Multijet Production in Charged Current Deep Inelastic Scattering with ZEUS at HERA

by

Homer Frederick Wolfe

A dissertation submitted in partial fulfillment of the

requirements for the degree of

Doctor of Philosophy

(Physics)

at the

University of Wisconsin – Madison

2008

Draft Version November 3, 2008

Multijet Production in Charged Current Deep Inelastic Scattering with ZEUS at HERA

Differential jet cross sections have been measured in charged current deep inelastic $e^{\pm}p$ scattering at high boson virtualities Q^2 with the ZEUS detector at HERA using an integrated luminosity of 0.36 fb^{-1}. Jets were identified using the k_T cluster algorithm in the longitudinally invariant inclusive mode. Polarized and unpolarized-corrected cross sections are presented for inclusive-jet production as functions of Q^2, Bjorken x and the jet transverse energy and pseudorapidity. The dijet invariant mass cross section is also presented. Observation of three-jet events in charged-current processes is reported for the first time. The predictions of leading-logarithm parton-shower Monte Carlo models and next-to-leading-order QCD calculations are compared to the measurements.

The design, operation, and commissioning of the HERA Collider and ZEUS Detector required the dedication of many individuals, without whom this research would not have been possible. The author would also like to personally thank Professor Claudia Glasman for providing her guidance, skill, effort and time to this work and the associated publication. Professor Juan Terrón also donated invaluable assistance with the theoretical calculations and numerous helpful suggestions during the course of this work. A special thanks is also given to the author's advisors: Professor Don Reeder, Dr. Alexander Savin, and Professor Wesley Smith, for providing expert advice and broad perspective to my education.

Contents

List of Tables

List of Figures

Chapter 1

Introduction

In this thesis, measurements of charged current jet production in polarized electron-proton scattering and comparisons to theoretical predictions are presented. The results presented are beneficial to the understanding of fundamental interactions and dynamics of the proton. The measurements presented were performed using the ZEUS detector at the HERA collider, which was part of the DESY accelerator complex in Hamburg, Germany. The predictions were derived from a theory called the Standard Model of Particle Physics (SM), which is briefly outlined in this chapter. The parts of the SM most relevant to this analysis and the methods used to compute the predictions are described in detail in chapter 2, and the experimental conditions are described in chapter 3. The methods used to process, simulate, and select data from the detector are described in chapters 4, 5 and 6, respectively. The techniques used to analyze the data are presented in chapter 7, and the subsequent results are presented in chapter 8. The importance of this work and potential extensions of this study are discussed in chapter 9.

1.1 Particles of The Standard Model

At present, the most complete and general description of the content and behavior of matter is the Standard Model. It is a highly successful theory, with a range of validity covering several orders of magnitude in energy, and predicted quantities which agree with observation to many significant figures. The SM describes the properties of matter as the dynamics and interactions of particles which are fundamental in the sense that they have no internal structure, and are indistinguishable among a given variety.

The particles of the SM can be organized into two major categories based on intrinsic angular momentum: particles which possess integral spin are referred to as *bosons*, while particles which possess half-integral spin are referred to as *fermions*. The elementary bosons of the SM mediate interactions of three kinds, and come in four types:

1. photons, γ, which mediate the electromagnetic interaction
2. gluons, g, which mediate the *strong* interaction
3. W & Z bosons, which mediate the *weak* interaction

Gravitational interactions are not described by the SM, but are widely accepted to be negligible in the conditions described in this work.

The fermions of the SM are classified into two groups: *quarks*, which possess the *color charge* of the strong interaction, and *leptons*, which do not. Protons, neutrons, and other *hadrons* are described in the standard model as composite objects, comprised of quarks and gluons. Quarks and gluons are referred to collectively as *partons* when

describing the content of hadrons. Quarks each possess spin $\pm 1/2$, a color of *red*, *green* or *blue*, and an electric charge of +2/3 or -1/3. Quarks with electric charge 2/3 and -1/3 are referred to as *up-type*, and *down-type*, respectively. Up-type quarks appear in three *flavors*: *up* (u), *charm* (c) and *top* (t), as do down-types: *down* (d), *strange* (s) and *bottom* (b).

Leptons possess spin $\pm 1/2$, no color charge, and electric charge of -1 or 0. Leptons with zero mass are referred to as *neutrinos*, and charged leptons include the electron (e^-), muon (μ), and the tau (τ). Neutrinos interact solely via the weak interaction, which associates one neutrino with each charged lepton. Neutrinos receive names from their weak interaction partners and are called the electron- (ν_e), muon- (ν_μ), and the tau neutrino (ν_τ). This pairing partitions the leptons into three *generations* of *doublets*, where two generations differs only by the mass of the particles of each type. The weak interaction likewise partitions quarks into three generations of doublets by associating pairs of up- and down-type quarks, specifically $u - d$, $s - c$ and $t - b$. The up type and down type quarks if each generation also differ only in their masses.

For each fermion, the SM additionally describes one antifermion. Fermions and their antipartners differ only by electromagnetic charge, with the charge of antipartners being equal but opposite. The possible color charges of anti-quarks are the anti-colors *antired*, *antigreen* or *antiblue*. The antiparticle of the electron is the *positron* (e^+), and is identical to the electron in every way except for having charge +1. All other antiparticles are usually referred to identically as their partners, but with a prefix of anti-, and are symbolically denoted with an overline. For example, the antiparticle of

the blue up is the anti-blue anti-up ($\overline{u}$).

The weak interaction additionally partitions fermions into two categories based on their *helicity*, which is the sign of the projection of a particles spin along its direction of motion. Particles with positive helicity are said to be *right-handed*, while particles with negative helicity are called *left-handed*. The a particle's transition under the weak interactions is indicated by the quantum number *weak isospin* (T_3). Left-handed charged leptons and left-handed up-type quarks have $T_3 = 1/2$, while left-handed neutrinos and left-handed down-type quarks have $T_3 = -1/2$. Right-handed fermions and left-handed antifermions have $T_3 = 0$. They form weak isospin singlet states, and do not participate in the weak interaction. *Weak hypercharge*, Y_W is a number determined for the EM charge and weak isospin of each particle by $Y_W = 2(Q - T_3)$, where Q is the EM charge. Table 1.1 summarizes the most important quantum numbers for the left-handed fermions. It is intersting to note that the electromagnetic, weak and strong couplings for left-handed anti-neutrinos are all zero. The do not participate in any SM interaction, but are included in the table for symmetry.

1.2 The Standard Model Lagrangian and its Symmetries

In the SM, the particles listed in section 1.1 are the quanta of *fields*, $\phi(x)$, which are functions that take complex vector values at each point in space-time. These functions are determined by the minimization of a scalar *action*, S. The action is the space-time integral over the *Lagrangian density*, $\mathcal{L}$, which is a functional of the fields and their *covariant derivatives* $D_\mu\phi$. This is written as

$$S = \int d^4x \mathcal{L}(\phi, D_\mu\phi). \tag{1.1}$$

	Generation	Name	Symbol	Electric Charge	Weak Isospin	Weak Hypercharge	Mass
Leptons	I	Electron	e^-	-1	-1/2	-1	511 keV
		Positron	e^+	+1	0	+2	
		Electron Neutrino	ν_e	0	+1/2	-1	< 2 eV
		Electron Antineutrino	$\overline{\nu_e}$	0	0	0	
	II	Muon	μ^-	-1	-1/2	-1	106 MeV
		Antimuon	μ^+	+1	0	+2	
		Muon Neutrino	ν_μ	0	+1/2	-1	< 2 eV
		Muon Antineutrino	$\overline{\nu_\mu}$	0	0	0	
	III	Tau	τ^-	-1	-1/2	-1	1.78 GeV
		Antitau	τ^+	+1	0	+2	
		Tau Neutrino	ν_τ	0	+1/2	-1	< 2 eV
		Tau Antineutrino	$\overline{\nu_\tau}$	0	0	0	
Quarks	I	Up Quark	u	+2/3	+1/2	+1/3	~ 3 MeV
		Up Antiquark	$\overline{u}$	-2/3	0	-4/3	
		Down Quark	d	-1/3	-1/2	+1/3	~ 6 MeV
		Down Antiquark	$\overline{d}$	+1/3	0	+2/3	
	II	Charm Quark	c	+2/3	+1/2	+1/3	~ 1.3 GeV
		Charm Antiquark	$\overline{c}$	-2/3	0	-4/3	
		Strange Quark	s	-1/3	-1/2	+1/3	~ 100 MeV
		Strange Antiquark	$\overline{s}$	+1/3	0	+2/3	
	III	Bottom Quark	b	-1/3	-1/2	+1/3	~ 4.2 GeV
		Bottom Antiquark	$\overline{b}$	+1/3	0	+2/3	
		Top Quark	t	+2/3	+1/2	+1/3	~ 171 GeV
		Top Antiquark	$\overline{t}$	-2/3	0	-4/3	

Table 1.1: Properties of Left-Handed Fermions.

The covariant derivatives take the form $D_\mu \equiv \partial_\mu - igA_\mu$, were g is the coupling strength of the interactions, and A_μ are *gauge potential fields*, analogous to the electromagnetic vector potential in classical electrodynamics.

The SM Lagrangian is a member of a class of Lagrangians which is invariant under local phase rotations, $\Lambda(x)$ of its fields $\phi \rightarrow e^{ig\Lambda}\phi$, and corresponding transformations of the gauge fields $A_\mu \rightarrow A_\mu - 1/g\partial_\mu\Lambda$. The value of $\Lambda(x)$ is defined independently at each point in space time, and takes matrix values with dimension appropriate to the interaction in question. Such transformations are called *gauge transformations*, Lagrangians that are invariant under these transformations are called *gauge invariant*, and theories with gauge invariant Lagrangians are called *gauge theories*. Gauge transformations form mathematical groups under composition, and provide the application of group theoretic technology to SM computations. The principle point of interest here is that because gauge transformations must be compatible with the potential fields, and the potential fields determine the interaction, the gauge symmetry group of the Lagrangian determines the interactions and *vice-versa*.

The symmetry group for electromagnetic interactions is $U(1)$, which can be represented as the multiplicative group of complex numbers of magnitude 1. The resultant field theory is referred to as Quantum Electrodynamics (QED). The symmetry group of the weak interaction is $SU(2)$, which can be represented as a two-dimensional matrix group generated by traceless Hermitian matrices, such as the three Pauli matrices. In the SM, the electromagnetic and weak interactions are unified at high energies to form the gauge group $U(1)_Y \times SU(2)_L$, where $Y = 2(Q + I_z)$ denotes *hypercharge*, and I_z denotes *isospin*. This gauge is referred to as the *electroweak gauge* and its four gen-

erators correspond to four independent gauge fields, which at low energies form fields for the neutral (γ, Z^0) and charged (W^+, W^-) electromagnetic and weak bosons.

The symmetry group for the strong interaction is $SU(3)$, which can be represented as the three dimensional matrix group generated by traceless Hermitian matrices, such as the eight Gell-Mann matrices. From eight generators arise eight independent gluon color fields. The resultant field theory is referred to as Quantum Chromodynamics (QCD). While the U(1) group is Abelian, the SU(2) and SU(3) groups are not. As a consequence, photons do not interact with other photons, allowing for the principle of superposition. Weak and strong fields, on the otherhand, are self-interacting, and their dynamics are non-linear.

1.3 Perturbative Field Theory and Renormalization

For a given observable quantity in the SM, it is often infeasible to perform an exact computation. Instead, series expansion is often performed which can be truncated to finite order. Often, this expansion parameter is the coupling strength of a process.

$$f(\alpha) = \sum_{n=0}^{\infty} f_n \alpha^n$$

In this case, each f_n can be represented as a Feynman diagram, where the order n corresponds to the number of interaction vertices in the diagram. If the coupling strength is less than 1, then the series has the potential to converge. *Leading-order* (LO) diagrams denote those terms if lowest order in n, while *next-to-leading-order* (NLO) denote the next highest, and so forth. Although any observable must have a finite amplitude, individual Feynman diagrams are often not finite. Truncated series

must then be treated with a process called renormalization in order to produce a finite prediction.

When comparing measurements with these renormalized predictions from truncated series, the measurements are reinterpreted not in terms of the parameters of the Lagrangian, called the *bare parameters*, but instead different parameters, called *renormalized parameters*. Renormalized parameters are dependent upon how the measurement is made, and this is parametrized in terms of a *renormalization scale* (μ_{R}).

The result is that the coupling strength of a renormalized theory is not a constant, but varies with scale $\alpha \rightarrow \alpha(\mu_{\mathrm{R}})$. This dependence is called *running* of the coupling, and agrees well with observed phenomena. The physical interpretation of μ_{R} is dependent on the particular process being studied, but can be thought of as the energy of the probe used, or the inverse distance that the probe can resolve or penetrate.

Perturbative QCD has been used in this thesis to produce theoretical predictions, as described in sections 2.3 to 2.10. Leading order calculations are also at the core of the event simulations which are described in chapter 5.

1.4 Confinement and Asymptotic Freedom in QCD

Figure 1.1 depicts the trend of running for the QED and QCD coupling constants, α_{EW} and α_{S}. Of greatest contrast between the two interactions is that α_{EW} asymptotically approaches a finite constant of approximately 1/137 for soft interactions, while the α_{S} increases, and diverges at a scale of λ_{QCD}. The value of λ_{QCD} depends on the renormalization procedure, but is usually on the order of 200 MeV. The increase of α_{S} at low scales is responsible for the feature of *confinement* which

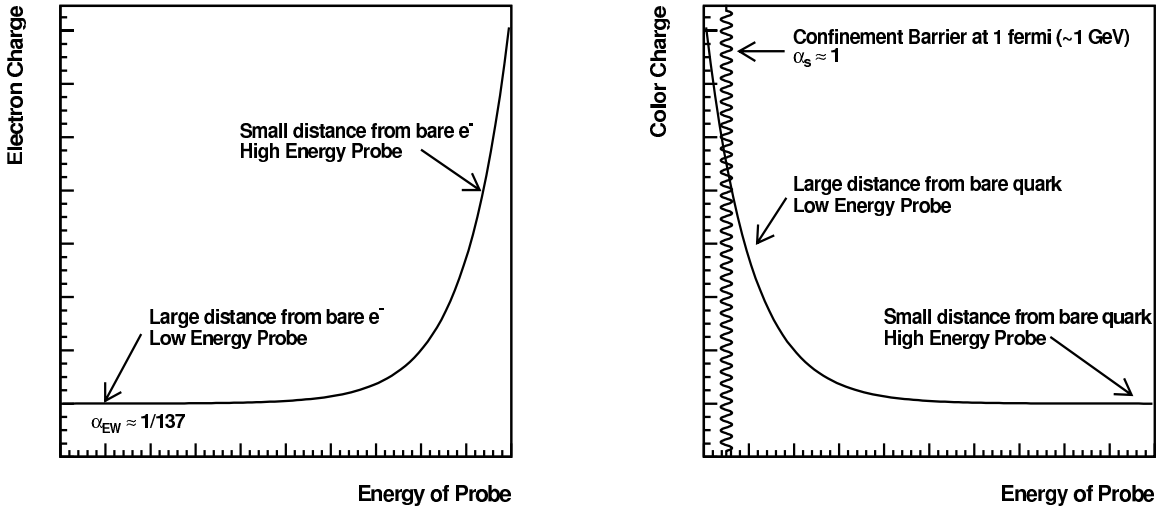

Figure 1.1: Behavior of the QED and QCD Couplings

describes why colored partons are not observed in nature, but instead are confined to color-singlet hadronic states. At large scales, $\alpha_{\rm S}$ asymptotically approaches zero. When a particle with energy much greater than 1 GeV is used to probe the proton, the value of $\alpha_{\rm S}$ diminishes such that the interactions between partons becomes negligible. The partons then appear to be non-interacting, which is called *asymptotic freedom*.

1.5 Parton Density Functions

At scales below about 1 GeV, the strength of the strong force is so great that partons are confined in hadrons. Perturbative calculations in the strong coupling, $\alpha_{\rm S}$, are no longer possible because it is on the order of unity or greater, and the series no is no longer assumed to be convergent. In order to describe the behavior of hadronic scattering within the SM, it is at present necessary to use phenomenological methods to describe their quark and gluon content. This is described in terms of probability distributions, called *Parton Density Functions* (PDFs). These functions

are experimentally determined, but are universally applicable. This universality means that the PDFs extracted at two experiments should be equivalent, and the PDFs determined at one experiment can be used to make other types of predictions at another. Given a hadron with momentum P and a probe with momentum transfer Q^2, the PDF $q(x, Q^2)$ expresses the probability of observing a parton of type q in a hadron which carries a momentum xP.

1.6 Deep Inelastic Scattering

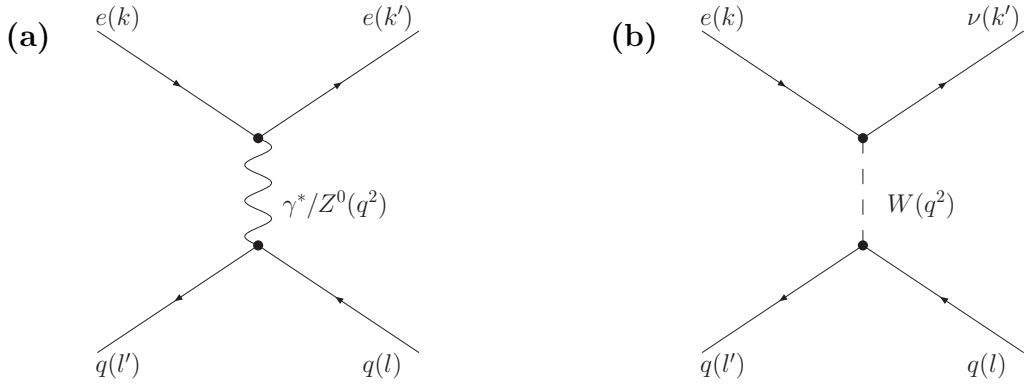

Figure 1.2: L.O. Feynman Diagrams for NC and CC DIS

Asymptotic freedom described in section 1.4 allows the scattering of point-like electrons on composite protons at high center-of-mass (CME) energies to be described in terms of the scattering of electrons off of independent quarks and gluons. This is accomplished by convolving predictions of parton-electron scattering in pQCD with the PDFs mentioned in section 1.5. At leading order in the the electroweak coupling, $\alpha_{\rm EW}$, and constant order in $\alpha_{\rm S}$, ep scattering proceeds via the quark parton model process, with Feynman diagrams shown in figure 1.2.

Figure 1.2(a) represents the Born-level exchange of virtual photons or Z^0 bosons

between electrons and quarks. When this is generalized to ep scattering at high energies, the process is referred to as Neutral Current (NC) Deep Inelastic Scattering (DIS). Here, the term deep refers to the resolving power of the probe, and inelastic refers to an increase in the Lorentz-invariant mass of the final state hadronic system. In NC DIS, the incoming electron is deflected, and appears in the final state. Figure 1.2(b) represents the Born-level exchange of charged W bosons between electrons and quarks. When this process is generalized to ep scattering, it is referred to as Charged Current (CC) DIS. In this process, the incoming electron does not appear in the final state, but is isospin rotated into a neutrino of the same generation. The initial-state up-type (down-type) quark likewise undergoes change of isospin, and is replaced in the final state by a down-type (up-type) quark of the same generation. The process is identical for e^-p and e^+p scattering, with the exception that the exchanged boson is either a W^- or W^+, in order to conserve electromagnetic charge at the upper EW vertex.

Other processes occur in ep scattering which were sources of background for this analysis. One of the largest was from Photoproduction (PHP), in which a photon with nearly zero invariant mass is exchanged between the e and p, which causes very little change in the electron's initial momentum. The soft photon can still interact inelastically with the proton, however. The ways that NC DIS and PHP can contaminate CC DIS samples and the means taken to remove these events are briefly discussed in section 1.9, and discussed in detail in chapter 6.

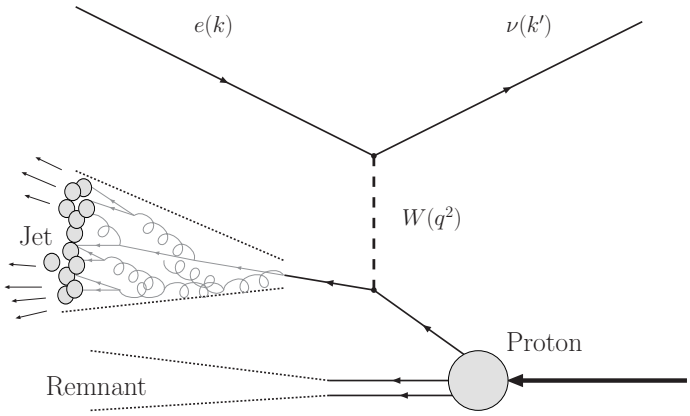

Figure 1.3: Schematic Diagram of Leading-order Jet Production in CC DIS.

1.7 Jet Production in DIS

Due to confinement, color non-singlet states such as the outgoing quark in Figures 1.2(a) and (b) are not observable quantities. Instead, partons dissociated from a hadron will undergo a process referred to as hadronization, in which observable color-singlet hadrons are produced. Because this process is soft, only small momentum transfers take place, and final-state momenta of the resultant hadrons will be approximately parallel, which is schematically represented in figure 1.3. This group of hadrons, referred to collectively as a *jet*, will closely resemble the kinematic properties of the initiating parton. This makes jets a powerful tool to study parton dynamics, and therefore a tool to understand the parton content of hadrons [1].

At higher order in α_s, the Feynman diagrams for eq scattering can have many partons in the final state. These partons will undergo hadronization separately, and will produce multiple separated jets in the final state. Events with at least one jet are referred to as *inclusive-jet production events*, while events with two, three or four are called *dijet*-, *trijet*-(3-jet) and *quadrajet*-(4-jet) events, respectively. Collectively,

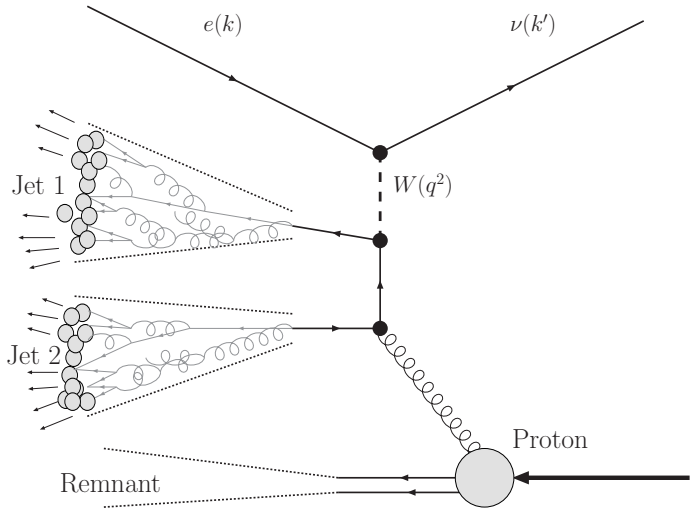

Figure 1.4: Schematic Diagram of Boson-Gluon Fusion CC DIS.

these are referred to as *multi-jet states*.

An example process which can produce dijets is represented schematically in figure 1.4, in which a gluon from the proton interacts with the W via a quark pair. This is referred to as *boson gluon fusion* (BGF). Measureables from this process are sensitive to the gluon content of the proton. Because the two jets are connected via a QCD vertex with the gluon, relationships between jets in the final state are an excellent means to test the predictions of QCD. Jet production is a non-perturbative process, and is phenomenologically modeled in two phases: QCD radiation and fragmentation. In the former, the initiating parton creates several new ones. In the latter, the partons produced in the radiative stage are combined into color less on-shell hadrons. Distributions of simulated jets can then be compared to distributions of reconstructed jets from a detector, as was performed in this thesis.

1.8 A Brief Overview Of The HERA Collider and The ZEUS Detector

The HERA collider was the world's first and only $e^{\pm}p$ collider, and produced $e^{-}p$ and $e^{+}p$ collisions during separate periods from 1992 to 2007. Previous ep experiments collided electrons with fixed targets like helium, but These experiments could only explore center of mass energies up to a few GeV [2]. The HERA collider consisted of two nearly-evacuated, nearly-circular storage rings with counter-cycling beams. HERA provided electron or positron beams with an energy of 27.5 GeV, and collided these with proton beams of 920 GeV to produce events with CMEs of approximately 300 GeV.

As HERA produced ep collisions, resultant particles were recorded in the ZEUS detector. The ZEUS detector was constructed around one of HERA's interaction points, and was roughly cylindrical in shape. Because interactions at HERA did not occur in the ep center-of-mass system, the ZEUS detector was built with more material in the direction the protons were traveling towards. Figure 1.5 shows a cutaway diagram of the ZEUS detector, so that the HERA beampipe is visible, and the viewer is facing the direction of lepton entry into the interaction. The standard ZEUS polar coordinate system places the nominal interaction point at the origin and the proton direction as the $\theta = 0$ line. ZEUS was composed of several independent detectors, each of which performed slightly different forms of measurement. Of central importance to this thesis is the Central Tracking Detector (CTD), and Calorimeter (CAL). The CTD covered a polar region of 30° to 150°, and recorded the path of charged particles in a magnetic field, to infer their masses, momenta and charges.

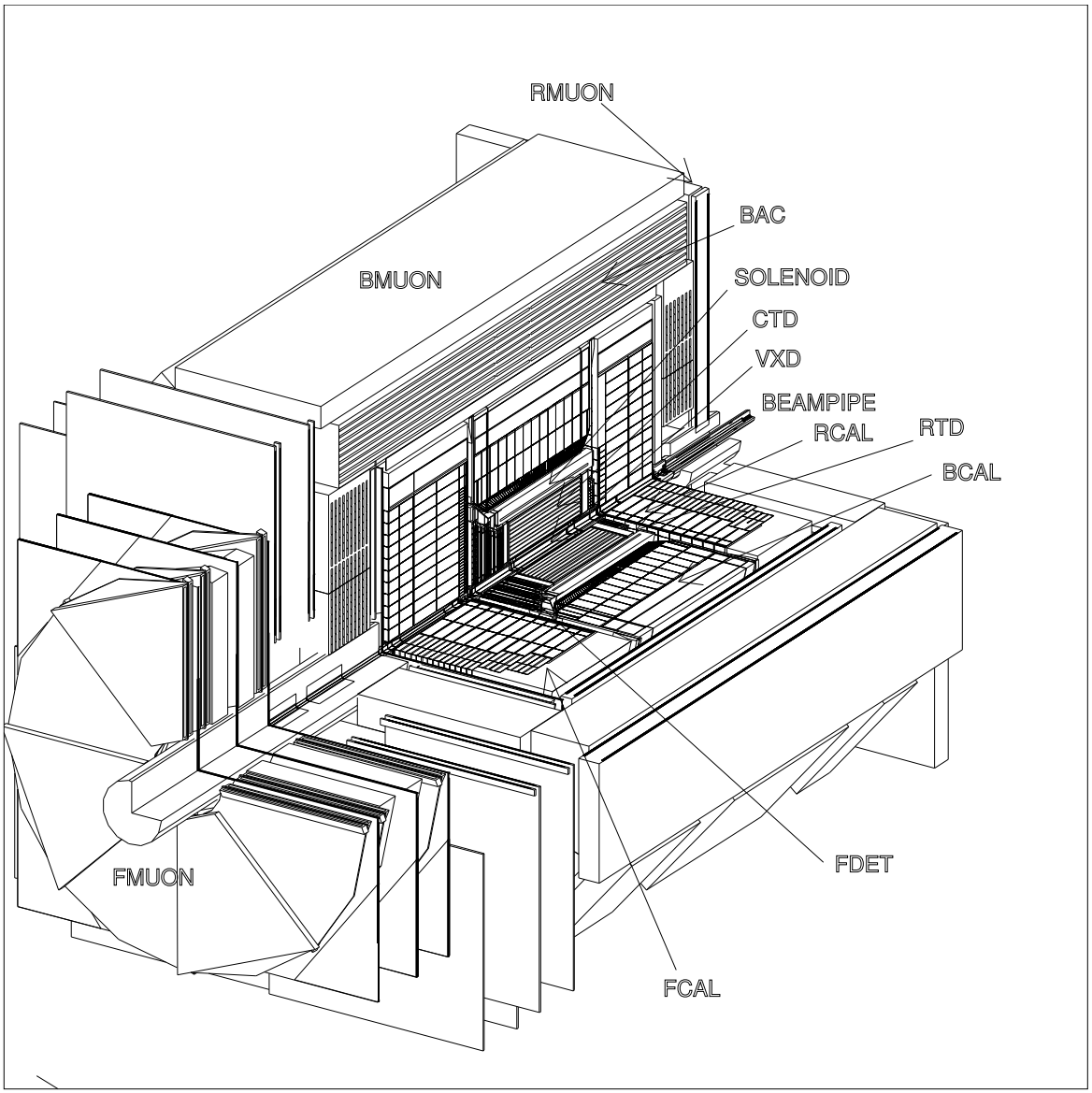

Figure 1.5: A Diagram of The ZEUS Detector

The CAL covered a polar angle range of 2.2° to 176.5°, and recorded the energy and position of electromagnetic- and strongly-interacting particles as they were absorbed by very dense metal. The absorber material was was arranged in units called *cells*, with a much coarser granularity than the CTD. When signals were recorded in the detector, a trigger system was used to select which events would be readout, and events were reconstructed and stored for analysis.

In figures 1.6 and 1.7, CC DIS candidate events are shown in the ZEUS CAL, CTD, and Forward Tracking Detectors. In figure 1.6, a single cluster of transverse energy is registered in the CAL, and tracks in the CTD lead from near the nominal vertex towards it. We identify this deposit with a jet. From the $x - y$ view, it can be seen that the energy deposits and tracks were not balanced in the direction transverse to the beamline, implying that something escaped detection in the direction opposite the jet. Because neutrinos only interact weakly, they are not expected to interact with the ZEUS detector and are therefore the most likely candidate for this type of signature.

In figure 1.7, we see two isolated deposits in the CAL, and two groups of particle tracks in the CTD. We label this event a dijet, which could have originated in a manner similar to figure 1.4. The plot of transverse energy in the ZEUS CAL at the bottom of figure 1.7 shows the separation of the two jets the CAL. These two candidate events can be compared with the ND DIS Dijet candidate event displayed in figure 1.8. Here, two broad, isolated hadronic deposits can be seen, and are counterbalanced in ϕ with the presence of a high-E_T REMC deposit, which is comprised from nearly one REMC cell. There is one isolated CTD track leading to this deposit, which strengthens its

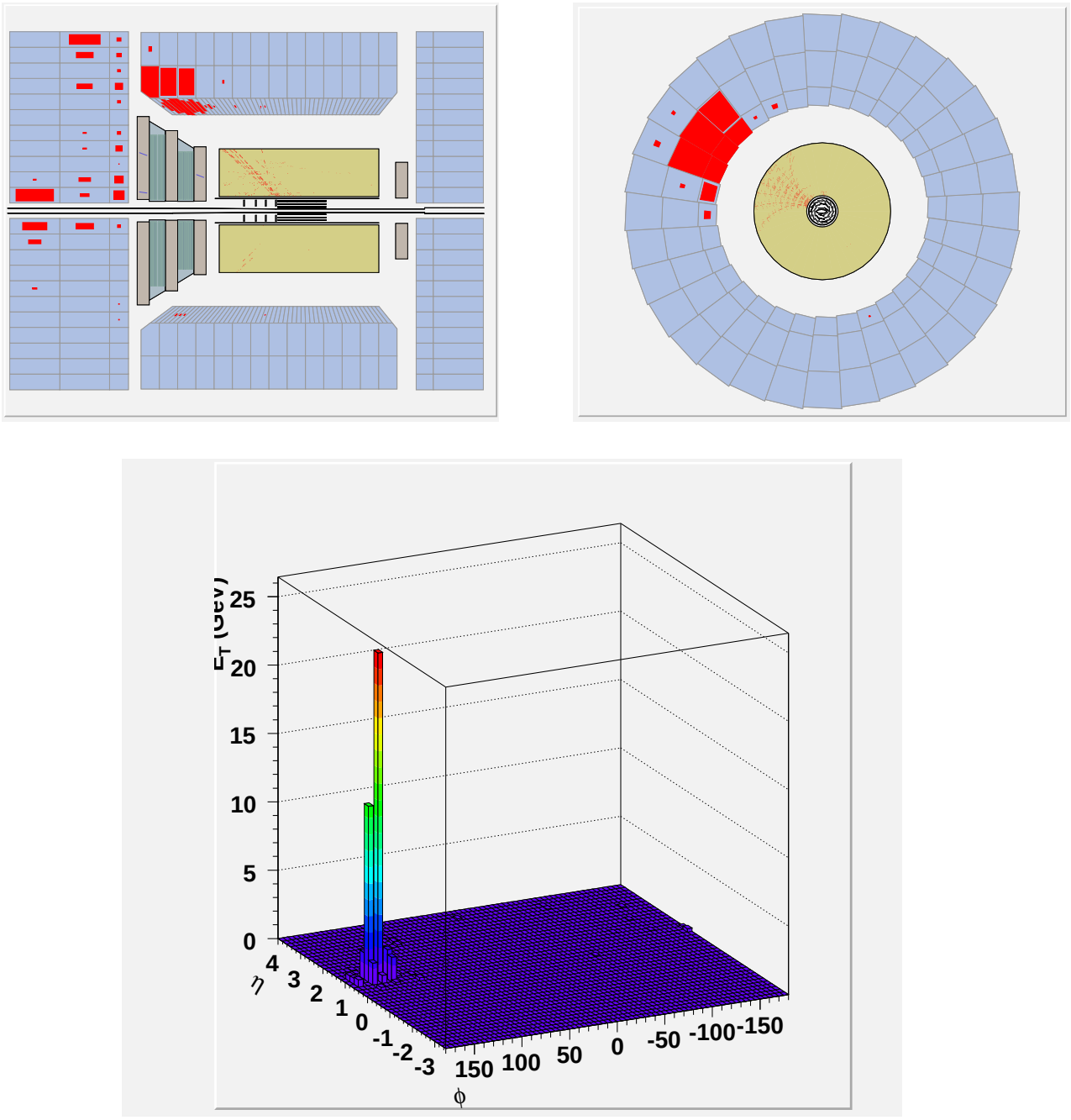

Figure 1.6: *Event Display Single Jet CC DIS*

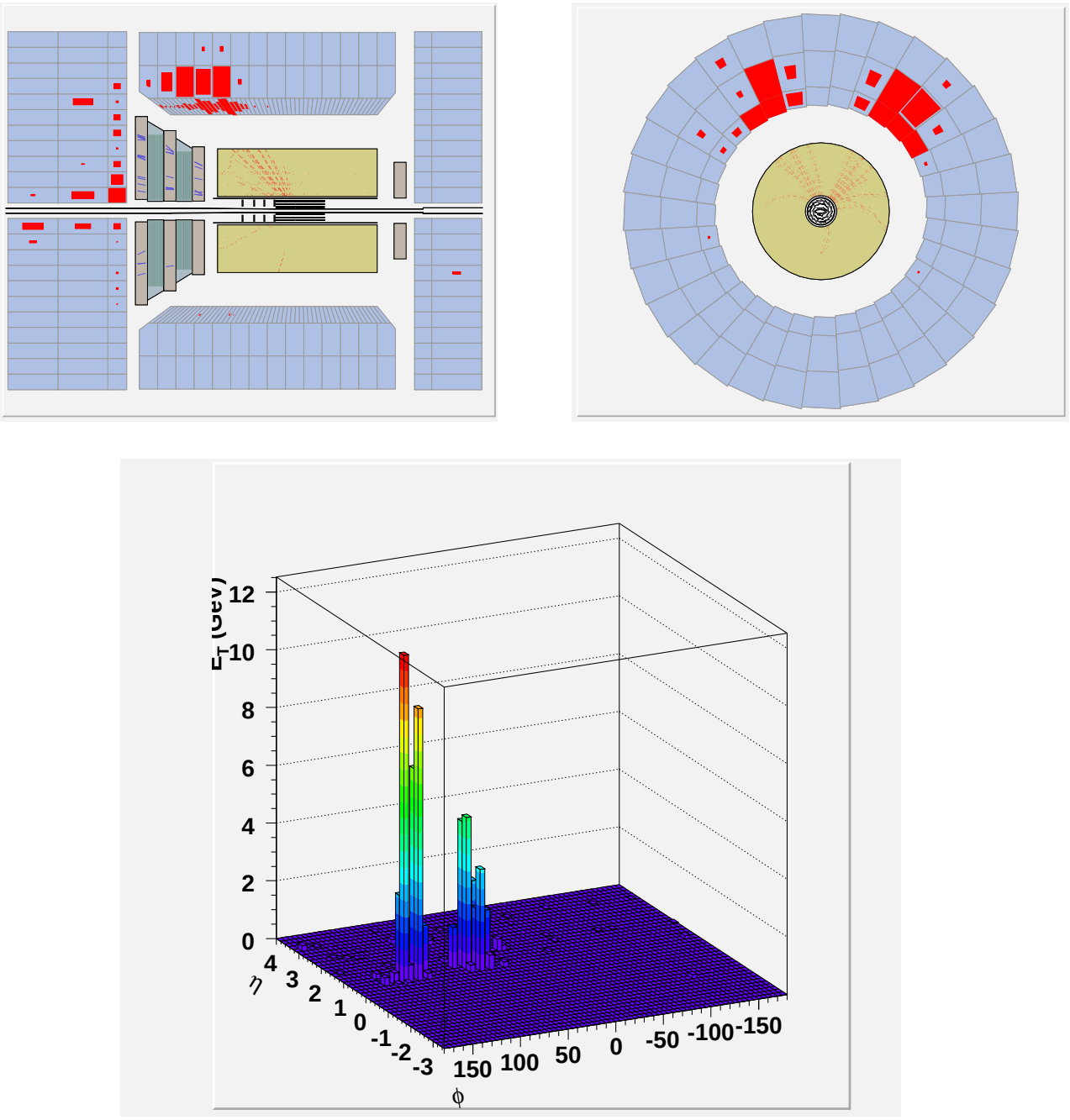

Figure 1.7: *Event Display of Dijet CC DIS*

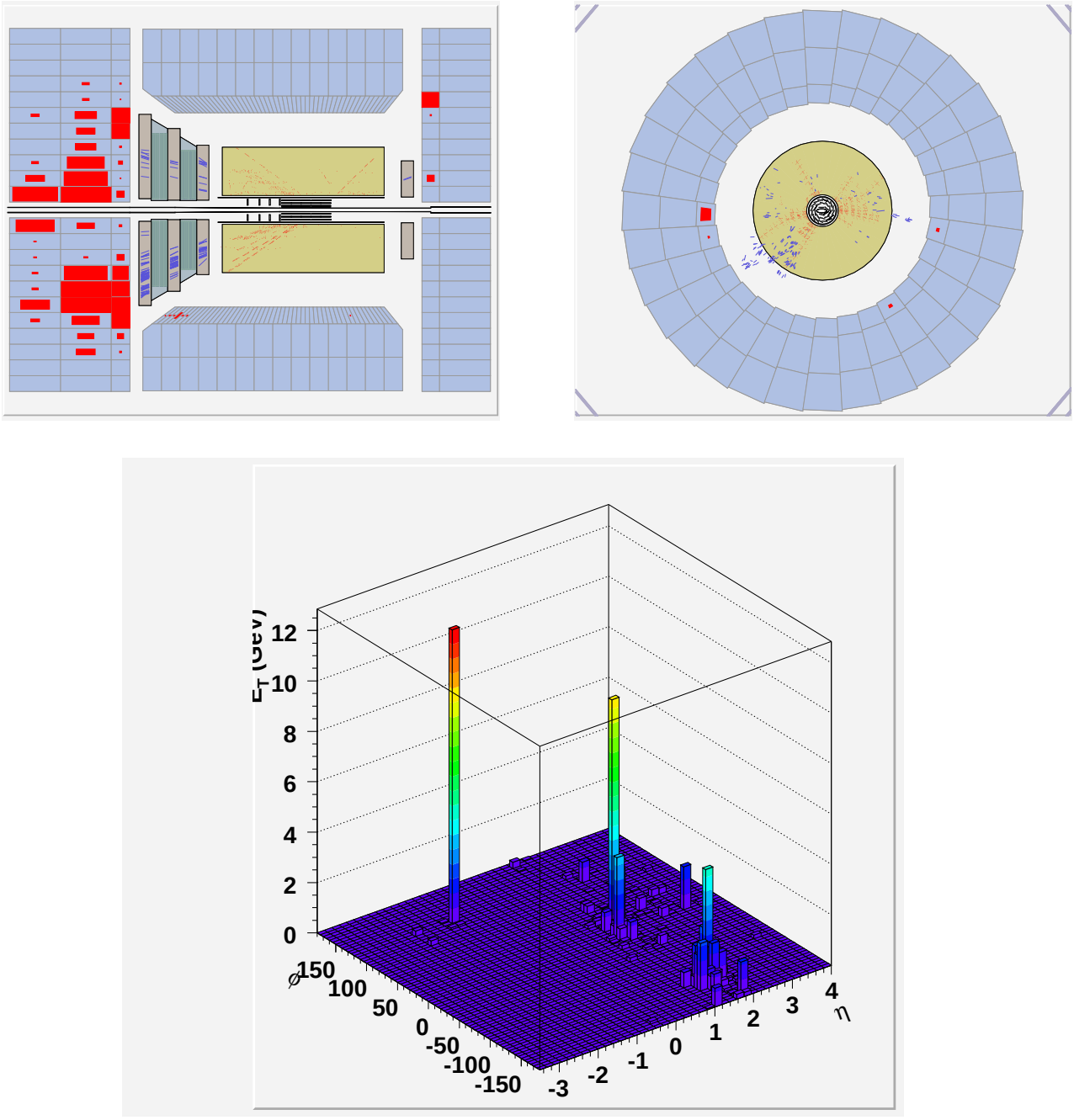

Figure 1.8: *Event Display of Dijet NC DIS*

candidacy as a scattered electron.

1.9 Methods Used In This Analysis

Once the data had been readout and stored from the ZEUS detector, software further reconstructed information about the interaction and CC DIS events were selected over background. Jets were reconstructed from clusters of CAL cells, and information from the CTD was used to determine the location of the primary interaction. Non ep background, such as cosmic rays and interactions between protons and residual gas in the beampipe were removed by comparing information of the CAL and CTD.

Because neutrinos interact only via the weak force, they were neither recorded by the CTD or CAL. Thus, a principle method of rejecting NC DIS is to reject events when an isolated electron was observed in the final state. In CC DIS neutrinos carry momentum from the event without detection, events therefore appear to have a nonzero net momentum transverse to the beampipe, P_T^{miss}. In PHP events the initial state electron is only slightly deflected in the interaction. The electron may escape detection down the beampipe, and with it carry transverse momentum. Some PHP events therefore have no recorded electron in the final state, and may have a non-zero net P_T^{miss}. The recorded P_T^{miss} from PHP may be larger than NC DIS, but is relatively small to the E_T produced in the inelastic γp interaction. In CC DIS, many events have $P_T^{\text{miss}} \approx E_T$, which makes P_T^{miss}/E_T is a powerful quantity to differentiate the two. Many other selection cuts are used to remove these events, as discussed later in chapter 6.

Once events were reconstructed and selected, a simulation of ep interactions and the ZEUS detector was used to correct the values obtained to remove the effects of the

detector itself. Rather than describing jets of calorimeter cells after particles passed through the detector, the corrected events described jets of hadrons. NLO calculations convolved with PDF functions were also corrected from describing jets of partons to describing jets of hadrons. The resulting distributions could then be compared to understand the strengths and weaknesses of the NLO calculations, and the PDF sets that were used.

Several variations were also performed on the analysis procedure, so that the uncertainties due to the reconstruction, simulations, and methods could be understood. Different PDF sets were also used, and their results were compared to understand the uncertainty on the measurements from the choice of PDFs used.

1.10 Overview Of Results And Implications Of This Analysis

CC DIS at high Q^2 has been measured previously by ZEUS and H1 under a variety of conditions. Inclusive CC DIS has been measured with and without longitudinally-polarized lepton beams [3, 4]. Scattering structure functions for the proton, which are directly related to PDFs were measured. Using polarized lepton beams, a search for the presence of right-handed weak interactions was performed, and no evidence for these effects was found. The ZEUS collaboration has also performed studies of jet production in e^+p CC DIS [5], in which the substructure of jets was studied and used to extract $\alpha_{\rm S}$. The H1 collaboration has published a study of Dijet production in e^+p CC DIS [6], in which CC Dijet cross sections were compared to NC Dijet distributions in the same phase space. The QCD characteristics of the jets were shown to be independent of the EW scattering process.

The analysis discussed in this thesis improves on previous studies in several

ways. The data sample utilized is larger by a factor of four than that used in [6], and approximately twice that used in [5]. The previous studies also did not incluse $e^- p$ data. The phase space explored in this work is wider in Q^2 than [6], and the angular range of jets explored herein is wider than in [5]. This also represents the first measurement of Jet production in CC DIS with longitudinally polarized leptons, The first measurement of differential cross sections of 3-jet final states in CC DIS,.and the first observation of 4-jet final states in CC DIS.

All of the PDFs for the proton are nonzero, but two of the largest functions are the u, and d, which respectively comprise approximately 2/3 and 1/3 of the proton at low energies. In $e^+ p$ CC DIS, a W^+ boson is exchanged, which, only interacts with d, $\bar{u}$, s and $\bar{c}$ quarks in the proton at lowest order in α_{S}[1]. In $e^- p$ CC DIS, a W^- boson is exchanged, which only interacts with $\bar{d}$, u, $\bar{s}$ and c quarks at lowerst order in α_{S}. This means that the $e^- p$ and $e^+ p$ offer very different information about the flavor content of the proton. The measurements presented in chapter 8 show a strong dependence on the PDF set used, most specifically a strong dependence on the d PDF. At present the d PDF has much larger experimental uncertainties than the u, so it is believed that this data can be used in conjunction with other measurements to improve the uncertainty of the d PDF. This knowledge is critical to extracting meaningful results at any hadron collider, because the uncertainties due to PDFs are often relatively large. Because the Large Hadron Collider will begin producing collisions in the near future, it is hoped that these results will be used by PDF extraction groups in future fits.

[1]The far heavier b quark has a neglectable contribution to this sample by comparison, and the interactions presented here do not contain sufficient energy to probe the t content of the proton.

Chapter 2

Theoretical Predictions

2.1 Kinematics of ep Scattering

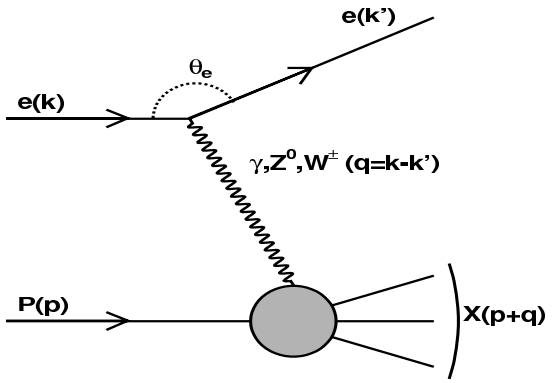

Figure 2.1: General Schematic of ep Scattering. The electron and proton interact via the spacelike exchange of a γ, W or Z with virtuality Q^2. The outgoing hadronic system is labeled X.

Figure 2.1 shows a very general ep interaction, for the purposes of defining kinematic variables. To simplify discussion, the initial state electron or positron will simply be referred to as the incoming lepton, and the final state electron, positron or neutrino will simply be referred to as the outgoing lepton. We label the 4-vectors of the incoming lepton, outgoing lepton, incoming proton and outgoing hadronic system as

k, k', p, and p_X, respectively. Electrons will be considered massless thoughout this work, and the mass of the proton is labled M_p. The following are Lorentz invariant quantities:

$$q^2 = (k - k')^2 = -Q^2, Q^2 > 0 \tag{2.1}$$

$$s = (p + k)^2 \tag{2.2}$$

$$W^2 = p_X^2 \tag{2.3}$$

$$\nu = \frac{p \cdot q}{M_p} = \frac{1}{2M_p}\left(W^2 + Q^2 - M_p^2\right) \tag{2.4}$$

Q, s, and W are identified as the transfer momentum, center of mass energy (CME) of the ep system, and invariant mass of the outgoing hadronic system. In the rest frame of the proton, ν is the energy difference of the incoming and outgoing lepton. The following variables will be used extensively:

$$x = \frac{Q^2}{2p \cdot q} = \frac{Q^2}{2M_p\nu} = \frac{Q^2}{W^2 + Q^2 - M_p^2} \tag{2.5}$$

$$y = \frac{p \cdot q}{p \cdot k} \tag{2.6}$$

The Bjorken scaling variable x is identified at the born level with the fraction of the momentum of the quark which participates in the hard scattering with that of the initial state proton. The variable y is referred to as the inelasticity of the interaction. Neglecting the masses of the incoming particles they are related by $Q^2 = sxy$.

2.2 Cross Sections

The results of this thesis are differential cross sections, $\frac{d\sigma}{d\Omega}$ which are defined as the rate or number of outgoing particles in a given state divided by the number of incoming particles. Summing over all possible outgoing states results in the *total-* or *integrated cross section*:

$$\sigma = \int_{\Omega} \frac{d\sigma}{d\Omega} = \frac{N}{L} \tag{2.7}$$

Where N is the number of outgoing states and L is the *integrated luminosity*, a measure of the total incoming flux.

The differential cross section for CC DIS versus x and Q^2 can be written as [7],

$$\frac{d^2\sigma(e^{\pm}p \to \nu X)}{dxdQ^2} = \frac{G_F^2}{4\pi x}\left(\frac{M_W^2}{M_W^2+Q^2}\right)\left[Y_+ F_2^{CC} - y^2 F_L^{CC} \mp Y_- x F_3^{CC}\right], \tag{2.8}$$

where G_F is the Fermi coupling constant, M_W is the mass of the W boson, and $Y_\pm = 1 \pm (1-y)^2$. The scalar functions $F_n^{CC}(x, Q^2)$ are called *structure functions*, and parametrize the flavor content of the proton and soft QCD interactions involved in ep scattering. These are not computable in pQCD, and must be experimentally determined. F_L^{CC} is very small relative to the other two structure functions. These are related to the PDFs by

$$F_2(e^- p \to \nu X)) = x\left(u + \bar{d} + c + \bar{s}\right) \approx xu \tag{2.9}$$

$$xF_3(e^- p \to \nu X)) = x\left(u - \bar{d} + c - \bar{s}\right) \approx xu \tag{2.10}$$

$$F_2(e^+ p \to \bar{\nu} X)) = x\left(\bar{u} + d + \bar{c} + s\right) \approx xd \tag{2.11}$$

$$xF_3(e^+ p \to \bar{\nu} X)) = x\left(-\bar{u} + d - \bar{c} + s\right) \approx xd, \tag{2.12}$$

where we have neglected b and t PDFs, because we assume them to be statistically

negligible at the scales probed here. Gluons have likewise been neglected in the above, which is only correct to lowest order in α_{S}.

The differential cross section in terms of x and y can be derived by [8]

$$\frac{d^2\sigma}{dxdy} = x\left(s - M_P^2\right)\frac{d^2\sigma}{dxdQ^2}. \tag{2.13}$$

2.3 The MEPJET Program

The pQCD calculations in this thesis were produced with the MEPJET 2.1 [9, 10] program, which was written for DIS by E. Mirkes. D. Zeppenfeld and S. Willfahrt. It is capable of computing partonic cross sections in DIS via exchange of photons, Z, and W bosons at $\mathcal{O}(\alpha_{\mathrm{S}})$ or $\mathcal{O}({\alpha_{\mathrm{S}}}^2)$. For this analysis, only W exchange was calculated, with the mass of the W boson set to 80.40 GeV. The number of active quark flavors was set to 5, and $\Lambda^{(5)}_{\overline{\mathrm{MS}}}$ was set to 226 MeV, which corresponded to a strong coupling constant $\alpha_{\mathrm{S}}(M_Z) = 0.118$. α_{EW}, G_F, and M_Z were set to the same values as chosen for the MC described in section

$$\begin{aligned} \alpha_{\mathrm{EW}} &: 1/137.035999 \\ G_{\mathrm{F}} &: 1.664 \times 10^{-5}\ \mathrm{GeV}^{-2} \\ M_Z &: 91.1876\ \mathrm{GeV} \end{aligned} \tag{2.14}$$

. For the inclusive-jet calculations, $\mathcal{O}(\alpha_{\mathrm{S}})$ predictions were produced, which are NLO. For dijet (three-jet) cross sections, $\mathcal{O}({\alpha_{\mathrm{S}}}^2)$ predictions were produced, which were NLO (LO).

2.4 Phase Space Slicing Method

The MEPJET program uses the phase space slicing method [11] to cancel infrared and collinear divergences. A parameter $s_{\min}$ was introduced, which acts as a minimum resolving power to separate partons, and effectively separates finite and infinite portions of the phase space. Integrals in regions where particles i and j satisfied $s_{ij} \cong 2p_i \cdot p_j < s_{min}$ were calculated analytically. Some divergences were matched and exactly cancelled with virtual contribution divergences, and others were subtracted as described in section 2.5. It has been shown that the final results are independent of the unphysical parameter $s_{\min}$ when $s_{\min}$ is less than or on the order of 0.1 GeV [10]. The remaining phase space, where the integrals were free of these divergences, were left to be calculated numerically by MC integration techniques. Leaving the finite portion of the phase space integral for the user provides a flexible system for custom modification of phase space cuts.

2.5 $\overline{\text{MS}}$ Renormalization Scheme

In MEPJET, the one-loop divergences in the diagrams are handled in the $\overline{\text{MS}}$ renormalization scheme. The scheme begins by introducing a dimensional regulator for loop momentum, by transforming the 4-dimensional integral over virtual particle momenta into $4-2\epsilon$ dimensions. This parametrizes the divergences in ϵ, but artificially introduces additional constant terms. The name stands for modified minimal subtraction, because the earlier method of subtracting only divergent parts [12] was later modified by additionally subtracting the constant terms that were introduced [13].

2.6 Factorization Scale and Evolution of Parton Density Functions

In addition to the choice of the renormalization scale at which the matrix elements are evaluated, an additional scale choice is made called the *factorization scale*. This scale is the delineation between the hard scattering computed in pQCD, and the soft QCD processes in the proton. Just as observable quantities should not depend on μ_{R}, they should not depend on μ_{F}, either. The Dokschitzer-Gribov-Lipatov-Altarelli-Parisi (DGLAP) [14, 15, 16, 17] equations are a set of $2(n_f + 1)$ coupled integro-differential equations which require that each structure function be independent of μ_{F}. In doing so, the DGLAP equations describe how the PDFs change with Q^2 and μ_{F}, allowing PDFs measured in one process to be used in predictions for another. The PDFs in this analysis come from the Coordinated Theoretical-Experimental Project on QCD (CTEQ5D, CTEQ6D) [18, 19, 20], Martin Roberts Stirling Thorne (MRST2001) [21], and The ZEUS Collaboration [22].

2.7 Scale Dependence and Uncertainty

In MEPJET, ultraviolet divergences were renormalized and absorbed into the bare coupling constant, introducing a dependence of the renormalized coupling $\alpha_{\mathrm{S}}(\mu_{\mathrm{R}})$. For this analysis, μ_{R} was set to Q for the central values extracted from the calculations. The dependence on μ_{R} would cancel for calculations performed at all orders in α_{S}, but for our fixed order calculations, some residual scale dependence persists. To quantify the uncertainty introduced by our choice, the calculations were also performed using the canonical adjustments $\mu_{\mathrm{R}} \equiv Q/2$ and $\mu_{\mathrm{R}} \equiv 2Q$. The optimal amount of adjustment

used in this technique is not universally agreed upon, but is common practice for High Energy Experimental Physics [23].

In MEPJET, initial state collinear divergences were factorized into the bare parton densities, introducing a dependence of the final cross sections on the factorization scale μ_F [10]. This scale was also set to Q, and modified by a factor of 2 up and down to quantify uncertainty based on this choice.

2.8 PDFs and PDF Uncertainty

To produce ep scattering predictions, eq and eg hard scattering functions must be convolved with PDFs. Calculations in this thesis were performed using the ZEUS-S [24] parametrization of the proton PDFs. PDFs must be experimentally determined, and contain both theoretical and experimental uncertainties. To understand the experimental uncertainty of the PDFs effect on results, calculations were performed using the 22 alternative PDFs from the ZEUS-S set, each of which contains different experimental input. This method takes into account the statistical and correlated systematic experimental uncertainties of each data set used in the determination. To understand the theoretical uncertainty involved in the choice of parametrization, alternative calculations were performed using the CTEQ6 and MRST sets.

2.9 Systematic Uncertainty Estimate for the Calculations

No alternative $\mathcal{O}(\alpha_S{}^2)$ calculations exists for CC DIS processes at this time. It is therefore not possible to produce a direct estimate of the uncertainty introduced by our choice of MEPJET. However, because MEPJET also produces NC DIS calculations, and because alternative NLO programs for these processes do exist, we can compare

NC DIS predictions, and consider the difference an estimate of the uncertainty introduced from the use of MEPJET. It was observed in [25] that while MEPJET and the alternative program DISENT [26] agree for inclusive NC DIS jet cross sections on the order of 1%, the relative disagreement for NC DIS dijet cross sections is on the order of $5 - 8\%$.

2.10 Correction of the Calculations to the Hadron Level

The calculations described above produce cross sections of jets of partons. These cross sections are referred to as *parton level* cross sections. In order to compare these predictions from cross sections which were measured, these cross sections were corrected to describe jets of hadrons. The resultant cross sections are referred to as *hadron level* cross sections. This was performed using the event simulations described in chapter 5, and the techniques used to accomplish this are describedin section 7.3 in detail.

Chapter 3

Experimental Setup

3.1 The DESY Laboratory

The analysis presented in this thesis was performed with data from the ZEUS detector, which was situated on the Hadron-Elektron Ring Anlage (HERA), at The Deutsches Elekronen-Synchrotron (DESY) Laboratory in Hamburg Germany. DESY is part of the Helmholtz Association, and has two locations in Germany: one in Hamburg, and one in Zeuthen. DESY's facilities are used primarily for the study of natural sciences, specifically pertaining to the use of particle accelerators of varying size to probe the structure of matter. DESY hosted on average approximately 3000 scientists from 33 different countries for research related to HERA and HASYLAB, the associated synchrotron complex.

3.2 The HERA Accelerator

HERA was the world's first and only lepton-nucleon beam collider, and was the largest accelerator at the DESY complex. A nearly circular construction with a circumference of 6.3km, HERA was approved for construction in 1984, and built between

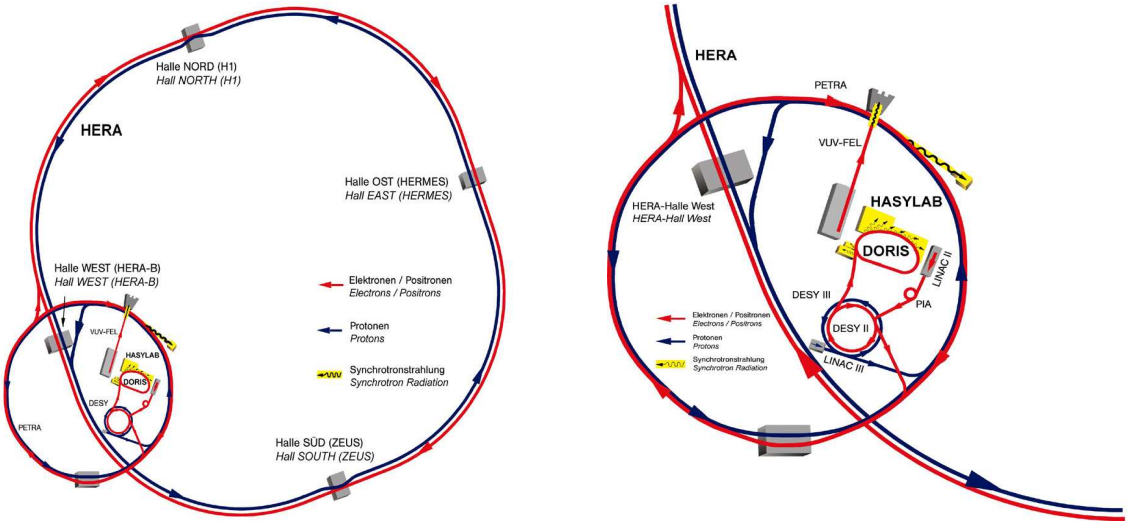

Figure 3.1: Schematic of the DESY Accelerator Complex

1984 and 1991. The commissioning of the electron ring and proton ring occurred in 1989 an 1991, respectively. HERA provided luminosity to its experiments from mid 1992 until 2 July, 2007, when it was decommissioned. Figure 3.1 is a schematic representation of HERA and the pre-accelerator elements. Particles were produced at low energies, and sequentially passed between different pre-accelerators before reaching HERA, as described below.

3.2.1 Proton Injection and Acceleration

To produce protons for collisions, hydrogen gas was ionized and accelerated in the LINAC III linear accelerator to 50 MeV. The ions were passed through a thin metal

foil to strip the remaining electron, and passed to the DESY III synchrotron for further acceleration to 7.5 GeV. DESY III is a 317 m circumference storage ring which could hold up to 11 proton bunches with approximately 10^{11} protons per bunch. From DESY III, protons were injected into PETRA II, which accelerated bunches up to 40 GeV. Protons were then injected into HERA for acceleration up to and maintained at their final energy. HERA operated at several different proton energies during its lifetime, but all data presented in this thesis arise from collisions with 920 GeV protons.

3.2.2 Lepton Injection and Acceleration

During periods of electron-proton collisions, electrons were produced by a hot metal filament. During periods of positron-proton collisions, positrons were produced by scattering electrons on tungsten sheets, resulting in the production of e^+e^- pairs by Bremsstrahlung. HERA provided both electron-proton and positron-proton collisions during separate periods. Throughout the rest of this chapter, the term *electron* will denote separately to either electrons or positrons, unless otherwise stated. After production, electrons were accelerated up to an energy of 450 MeV in the LINAC II accelerator, which is a 70 m linear accelerator. They were then gathered in PIA, a 29 m accumulator. Bunches of approximately 3.5×10^{10} electrons were then injected into DESY II, a 293 m circumference synchrotron, which accelerated them to an energy of 8 GeV. From DESY II, electrons were injected into PETRA II, a 2.3 km circumference synchrotron, which accelerated bunches to 12 GeV. Electrons were then injected into HERA, and were accelerated to and maintained at an energy of 27.5 GeV.

3.2.3 Beam Circulation and Collisions

Within HERA, electron and proton beams were stored in separate beam pipes, each with a vacuum pressure of approximately 3×10^{-11} Torr. The bunches circulated in opposite directions, with a separation of approximately 28.8 m, which in time is 96 ns, and a frequency of 10.4 MHz. HERA could theoretically have held 210 electron and 210 proton bunches, but in practice about 10 bunches of each type were left unfilled to so that a filled bunch of the opposing type could circulate without collisions. This allowed the HERA Machine group to study beam dynamics separately from interactions. Additionally, approximately 15 successive bunches of each type were left unfilled to allow time for deflection magnets to energize for beam dumps.

At two places on the ring, labled north and south halls in Figure 3.1, the two beam pipes merged into one and the beams were brought together with nearly zero crossing angle. Two experiment halls were located at the intersection points, providing space for the general purpose detectors H1 and ZEUS. Two other experiments, HERMES and HERA-B detectors were located at experiment halls labeled east and west, respectively. HERA-B studied collisions between the proton beam and wire targets to study B hadron production, while HERMES studied collisions between the electron beam and a proton gas jet to study the spin structure of the proton.

Between 1992 and 1997, HERA collided 27.52 GeV leptons with 820 GeV protons, providing ep collisions with a CME of $s \approx \sqrt{4E_pE_e} \approx 300$ GeV. The energy of the protons from 1997 to 2007 920 GeV, ep collisions with a CME of approximately 320 GeV. During the last periods of operation in 2007, The proton energy was lowered to 450 and 575 GeV, in order to investigate a previously unexplored region of phase

space.

3.2.4 HERA Luminosity

HERA began operation providing electron-proton collisions, and has alternately provided positron-proton collisions. The *Instantaneous luminosity*, L can be described as the incoming flux of particles participating in a reaction. At a two-particle intersecting storage ring collider like HERA, this can be estimated as $L = f\,(N_1 N_2/A)$, where f is the frequency of bunch crossings, N_i is the number of particles in each bunch in beam i, and A is the area of overlap of the two beams. Thus, the instantaneous luminosity of HERA based on its design characteristics would be

$$L_{HERA} = f\frac{N_1 N_2}{A} \approx 10.4 \times 10^6 \frac{10^{20}}{3.36 \times 10^{-5} cm^2} = 3.1 \times 10^{31} cm^{-2} s^{-1} \qquad (3.1)$$

The average specific luminosity during the period 1992 to 2000 was approximately 2×10^{31} cm^{-2} s^{-1}. Between 2000 and 2002, HERA underwent a luminosity upgrade, which was primarily achieved by installing improved focusing magnets which diminished the interaction area of the two beams. The periods before and after the upgrades are referred to as *HERA I* and *HERA II*, respectively. The resulting specific luminosity for HERA II was approximately 3.8×10^{31} cm^{-2} s^{-1}. Direct detection of the instantaneous luminosity during HERA operation is described in section 3.3.3.

3.2.5 Polarized Collisions

The electron beam at HERA became naturally polarized transversely polarized due to the Sokolov-Ternov effect[27]. The characteristic build-up time expected for the HERA accelerator was approximately 40 minutes. During the 200-2002 luminosity upgrade, spin rotators on either side of the H1 and ZEUS detectors were installed

to change the electron polarization from transverse to longitudinal and back, providing collisions with longitudinally polarized electrons. Measurement of the electron polarization is described in section 3.3.3.

3.3 The ZEUS Detector

The ZEUS detector was a general purpose detector designed for studying various aspects of electron-proton scattering, and was located at the HERA south experiment hall. It was constructed from several independent subdetectors, which were built by universities from more than 11 countries.

The ZEUS collaboration used a right-handed Cartesian coordinate system to describe the design and operation of the ZEUS detector. The origin is located at the nominal interaction point, the positive z-axis pointed in the direction of the proton beam, the positive y-axis pointed upwards, and the x-axis pointed toward the center of HERA. The polar angle, θ, is defined by 0° in the direction of the proton beam, and 90° in the direction of the positive y-axis. The azimuthal angle, ϕ is defined as being 0° in the direction of the positive x-axis, and 90° in the direction of the positive y-axis. The direction of positive and negative z will sometimes be referred to as *forward* and *backward*, respectively. Objects in these halves of the coordinate system will be described as being in the *front* and *back* of the detector, respectively. Because the central part of the ZEUS detector is cylindrically shaped, objects this region will be referred to as in the *barrel*.

The ZEUS detector was built around the HERA beampipe at the nominal interaction point, and was roughly symmetric in ϕ. The most central components were, in order from the beam pipe to the outside, the micro-vertex detector, tracking sys-

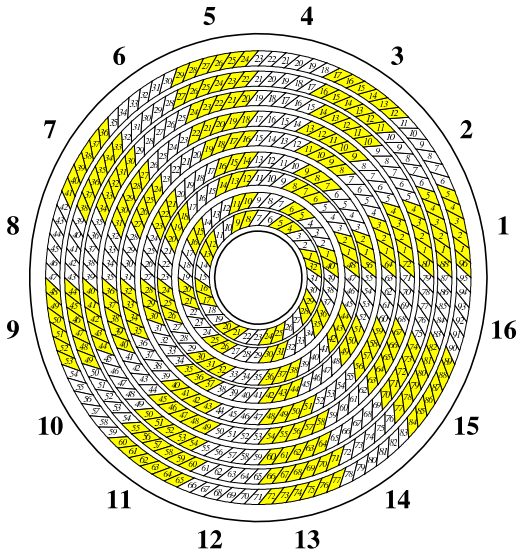

Figure 3.2: A Diagram of The ZEUS CTD, as viewed in the direction of the electron beam.

tem, toroid magnet, and calorimeter. These components were directly used in this analysis and will be described in more detail in the sections which follow. Around the calorimeter are the iron yoke/backing calorimeters, muon chambers, and the concrete encasement. In the negative z direction, in the direction which protons enter the detector, the "veto wall" detector was located to cancel the recording of data caused by particles associated with the proton beam, but not caused by ep interactions.

3.3.1 ZEUS Tracking Detectors

During the period of data taking relevant to this thesis, the tracking system of the ZEUS detector consisted of a silicon vertex detector, Three drift chamber detectors, and a straw-tube tracker. The drift chamber tracking detectors covered three regions: the forward (FTD), barrel, or central (CTD), and rear (RTD). The CTD is of greatest importance to this thesis, and the FTD and RTD will not be discussed here.

The silicon-strip micro vertex detector (MVD), was installed in 2001 during the HERA upgrade shutdown. The MVD was designed to improve the overall precision of the tracking system and allow the identification of events containing secondary vertices from decays of long-lived particles[28]. The MVD was split into two sections: barrel (BMVD) and forward (FMVD).

The BMVD was 64 cm long and covers a polar angle between 30° and 150°. It consisted of three layers of silicon sensors arranged in concentric planes around the interaction point. The inner layer was placed at a radius between 3 and 5 cm from the CTD axis. Because of space restrictions cause by the elliptical beam pipe not being centered on the interaction point, the inner layer did not completely surround the beam pipe in ϕ. The second and third layers were placed at r=8.6 cm and r=12.3 cm, respectively, and each completely surrounded the beam pipe in ϕ. The BMVD was equipped with 600 single-sided strip silicon sensors of approximately 64×64 mm^2 and 320 μm-thick with p+ strips implanted into n-type bulk. Each sensor was covered with 3082 strips with a pitch of 20 μm. Two sensors were glued together next to each other with perpendicular strips on the same side. When placed in the barrel MVD, the sensors parallel to the beam pipe give the $r - \phi$ coordinate of a hit while the perpendicular ones gave the z information.

The FMVD consisted of four planes referred to as wheels, which were perpendicular to the beam axis. The four wheels were positioned at z=32, 45, 47 and 75 cm. Each wheel consisted of two back to back layers of 14 silicon sensors of the same type as in the barrel section but with a trapezoidal shape. There were 480 readout strips per sensor. The FMVD extended the polar coverage of the MVD down to 7°.

The CTD was a cylindrical drift chamber which is filled with a mixture of argon, CO_2 and ethane. It had an active volume with length 205 cm, inner radius of 18.2 cm and an outer radius of 79.4 cm, covering a polar angle range from 15° to 164°. It was divided into eight sections called *octants*, which occupied 45° of azimuthal angle each, spanning the entire length of the CTD, this is depicted in figure 3.2. Each octant was divided into nine radial *super layers*, numbered one to nine, numbered from central to exterior. Each odd-numbered superlayer contained wires which were parallel to the beam axis. Each even-numbered superlayer contained wires which were tilted relative to the beam axis by an angle of 4.98°, −5.53°, −5.51°, and 5.62° for layers 2,4,6,8, respectively. These angles are referred to as a *stereo angle*, because the path of particles which caused a signal in two adjacent superlayers could be identified within 2 mm in the z direction.

The CTD operated in a $1.43T$ magnetic field, which caused charged particles to arc as they passed. The momentum and charge of the particles could then be determined by this curvature. As particles passed though the CTD, they imparted energy to the gas, and their energy loss as a function of distance, $\frac{dE}{dx}$, was also used in particle identification.

3.3.2 The ZEUS Calorimeter

Similar to the Tracking system, the ZEUS uranium calorimeter (CAL) was constructed in three separate parts: forward (FCAL), barrel (BCAL), and rear (RCAL). This is depicted schematically in Figure 3.3.2. These covered polar angles of $2.2° - 39.9°$, $36.7° - 128.1°$, and $128.1° - 176.5°$ respectively. Each of these three main main regions were constructed from independent sections called *modules*, which were fur-

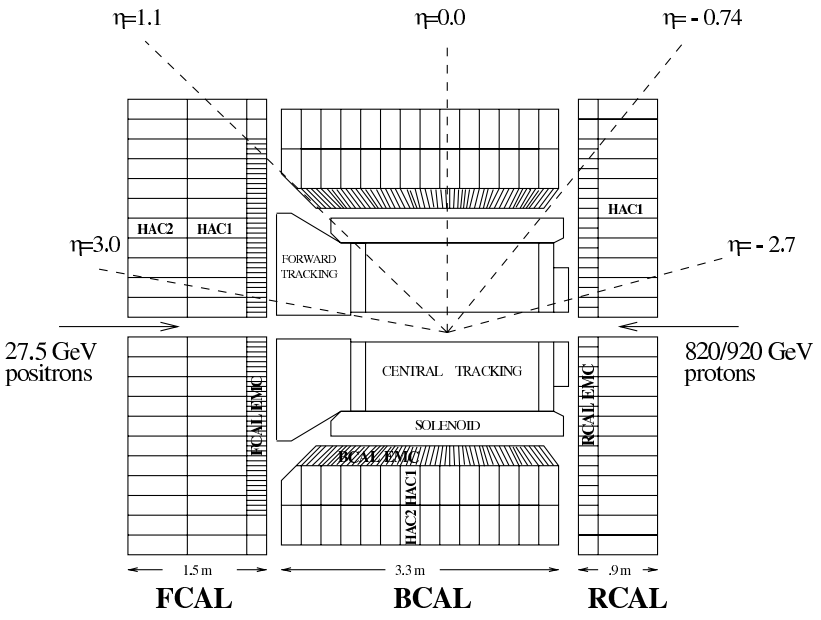

Figure 3.3: A z-y schematic diagram of the ZEUS Calorimeter.

ther divided into sections called *CAL towers*, which were then divided into *cells*. Each tower in the CAL was subdivided into electromagnetic *EMC* or hadronic *HAC* sections. In the FCAL and BCAL Each EMC section contained four longitudinal separations into EMC cells, while each HAC section was transversely separated into two HAC cells. In the RCAL each tower contains only two EMC cells and one HAC. In terms of readout, cells are the most fundamental unit of the CAL. Each cell was roughly shaped like a rectangular prism, and was constructed of alternating layers of 3.3 mm thick absorber plates and 2.6 mm thick plastic scintillator. Each absorber plate was constructed by encasing the depleted uranium ^{238}U in a steel jacket. Incident particles on the absorber showered, producing many more particles, which stimulated the scintillator tiles, producing light. Light from the scintillators was passed from two opposite sides of each cell along two separate wavelength shifters. Each wavelength

shifter was attached to one photo-multiplier tube (PMT), located on the exterior of the CAL. The two PMTs for each cell were labled as *left* and *right*. Using timing information between left and right channels for each cell, improvement in three dimensional positioning could be made. The agreement between pairs of PMTs also allowed a systematic check of response, and redundancy in case of noise.

^{238}U was chosen as absorber material for its density, stability, radiation-hardness and its own natural low level radiation. This low radiation provided a stable and well understood signal for calibration of the readout. Hadrons incident on ^{238}U create a high number of spallation neutrons, which can then excite the hydrogen nuclei of a scintillator. Electrons do not radiate the same manner because they mostly interact with atomic electrons, rather than nuclei. These EM interactions typically produce photons and e^+e^- pairs. The CAL was designed with a careful balance between the quantity of uranium and steel in each absorber plate which allowed the CAL to reach a nearly equal response from hadronic and leptonic energy. Test beam studies showed the response to be equal within 3%. This is important for jet physics, because it removes the need for assumptions about the leptonic and hadronic content of jets. The single particle energy resolution for electrons and hadrons was determined in test-beams to be $\frac{\sigma_E^e}{E} = 18\%/\sqrt{E}$ and $\frac{\sigma_E^h}{E/\mathrm{GeV}} = 35\%/\sqrt{E/\mathrm{GeV}}$, respectively [29]. This can be contrasted with the equivalent H1 energy resolutions of $\frac{\sigma_E^e}{E} = 12\%/\sqrt{E}$, $\frac{\sigma_E^h}{E} = 50\%/\sqrt{E}$ [30, 31].

3.3.3 Luminosity Monitor and Polarimeters

The *luminosity* of a data sample, $L = N/\sigma$, is defined as the number of particles produced from a process, divided by the cross section for that process. Thus in order

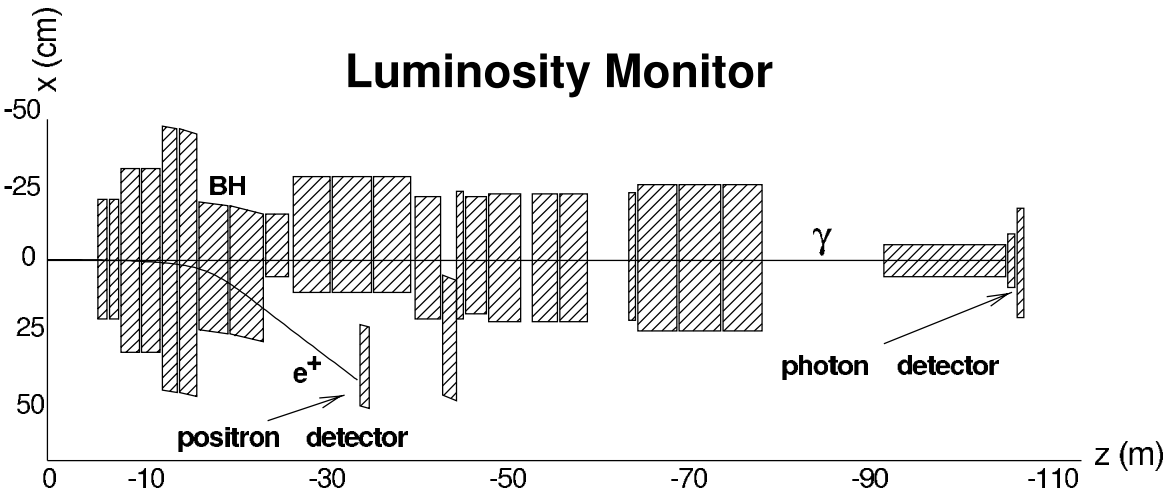

Figure 3.4: Schematic of the ZEUS Luminosity System.

to determine a cross section from experimental data, one must know the luminosity used to generate that measurement. At HERA, the luminosity of ep collisions was determined by measuring the rate of Bremsstrahlung photons from the Bethe-Heitler process $ep \to ep\gamma$. The theoretical cross section for this process is known to an accuracy of .5%, so a precise measurement of this process allowed a precise measurement of the luminosity.

The Bethe-Heitler measurement was performed at -107 m in the ZEUS coordinate system by a lead-scintillator calorimeter, depicted in Figure 3.3.3. The lumi-γ system, gathered photons with a polar angle $\theta_\gamma < 0.5$ mrad with an test-beam energy resolution of $18\%/\sqrt{E}$ [32]. It was determined that the protective carbon/lead synchrotron radiation filter caused a slight degradation of performance to $18\%/\sqrt{E}$. The lumi-γ detector had 1cm scintillator strips located $.7\chi_0$ inside, granting the ability to resolve the impact position of photons to .2cm in x and y. This system was also used to measure the electron beam-tilt and measure photons from initial-state radia-

tion (ISR). In addition to the lumi-γ calorimeter, a second lead-scintillator calorimeter called lumi-e was located at $-27m$, which captured electrons which were deflected from the beam by the HERA bending magnets. This was originally designed to compliment the lumi-γ system, but was found to be unnecessary for luminosity measurement. The total uncertainty in the luminosity measurement was determined for this analysis to be 2.5%.

The electron beam polarization was measured using two independent polarimeters, referred to as the longitudinal polarimeter (LPOL) [33, 34] and transverse polarimeter (TPOL) [35, 34]. Both devices exploited the spin-dependent cross section for Compton scattering of circularly polarized photons off of electrons. The polarimeters were able to measure the polarization in times much shorter than the polarization build-up time. The two independent devices were found to agree with each other within 2% [36]

3.3.4 Veto Wall and C5 Counter

The veto wall is was a large wall of iron positioned -7m, designed to shield the ZEUS detector from particles produced in the proton beam halo. It measured $8 \times 7.6 \times 0.86$ m, with a square hole of dimension 0.95 m at the center to accommodate the beam pipe and magnets. Scintillators on either side of the wall provided information about the rate of incident particles, allowing veto information for events contaminated by these particles. The C5 counter was a scintillator attached to the C5 collimator at $z = -3.15$ m which provided timing information used to synchronize the HERA and ZEUS clocks. The C5 counter also provided veto information for beam halo

interactions.

3.3.5 Trigger and Data Acquisition

Assuming that ZEUS recorded one event from every crossing, it would have produced data at a rate of approximately 1 MB $\times$ 10MHz= 10TB/s. Because the data transmission from the detector to the event reconstruction computing farm (described in the next section) was less than 1MB/s, the rate of data was forced to be reduced by a factor of 10^6. A faster transmission rate would not have been beneficial, because not every crossing produced an *ep* interaction, and some that did produced products deemed uninteresting, or which were contaminated by signal from non-*ep* sources. Deciding which events were worth full reconstruction and storage was accomplished by the a 3-level trigger system, depicted in Figure 3.3.5. The ZEUS First Level Trigger (FLT) was a digital hardware trigger, designed to reduce the event rate to $1kHz$. In order to hold the data while electronics make a decision, raw data was stored on the detector in an analog pipeline for $5\mu s$. This allows a decision to move data off the detector to be made roughly every 50 bunch crossings. The time during the first 25 of these 50 crossings is allocated to individual component FLTs. The rest of the cycles are given to the Global First Level Trigger (GFLT), which collected decisions from the subdetector-specific FLTs, and issued global accept or abort requests. This was performed with almost zero deadtime. If a particular event was accepted by the FLT, it was then digitized and transferred to the Second Level Trigger (SLT). Due to finite transfer of data between the components deadtime occurs here at $1-2\%$ The SLT used more complete information than the first level trigger. It was designed to reduce the event rate to less than $100Hz$. Similarly to the FLT, each subdetector has its

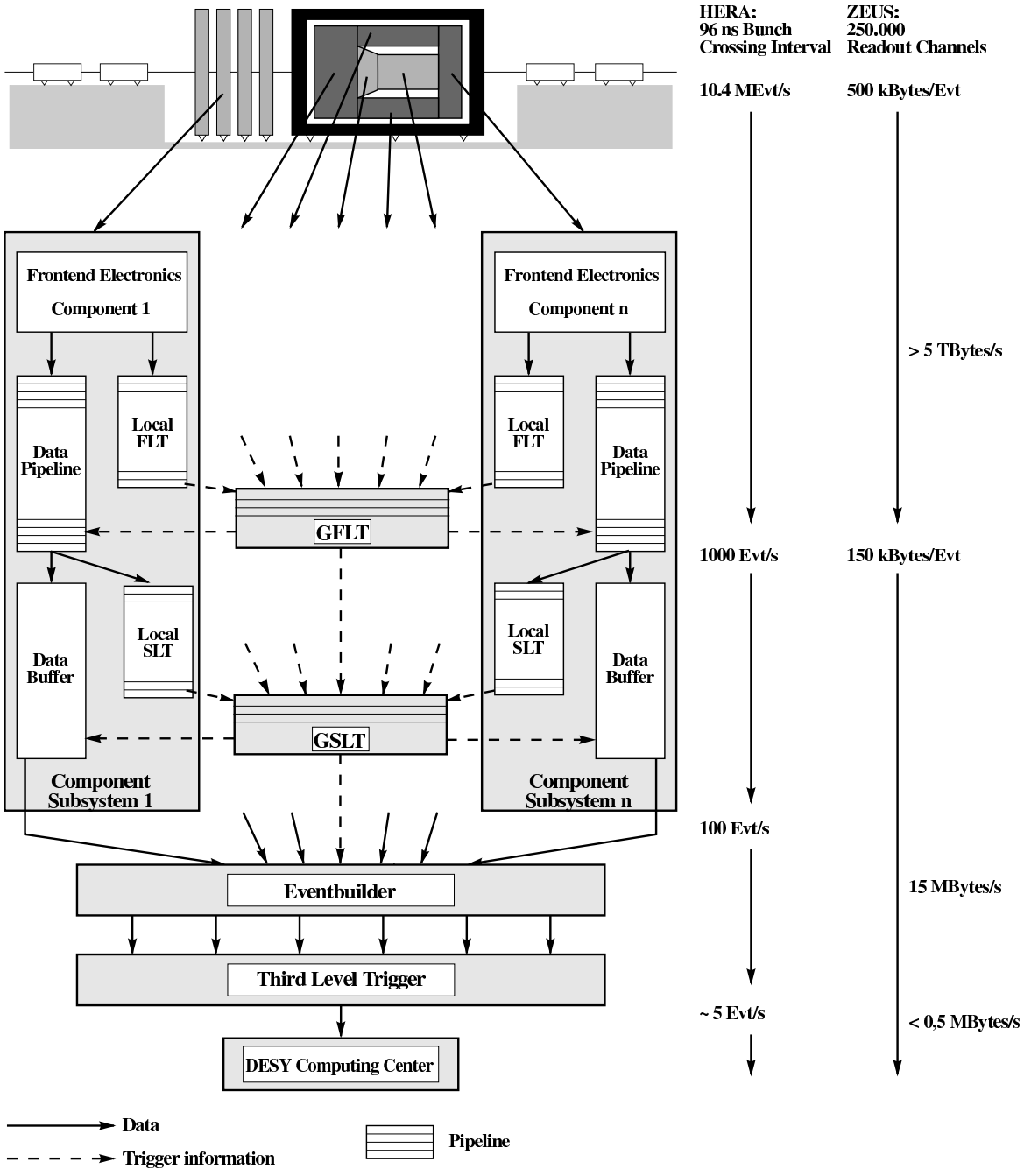

Figure 3.5: Schematic of the ZEUS System System.

own SLT which passes information to the Global Second Level Trigger (GSLT). If the event is accepted by the SLT, all components send all information to the event builder (EVB), which then combines all data into a single event record to ADAMO database tables.

Data was then passed to the Third Level Trigger (TLT), which was a purely software based trigger. The TLT partially reconstructed kinematic variables, and reduced the eventrate to 1Hz. If the event was accepted by the TLT, then it was passed to the ZEUS Physics Reconstruction Program (ZEPHYR), which uses calibration constant tables for each component to interpret detector signals as energies, times, and positions, and the event was written to data tape for storage and analysis.

Chapter 4

Event Reconstruction

Events from the ZEUS detector which passed the FLT, SLT and TLT triggers were written to tape for storage and later analysis. Reconstruction of events begins with the EVB (see section 3.3.5.) which combined all detector signals from the event into a single ADAMO table entry. Entries were then processed by the ZEPHYR program, which used calibration constant tables for each component and each run to interpret detector signals as energies, times, and positions. Offline analysis in this work was performed using the ORANGE (Overlying Routine or Analysis Ntuple GEneration) software framework, which is based on EAZE (Effortless Analysis of ZEUS Events). ORANGE and EAZE provide routines which retrieve data records, perform specialized and modifiable reconstruction of event variables, integrate the CERN libraries, and perform basic event selections.

4.1 Track and Vertex Reconstruction

While the nominal interaction point for *ep* interactions is at the origin of the ZEUS coordinate system, finite dimensions of the beam bunches caused real interactions to occur with a spread in all three dimensions. Information from the tracking

components of the ZEUS detector were used to reconstruct the tracks of individual charged particles and estimate the location of the initial ep interaction. This is performed using the VCTRACK [37] program. The VCTRACK package uses information from all tracking detectors, with primary information coming from the CTD. Track finding begins with CTD seeds, each of which contains three neighboring hits in the outermost axial superlayers of the CTD. Each seed is extrapolated iteratively towards the inner superlayers, aided by a "virtual hit" which is fixed to the beam line. As hits are added to the tracks, trajectory parameters of each track are recalculated with each iteration. Tracks that share 15% or more of their hits with other tracks at any stage are removed. An initial estimate of the z-position of each hit from the z-by-timing information is used, which is later refined using stereo superlayer hits. The next step of reconstruction proceeds by extrapolating the innermost hit of each track outward. Fitted tracks are then used as input to an algorithm which tests candidate primary and secondary vertices. Vertices are then chosen based on a χ^2 minimization routine, and tracks matched to the primary vertex are then refitted using the primary vertex as a starting point. For all events in the study, the x and y vertex positions were set to 0 after track fitting and electron finding, which is described in section 4.3.

4.2 Calorimeter Reconstruction

Information from the ZEUS calorimeter was used to reconstruct the energies and positions of particles. Each cell provides pulse amplitude and timing information from two PMTs, which are compared to ensure accuracy and provide improvements in position reconstruction. Several sources of uncertainty enter the calorimeter reconstruction. These include noise from uranium absorber decays, noise from readout elec-

tronics and PMT discharges, which occurred when the high voltage from a PMT base discharged spontaneously to the encasement. The behavior of each PMT was monitored during operation and calibrations to ensure proper functioning, PMTs listed in a table of unreliable PMTs for each run were ignored during reconstruction. To suppress uranium radiation in reconstruction, EMC cells with $E < 80$ MeV and HAC cells with $E < 140$ MeV were neglected. To suppress PMT discharge signals, cells were ignored if the imbalance between left and right PMTs, $I_{\text{cell}} = \left|\left(E_{\text{L}} - E_{\text{R}}\right) / \left(E_{\text{L}} + E_{\text{R}}\right)\right| > 0.7$, and that cell had an average energy greater than 700MeV. Cell selection was performed in this analysis by the ZEUS Noise04s routine.

Simulations of the energy response of the CAL differ from that of the true response [38]. While this could be corrected by adjusting the energy values of the simulation, historically this is performed by altering the final CAL cell energies in the ZEUS data. For each FEMC cell, the energy was multiplied by a factor of 1.024. The same procedure was performed using factors of 0.941 for FHAC, 1.053 for BEMC, 1.096 for BHAC, and 1.022 for all RCAL cells. No adjustment to calorimeter cell values was applied to MC events.

4.3 Electron Reconstruction

A major source of background to CC DIS is NC DIS, which has a principle signal as an isolated electron deposit located in the calorimeter. In order to reject events arising from NC interactions, the electron finder Sinistra95 [39] was applied to all events. Sinistra is a neural network which has been trained on simulated low-Q^2 NC DIS data to produce the best separation between electromagnetic and hadronic energy deposits by using the properties of shower profiles to establish the characteristics of

the initiating particle.

Scattered particles such as single electrons often deposit their energy into more than one calorimeter cell, and often in ways which involve cells in both the BCAL and RCAL. Before input into SINISTRA, groups of calorimeter cells called *islands* [39] were formed, where each island is a potential deposit from an electron. The 17 inputs to the neural network were the total energy of the cells in the island, and 16 showering profile parameters called Zernike moments and Legendre functions. The output of SINISTRA is a real number between 0 and 1, which is interpreted as a likelihood that the island in question resulted from an isolated electron. Clusters with SINISTRA output near one are considered to be electron-like. In this analysis, only the candidate with greatest SINISTRA likelihood was considered, and events were only considered to have a candidate if the likelihood was greater than 0.9. The reconstructed energy of an electron candidate was the sum of the cell energies in its island, and the position of the candidate was determined from the energy weighted island center. For candidates with likelihood greater than 0.9 and energy greater than 10GeV, SINISTRA was estimated to have 80% purity and nearly 100% efficiency [40].

4.4 Kinematic Reconstruction

Basic kinematic quantities were reconstructed from the calorimeter energy deposits, which were treated as massless particles.

$$\text{Total energy} \;:\; E_{\text{CAL}} = \sum_i E_i \tag{4.1}$$

$$\text{Longitudinal momentum in the CAL} \;:\; p_z = \sum_i p_{z,i} \tag{4.2}$$

$$\text{Transverse momentum in the CAL} \;:\; p_{T,\text{CAL}} = \sqrt{\left(\sum_i p_{x,i}\right)^2 + \left(\sum_i p_{y,i}\right)^2} \tag{4.3}$$

$$\text{Cosine of hadronic system angle} \;:\; cos\gamma_h = \frac{p_T^2 - (E-p_z)^2}{p_T^2 + (E-p_z)^2} \tag{4.4}$$

In charged current interactions at ZEUS, the exiting neutrino escapes detection, requiring kinematic quantities to be reconstructed from the hadronic system alone. To prevent bias in our estimation of these values due to particles which escape detection down the beam pipe, the Jaquet-Blondel method [41] of reconstruction was used. This method relies only on the transverse momenta, p_T and difference in energy and z-component momenta, $E - p_z$ of each particle, which are small for particles scattered near the beamline. The reconstructed values of Q^2, x, and y are:

$$\begin{aligned} y_{\text{JBCAL}} &= \frac{E-p_z}{2E_e} \\ Q^2_{\text{JBCAL}} &= \frac{p_{T,\text{CAL}}}{1-y_{\text{JBCAL}}} \\ x_{\text{JBCAL}} &= \frac{p_T}{s y_{\text{JBCAL}}(1-y_{\text{JBCAL}})}. \end{aligned} \tag{4.5}$$

4.5 Jet Reconstruction

Calorimeter cells were combined in the laboratory frame using the k_T cluster algorithm [42] to form jets of calorimeter cells. The algorithm was also used to clus-

ter jets of hadrons and partons in the simulations, so in this section we will refer only to "objects" being clustered for generality. All clustering objects were considered massless. The algorithm defines the distance of each particle from the beam line as $d_i = E_{T,i}^2$, and the distance between two objects as $d_{ij} = \min\left(E_{T,i}^2, E_{T,j}^2\right) \times \left[(\eta_i - \eta_j)^2 + (\phi_i - \phi_j)^2\right]$. The algorithm begins by identifying $\min(d_i, d_{ij})$. If $d_{kl} = \min(d_i, d_{ij})$ for some k, l, then objects k, and l are merged into a cluster (here indexed as m) with properties

$$\begin{aligned} E_{T,m} &= E_{T,j} + E_{T,k} \\ \eta_m &= \frac{E_{T,j}\eta_j + E_{T,k}\eta_k}{E_{T,j} + E_{T,k}} \\ \phi_m &= \frac{E_{T,j}\phi_j + E_{T,k}\phi_k}{E_{T,j} + E_{T,k}}. \end{aligned} \tag{4.6}$$

If $d_n = \min(d_i, d_{ij})$ for some n, then object n is considered a jet, and no longer participates in the merging procedure. In this analysis, the k_T algorithm was applied in the lab frame in inclusive mode, meaning that all objects are merged into jets. Phase space requirements were applied to each jet, neglecting objects outside acceptance or poor reconstruction, which is described in section 6.3.3.

The k_T algorithm is an alternative to the cone algorithm [43], which is primarily used in hadron-hadron colliders. The cone algorithm begins by selecting high-E_T deposits as seed jets. Other objects contained in an $\eta - \phi$ cone of a given radius are considered as belonging to a single jet. The angle of a given cone is then modified to maximize the E_T contained within, or to match the jet-axis with the cone-axis. This algorithm has ambiguities resulting from the choice of minimum seed E_T, as well as the prescription to resolve overlapping cones. The algorithm also is infra-red unsafe, meaning that the jet-cross section diverges as the seed threshhold is lowered. The

resulting jets can be dramatically different between two events differing only by low E_T QCD radiation. The algorithm requires vary little processing power, however, and was used to select events at the third level trigger, as will be described in section 6.2.3. In all other parts of this thesis, all jets are found using the k_T cluster algorithm.

Chapter 5

Event Simulation

The calculations presented in chapter represent jets of partons, while the data which were collected represent jets of hadrons. In order to compare these, we must translate the predictions of partons onto predictions for hadrons. Moreover, the data as immediately taken from the readout includes detector specific effects which we must correct for in order to compare our data with predictions, or with other experiments. In order to accomplish these two goals, Leading Order MC (MC) simulations were employed. The MC used here simulates individual events in the ZEUS detector in several steps.

For each event, points in a predetermined phase space are selected, and leading order electron-quark matrix elements are combined with a PDF parametrization to produce a list of partons for the event. This is referred to as the hard scatter, and the information about this list of exiting partons is said to describe the event at the *parton level*. Then, a phenomenological model is employed to approximate hadronization for the partons, and the resulting list of hadrons is said to describe the event at the *hadron level*. Lastly, a complete simulation of the detector, including material interactions, magnetic fields, detector components, trigger, and data readout is used to simulate how the detector would respond to each event. The information produced by the detector

simulation is of the same structure as the data taken from the actual detector, and is analyzed in the same way. This information is said to describe the event at the *detector level*.

5.1 PDF and Hard Scatter

The incoming state of the simulated event is an electron and proton, which will interact via the protons partons. Which flavor parton will interact, and the x and Q^2 values of the interaction is determined by the proton PDFs and a pseudorandom number generator[1]. The PDFs used in the MC were the CTEQ5D PDFs described in section 2.6. The relative probability of processes were computed to leading order, which were stored in tables for efficient recall. Pseudorandom numbers are generated select from these processes. This component represents the hard scatter, after which the event contains an outgoing neutrino, one or two outgoing quarks or one gluon. and the proton remnant. The available outgoing states in the MC used in this analysis are depicted by the Feynman diagrams shown in section 2.3. All MC presented in this thesis used unpolarized matrix elements.

5.2 Parton Cascade

As described in section 1.4, quarks and gluons are not observed in the detector, but instead undergo QCD radiation and hadronization. QCD radiation of hard-scatter partons is also called parton showering, and is an intrinsically non-perturbative pro-

[1]A pseudorandom number generator is a deterministic algorithm for the production of numerical sequences which satisfy some statistical tests of randomness, such as uniform frequency and distribution of the numbers produced.

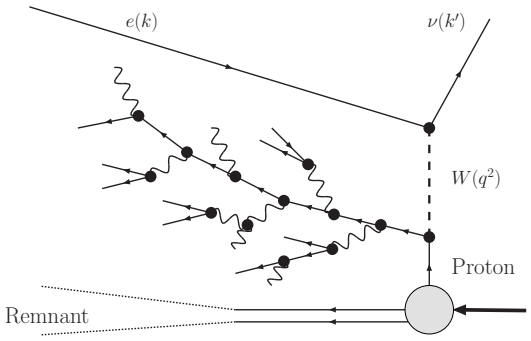

Figure 5.1: Schematic of MEPS

cess due to the low scales involved. Two methods of simulating a parton cascade will be considered here: Matrix-Element plus Parton Shower (MEPS) [44], and the Color Dipole Model (CDM) [45]. The MEPS approach generates parton showers from the DGLAP splitting functions. Partons become less virtual as they radiate and split until a predetermined virtuality is reached, typically on the order of 1 GeV. This is represented in figure 5.1. Because the parton shower uses the DGLAP evolution equations, radiation is ordered strongly in decreasing k_T and increasing proton fractional momenta. MC samples generated by the LEPTO 6.5 program [46] MC presented in this thesis employ MEPS as implemented via JETSET 7.4 [44, 47].

CDM describes the proton remnant and its dissociated parton as a color dipole. As the parton and remnant separate, the dipole energy increases until sufficient energy is reached to radiate a gluon, which bifurcates the dipole. The two halves continue to stretch and split as more gluons are emitted. Unlike MEPS, CDM does not order its radiation in k_T. Samples of ARIADNE 4.08 [48] MC presented in this thesis employ CDM. This is represented in figure 5.2.

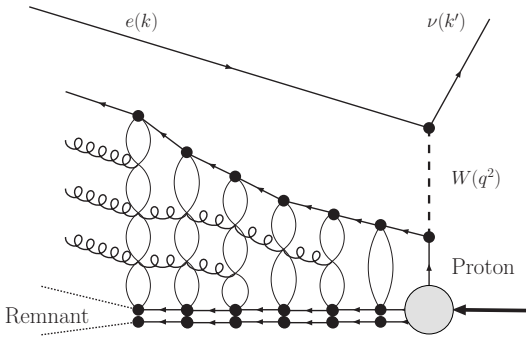

Figure 5.2: Schematic of CDM

5.3 Hadronization

Free partons are never observed due to color confinement, so the partons simulated during the cascade phase discussed in section 5.2 must be converted into color singlet hadrons in order to describe physical data. This process is referred to as hadronization. Because it describes confinement, at scales of ($\mu \lesssim 1$ GeV) where α_s is large, it necessarily cannot be described by perturbative QCD. Several hadronization models are currently implemented in MC models, but only the Lund String Model [49] is used in the MC results presented in this thesis.

In the Lund String Model, the color field between a $q\bar{q}$ pair is represented as a linear potential, described as a flux-tube or string of gluons. Spatial stretching of this string results in a potential energy of $\approx$ 1 GeV/fm. If the initial $q\bar{q}$ pair separate sufficiently the color field will contain enough potential energy to produce a new $q\bar{q}$ pair. This is described in the model as occurring between the initial $q\bar{q}$ pair, as if the string had been cut. This mechanism produces quarks with an approximately Gaussian p_T spectrum. This process continues until some preset cutoff, when the

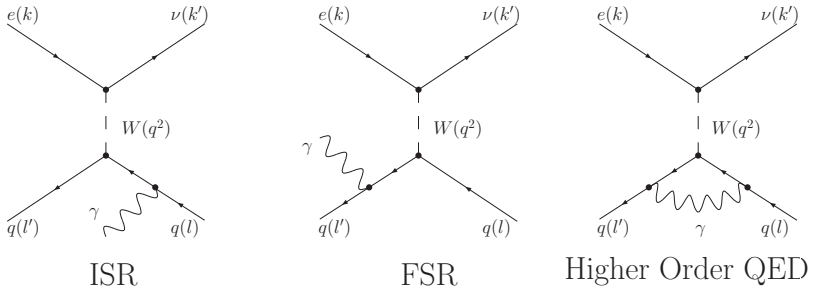

Figure 5.3: Feynman Diagrams for Higher Order QED Effects

$q\bar{q}$ pairs have small enough relative kinetic energy to be considered on-shell hadrons. Groups of 2 and 3 quarks are then chosen to form mesons and hadrons.

5.4 Description of Initial- and Final-State QED Radiation

While MC models can generate interactions at fixed electron and proton energies. HERA data were produced with a broader kinematic spectrum, however, because of radiation of photons immediately before and after the hard interaction, as shown in figure 5.3. This type of process is referred to as initial- and final-state radiation (ISR/FSR). For this analysis, the MC implementations used for event simulation were interfaced with the HERACLES 4.6.1 [50] program via DJANGO v1.3 [51]. The HERACLES program includes QED effects up to $\mathcal{O}(\alpha_{\mathrm{EW}}^2)$. The physical parameters used to compute QED effects were identical as those used for the pQCD calculations, stated in section 2.3.

5.5 Detector and Trigger Simulation

Once an event has been simulated to produce real particles with definite momenta, these particles are used as input into a full detector simulation. This simulation

includes potential decays of short lived particles, the interactions with the active and passive materials in the detector, and the response of the electronics at all levels in the data-taking and reconstruction chain. Information for the modeling of the detector response comes from test-beam data, and the simulation is referred to as the MC *for ZEUS Analysis, Reconstruction and Trigger* (MOZART v2005a.1), which is based on GEANT v3.21[52].

The trigger simulation, called Complete ZGANA[2] Analysis Routine (CZAR v2005b.2) provides complete description of the ZEUS trigger system response to simulated events. The output of MOZART and CZAR is an table of detector signals which is organized similarly to data from the ZEUS detector. The principle difference from real data is the additional information about the generator, parton, and hadronic portions of the simulation. These ADOMO tables were then submitted to the ZEPHYR program discussed in the beginning of chapter 4, and were reconstructed identically as the data were. This type of information is referred to as being at the *detector level*.

[2]The ZEUS GEANT Analysis (ZGANA v1.5) and TLT_ZGANA are simulations of the ZEUS 1st+2nd and 3rd trigger systems, respectively. CZAR is the combination of the two, encompassing the complete trigger chain.

Chapter 6

Event Selection

6.1 Description of Data Sample

The data in this thesis were collected during the years 2004 to 2007. During this time, HERA provided collisions between protons and longitudinally polarized electrons (2005-2006), and between protons and longitudinally polarized positrons (2004, 2006-2007). Because several depolarizing effects existed, and these could not be precisely controlled, the lepton beam polarization varied substantially from run to run, and was always below the theoretical maximum of 92.4% [53]. The absolute value of the observed value was almost always below 50%, with a luminosity-weighted average of -27% and +30% (-37% and +32%) for left- and right-handed e^-p (e^+p) data, respectively. The luminosity collected for left- and right-handed e^-p (e^+p) collisions was 106 pb$^-$1 and 74 pb$^-$1 (77 pb$^-$1 and 102 pb$^-$1), respectively.

6.2 Online Event Selection

As described in section 3.3.5, event selection during data taking was performed via a three level trigger system. As events were produced in the ZEUS detector,

The trigger system was responsible for the decision to offload, reconstruct, and store event data from the detector. The two concerns of trigger selection choice is that the selection be *efficient*, and *pure*. Efficiency refers to the probability that a desired event was triggered, while purity refers to the probability that a triggered event was desired. Thus, a balance was chosen between overly loose selection criteria which selected signal with additional background, and overly stringent criteria which rejected background at the cost of diminishing signal.

Two independent trigger selections were used in this analysis, and are referred to throughout as the *principle* and *alternative*. The principle trigger selection was used to extract the cross sections, while the secondary was used to understand the systematic uncertainty introduced from trigger choice and operation. The principle selection has been previously tested and used in an inclusive HERA II CC DIS ZEUS publication [54]. The alternative trigger selection is derived from a HERA I CC DIS Jets publication [55]. The primary difference between then two is that the alternative selection required the presence of jets, while the principle selection made no such constraint. The principle selection also heavily relied on tracking quantities, while the secondary relied more heavily on the calorimeter.

6.2.1 First Level Trigger Selection

The core conditions of both the principle and alternative FLT selections is the presence of large E_T in different subsections of the CAL, and the presence of CTD tracks which are consistent with ep interactions. The primary purpose of these requirements was to select ep events without reading data from the detector for every bunch crossing. Both selections also rejected events if deposits and timing information

was consistent with beam-gas interactions.

For both selections, events were accepted by the FLT if the event had an E_T greater than 30 GeV, and no beam-gas signature was seen as described in section 1.9. Lower values of E_T were required if a well reconstructed track was present, or if the energy deposit was not close to the beampipe. Events were also triggered if the $P_T^{\rm miss}$ observed was 5, 8, 11.5 GeV, depending on various other calorimeter and tracking conditions. A detailed list of trigger bits and their physical meanings is given in appendix E.1.

6.2.2 Second Level Trigger Selection

One challenge of designing a trigger selection for CC DIS is that the signature of large $P_T^{\rm miss}$ and E_T are also produced by beam-gas interactions. beam-gas typically deposits its energy near the beam pipe, so it is useful to select events based on the $P_T^{\rm miss}$ and E_T not including these CAL cells. Thoughout this chapter, $E_T(-2IR)$ ($E_T(-1IR)$, $P_T^{\rm miss}(-1IR)$) will refer to the transverse energy as measured by the CAL excluding the inner two rings (one ring) of cells closest to the beam pipe. The variable $N_{\rm gt}$ refers to the number of "good" tracks in the sense that they are reliably reconstructed, and originate from an area near the nominal vertex. This definition is specific to the ZEUS CTD, and is based on the number and distribution of hits used in the track fit. The requirement that the tracks come from near the nominal vertex helps differentiate between *ep* interactions and beam-gas, because beam-gas events often have tracks originating far from $z = 0$. In the principle SLT selection, events were required to satisfy the each of the following three conditions.

1. Proper timing and number of hits in the CTD

2. No deposits from off-momentum protons were detected

3. At least one of the following:

   (a) $P_T^{\rm miss} > 6$ GeV and $E_T(-2IR) > 6$ GeV and $N_{\rm gt} > 1$

   (b) $P_T^{\rm miss} > 9$ GeV and $P_T^{\rm miss}(-1IR) > 8$ GeV and $E_{FCAL} > 20$ GeV

   (c) $P_T^{\rm miss} > 9$ GeV and $(P_T^{\rm miss})^2 > 2.31 \times E_T$ and $E_{FCAL} > 80$ GeV

   (d) $E - p_z > 6$ GeV and $(P_T^{\rm miss})^2 > 2.25 \times E_T$ and $N_{\rm gt} > 1$

Conditions 1 and 2 above attempt to reject non-*ep* events. Conditions 3a and 3b selected events with large $P_T^{\rm miss}$ without being sensitive to beam-gas. Condition 3c selected events with $P_T^{\rm miss}$ large relative to the E_T of the event. This helped select CC DIS over PHP, as discussed in section 1.9.

The alternate selection required that all the following conditions were met:

1. $N_{\rm gt} > 1$

2. $P_T^{\rm miss} > 8$ GeV

3. $E_T(-1IR) > 8$ GeV

4. $P_T^{\rm miss}/E_T > 0.3$

In the above criteria, criteria 1 selected *ep* events, while selection 2 and 3 selected CC DIS over NC DIS. Selection 4 selected CC DIS over PHP.

A more detailed explanation of these criteria is given in table E.2.

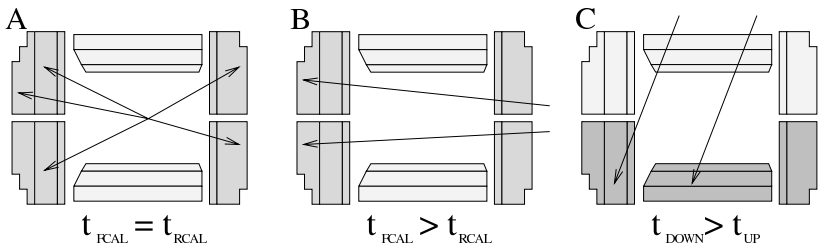

Figure 6.1: Schematic diagram of CAL timing information. Major scenarios include: A) Events originating near the nominal vertex. B) Events originating outside the detector near the beam-pipe. C) Events originating outside the detector far from the beam pipe.

6.2.3 Third Level Trigger Selection

In this section, the term *up-down CAL time difference* is used to indicate the difference of the time in which CAL hits were recorded in the upper and lower halves of the CAL. Quantities comparing CAL timing information are useful quantity because events originating in the center of the detector have $t_{\rm up} \approx t_{\rm down}$ and $t_{\rm RCAL} \approx t_{\rm FCAL}$, as depicted in figure 6.1 A. cosmic and halo muons enter the detector from outside, creating a different signature in these values, as depicted in figure 6.1 B and C.

The principle selection was satisfied if all of the following conditions were met:

1. $P_T^{\rm miss} > 6$ GeV
2. $|z_{vtx}| < 60$ cm
3. Up-down CAL time difference which was indicative of an interaction originating within the detector. The events were rejected if the time difference exceeded 8 ns.

The third condition compares the timing information from the upper and lower half of the calorimeter. This condition rejected cosmic rays, which often come from above

the ZEUS detector. The event was also accepted if all of the following conditions were met

1. $P_T^{\text{miss}} > 6$ GeV
2. $\left(E_{FCAL} > 10 \text{ GeV} \parallel N_{\text{gt}} > 0\right)$
3. No particles lost from accelerated bunches were measured in the detector.
4. If the reconstructed vertex was less than -80 cm from the nominal interaction point, and fewer than five tracks originating from the vertex if the z-position exceeded -80cm from the nominal interaction region.
5. Fewer than 25 tracks were observed, and if more than 25 were observed, no more than 8 of these led to some vertex -80cm from the nominal interaction point.
6. $\left(N_{\text{hits}}^{\text{CTD}} < 2500 \parallel P_T^{\text{miss}} > 10 \text{ GeV}\right)$
7. Up-Down CAL time difference which was indicative of an interaction originating within the detector, in which the upper and lower parts of the CAL recorded a time difference less than 8 ns

The alternative trigger accepted the event if $P_T^{\text{miss}} > 8$ GeV, and either $E_T(-IR) >$ 8 GeV, one jet found with the cone algorithm [43] such that $E_T^{\text{jet}} > 8$ GeV, or one k_T [42] jet was found such that $E_T^{\text{jet}} > 8$ GeV. This is the only condition in this thesis where cone jets were considered. At all other points, a jet refers explicitly to jets found using the k_T cluster algorithm. These jetfinding algorithms are described in detail in section 4.5.

When an event satisfied the trigger selection criteria, it was written to data tape for storage and later analysis.

6.3 Offline Event Selection

The selection criteria applied to events after triggering can be separated into three categories: Preselection, in which loose cuts are applied to speed analysis, cleaning selections, in which background and poorly reconstructed events are rejected, and phase space selection, in which events are selected with desired kinematic and jet properties.

6.3.1 Preselection

The performance of the ZEUS detector, luminosity monitoring systems and polarization monitoring systems varied during data taking. The ZEUS reconstruction library contains a dedicated functions which indicated wether the ZEUS detector subcomponents were in proper functioning order at the time the event was recorded, and events taken with all central components properly functioning were only used in this analysis. MC events were not subject to these selections.

The two devices used for measuring the lepton beam longitudinal polarization, LPOL [33, 34] and TPOL [35, 34], which are described in section 3.3.3, produced comparable but different measurements of the average polarization during each data taking run. The device chosen for each data taking run was based on which one was functioning properly for a longer period of that run. If LPOL (TPOL) was functioning longer for that run, then each data event was only selected for analysis if the LPOL (TPOL) was indicated as functioning properly the time that event was recorded. The

average polarization value and integrated luminosity for each data taking run was exclusively taken from the LPOL (TPOL).

Events were required to have $P_T^{\rm miss} > 9$ GeV, $P_T^{\rm miss}/E_T > 0.3$, and at least one calorimeter jet within $-1 < \eta^{\rm jet} < 2.5$ and $E_T^{\rm jet} > 3$ GeV, where $E_T^{\rm jet}$ was computed purely from CAL cell energies as stored on tape. These cuts are less restrictive forms of those applied later, and the jet cuts are described in section 6.3.3 in detail. Events meeting all these criteria were selected for more detailed analysis.

6.3.2 Signal Selection and Background Rejection

This section describes selection cuts which were applied both to select signal and reject background. The principle signal of CC DIS is missing transverse momenta, due to the neutrino which escapes detection. Many other types of *ep* and non-*ep* events create this signature in the detector, such as CAL PMT base discharges, cosmic or halo muons, and particles which escape down the beam pipe at a low angle. Thus, many other selection cuts are required to remove events from these sources.

All detector level events were required to have a $p_T^{\rm CAL} > 11$ GeV as measured by the CAL without any corrections applied. This both selected CC DIS events, and ensured trigger efficiency, because almost all trigger conditions were set to a $P_T^{\rm miss}$ much lower.

Because the phase space of jets found in the analysis aimed at reaching to $\eta^{\rm jet} \equiv 2.5$, while the CTD acceptance begins to deteriorate at $\eta \equiv 2$, special tracking requirements were formed to differentiate these two cases.

As described in section 6.3.1, all events were required to have a jet before being retrieved from tape. Only k_T cluster objects with $E_T > 3$ GeV as recorded by the CAL

were defined as jets. Events where the jet with the highest $E_T^{\rm jet}$ satisfied $\eta^{\rm jet} > 2$ are referred to as *forward-jet events*. Forward-jet events events have many tracks outside the CTD acceptance, and are treated specially.

Non-forward-jet events were expected to have many tracks within the CTD, and geometric information in the CTD and CAL were expected to agree. Selection requirements for non-forward-jet events were

1. $N_{\rm gt} \geq 1$, where $N_{\rm gt}$ is the number of *good tracks*[1] in the CTD. These tracks were reconstructed with high purity, which enabled the reliable reconstruction of the event vertex.

2. $|\phi^{\rm CTD} - \phi^{\rm CAL}| < 1$ rad, where $\phi^{\rm CTD}$ is the azimuthal angle of the net momentum from tracks in the CTD and $\phi^{\rm CAL}$ is the azimuthal angle of the net momentum from cells in the CAL. This selection cut removed events where a cosmic or halo muon deposited energy in the CAL during an *ep* event.

3. $p_T^{\rm CTD} > 0.1 \times p_T^{\rm CAL}$ or $p_T^{\rm CAL} > 25$ GeV. This selection cut removed events where a cosmic or halo muon deposited energy in the CAL during an *ep* event.

Forward-jet events were exempt from these requirements, but the transverse momentum requirement for these events was tightened to $p_T^{\rm CAL} > 20$ GeV.

Events were required to have a reconstructed vertex with $-35 < z_{\rm vtx} < 33$ cm. This removed many events which were triggered from beam gas and halo muons. The reconstructed vertex was also required to have at least two good tracks leading to

[1]Good tracks in the offline selection were defined as tracks which possessed a transverse momentum such that $0.15 \leq p_T^{\rm trk} \leq 150$ GeV, a polarangle such that $15 \leq \theta_{\rm trk} \leq 164^\circ$, and were fit with at least 10 degrees of freedom.

it. This was required to reject non-*ep* background, and also because the vertex was used to compute other quantities like E_T and $\gamma_{\rm H}$. Before this could be applied, good tracking conditions were required, on which the vertex reconstruction relied.

As described in section 1.9, PHP events may have a large reconstructed $P_T^{\rm miss}$, and no isolated electron in the CAL. These events were largely removed by requiring $P_T^{\rm miss}/E_T > 0.5$.

Some NC DIS events occurred in overlap with a CAL PMT base discharges. The offending cell would then carry a significant fraction of the total E_T of the event. Requiring $E_T^{\rm max}/E_T < 0.7$ removed these events, where $E_T^{\rm max}$ is the E_T of the CAL cell with the largest E_T.

Some NC DIS events occurred in overlap with a halo or cosmic muon. These events left a large amount of energy in the BHAC, $E_{\rm BHAC}$, relative to other parts of the CAL. Energies in the inner and outer hadronic parts of the BHAC are labled as $E_{\rm BHAC1}$ and $E_{\rm BHAC2}$, respectively. These events were removed by rejecting events if either of the following were satisfied:

- $E_{\rm BCAL} > 8$ GeV and $E_{\rm BHAC1}/E_{\rm BCAL} > 0.85$
- $E_{\rm BCAL} > 2$ GeV and $E_{\rm BHAC2}/E_{\rm BCAL} > 0.5$

Some cosmic muons traversed the ZEUS detector with a very small distance of closest approach to the nominal interaction point. These types of events appear as two hadronic jets with two nearly anti-parallel tracks. These events were removed by rejecting all events with only two "good" tracks, such that the cosine of their angle was less than -0.996.

Some NC DIS events were reconstructed with large P_T^{miss}. The were removed from the sample by identifying an isolated electron in the CAL. As described in section 4.3, candidate electrons were identified by the SINISTRA program. Only the highest probability candidate was considered. Important quantities for candidate included

- E'_e, the sum energy of CAL cells associated with the candidate.
- θ_e, the polar angle of the candidate cluster
- $\mathcal{I}_e$, the *isolation* of the electron from other CAL deposits; computed as $\mathcal{I}_e = \overline{E'}_{e,7}/E'_e$, where $\overline{E'}_{e,7}$ is the energy sum of the cells belonging to the candidate which are outside a cone of radius .7 from the center of the candidate deposit in the $\eta - \phi$ plane.
- $\mathcal{N}_e$, the *narrowness* of the electron from other CAL deposits; computed as $\mathcal{I}_e = E'_{e,3}/E'_e$, where $E'_{e,3}$ is the energy sum of the cells belonging to the candidate within a cone of radius .3 in the $\eta - \phi$ plane.

Events were rejected if the following conditions were all satisfied.

1. $E'_e \geq 10$ GeV
2. $20 \leq \theta_e \leq 140$
3. $\mathcal{I}_e \leq .1$
4. $\mathcal{N}_e \geq .9$

Events were also rejected if the electron candidate satisfied ($y_{\rm e} < 0.7$), where $y_{\rm e}$ is the inelasticity of the event computed from the electron candidate information as $y_{\rm e} = 1 - \frac{E'_e}{2E_e}(1 - \cos(\theta_e))$, where E_e is the nominal HERA II electron beam energy of 27.5 GeV.

Electrons from NC DIS occasionally deposited their energy in a wide shower, which could be falsely reconstructed as a jet. Events were rejected if any jet in the event overlapped with the electron candidate. Events were rejected if all the following were satisfied:

- $E'_e > 10$ GeV
- The distance in the $\eta - \phi$ plane between the jet and electron candidate was less than 0.1
- $|1 - E'_e/E_{\rm jet}| < 0.2$

Here, $E_{\rm jet}$ refers to the uncorrected CAL cell energy of the jet in question.

Even after these cleaning cuts, approximately 1% of the event was comprised by halo and cosmic muon events. These have a topology which is simple to identify by sight, but difficult to reliably quantify. The sample was independently visually scanned by two analyzers, and the remaining events were removed from the sample. There was no discrepancy between the events chosen for removal. No MC events were removed in this manner.

6.3.3 Kinematic and Jet Selection

All detector level events were required to have a dead-material-corrected Q^2 value greater than 200 GeV, and a corrected y less than 0.9. The procedure for

inactive-material correction is described in section 7.2.1.

All k_T cluster objects were required to have uncorrected $E_T^{\rm jet} > 3$ GeV before being considered jets to ensure reliable reconstruction. All jet variables will henceforth refer solely to those corrected for detector effects unless otherwise stated. Clustered objects were only considered jets if they satisfied $-1 < \eta^{\rm jet} < 2.5$. Thus, the terms *jet with highest* E_T^{jet}, *most forward jet* etc. implicitly refer to jets selected exclusively from the set of all jets within this $\eta^{\rm jet}$ range. All data events events in the sample were required to have the jet with highest $E_T^{\rm jet}$ satisfy $E_T^{\rm jet} > 14$ GeV. Inclusive jets were defined as any jet with $E_T^{\rm jet} > 14$ GeV. Dijet systems were defined as the two jets in an event with highest $E_T^{\rm jet}$, such that they possessed $E_T^{\rm jet1} > 14$ GeV and $E_T^{\rm jet2} > 5$ GeV, where $E_T^{\rm jet1} \geq E_T^{\rm jet2}$. 3-jet systems were defined as the three jets in an event with highest $E_T^{\rm jet}$, such that $E_T^{\rm jet1} > 14$ GeV, $E_T^{\rm jet2} > 5$ GeV and $E_T^{\rm jet3} > 5$ GeV, where $E_T^{\rm jet1} \geq E_T^{\rm jet2} \geq E_T^{\rm jet3}$.

The minimum value of $E_T^{\rm jet1}$ and inclusive-jet $E_T^{\rm jet}$ was chosen because this value is correlated with $P_T^{\rm miss}$, and the selection cut of $P_T^{\rm miss} > 11$ GeV limits selection efficiency below $E_T^{\rm jet1}$ of approximately 14 GeV. It was possible to choose the value of minimum $E_T^{\rm jet}$ for $E_T^{\rm jet2}$ and $E_T^{\rm jet3}$ because these jets were not strongly correlated with the selection of the event. The fundamental limitation for these jets was the reliable reconstruction of calorimeter quantities. The restriction on $\eta^{\rm jet}$ requires that jet be reconstructed well within the acceptance of the CAL.

6.4 Reconstruction and Selection of Simulated Events

To produce detector level and corrected detector level distributions for MC events, all selection criteria were performed identically as for the data, with exceptions

noted in section 6.3.2 and 6.3.3.

Parton- and hadron-level simulated events were only selected if $Q^2_{\rm gen} > 200$ GeV and $y_{\rm gen} < 0.9$, where $Q^2_{\rm gen}$, $y_{\rm gen}$ are understood to be the generated values, not the values from the QED born level.

Parton- and hadron-level jets were found in the lab frame by applying the k_T cluster algorithm to partons and hadrons, as described in chapter 4.5. Hadronic (partonic) jets were selected with the same phase space requirements as the corrected detector level jets, as described in section 6.3.3.

Chapter 7

Analysis Method

7.1 Comparison of MC and Data

In order to measure the cross sections in a manner independent of the specific characteristics of the detector, the data were corrected to the hadron level using leading-order MC. Before this was done, it was ensured that the detector-level distributions for the most important observables matched well between data and MC. The agreement was examined both within the phase space used for the analysis, and in regions slightly outside the selection cuts.

7.1.1 Reweighting Procedure

The generated distributions of z_{vtx} and Q^2 are input parameters to the MCs. The z_{vtx} distribution was determined from a selection of ZEUS NC events in the same data taking period, and the Q^2 distribution has been determined from several measurements. In order to improve the agreement between data and MC, these input distributions were effectively altered by filling MC histograms with weights differing slightly from 1, as functions of z_{vtx} and Q^2. MC events were assigned per-event weights

given by $w = w_z \times w_{Q^2} \times w_{track}$ for all detector-level quantities, and $w = w_z \times w_{Q^2}$ for all hadron- and parton-level quantities. The terms, w_z and w_{Q^2} refer to independent weights for the generated values of z_{vtx} and Q^2 respectively. The variable w_{track} refers to a weight which accounts for a tracking veto which was not included in the MC detector description at the time of generation. These factors are described in detail in Appendix B.

7.1.2 Detector-level Comparisons

In figures 7.1 (a)–(f), the comparison between data and ARIADNE 4.08 [48] kinematic distributions is shown for $e^- p$ inclusive jet samples. Equivalent comparisons for $e^+ p$ are included in appendix A. It can be observed that all presented quantities shown are in good agreement, both inside and outside of the selection criteria. In figures 7.2 and 7.3, detector-level jet quantities are shown. From 7.2(a), it can be observed that data events have significantly more jets per event than the MC, which is expected because higher order terms not included in the LO MC are responsible for multi-jet production. The shape of the $E_T^{\rm jet}$ and $\eta^{\rm jet}$ distributions for jets with highest, second- and third-highest $E_T^{\rm jet}$ are all in good agreement, however, so it is still acceptable to use the MC samples to correct event and jet variables.

7.2 Correction Procedures Applied to Data Events

7.2.1 Inactive Material Corrections

As particles left the interaction region, they passed through the MVD, HERA beampipe, and support materials before entering the active region of the CTD. Parti-

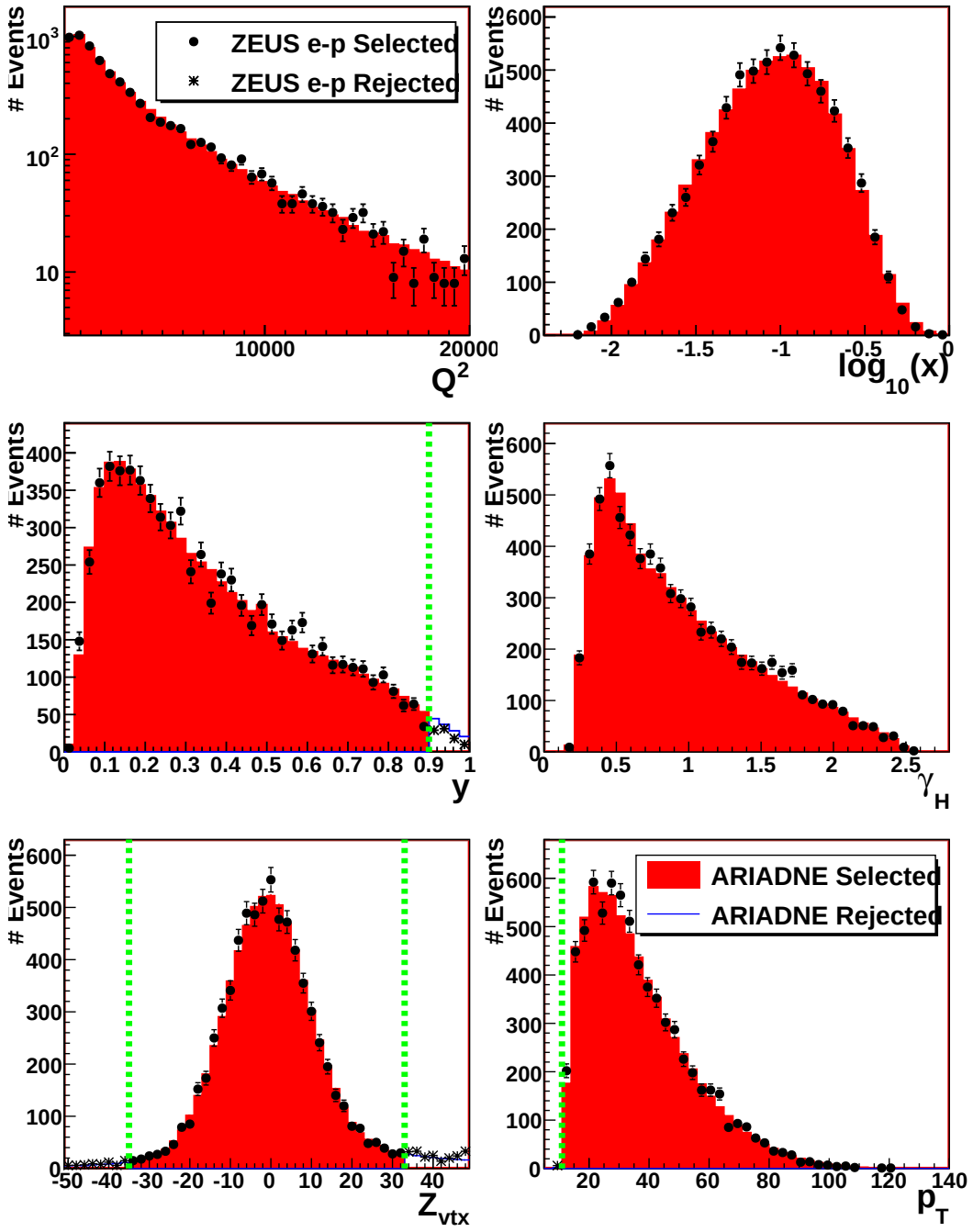

Figure 7.1: Comparison between detector level kinematic quantities of e^-p data and CC DIS ARIADNE. Filled histograms and closed points represent data and MC events which were selected for the inclusive-jet sample. Stars and empty histograms represent data and MC events which fall outside the kinematic selection, but were only rejected by the selection cut indicated by the dashed line. The selection cut on $Q^2 > 200$ is applied, but not shown. The MC has been area-normalized to the data for each plot shown.

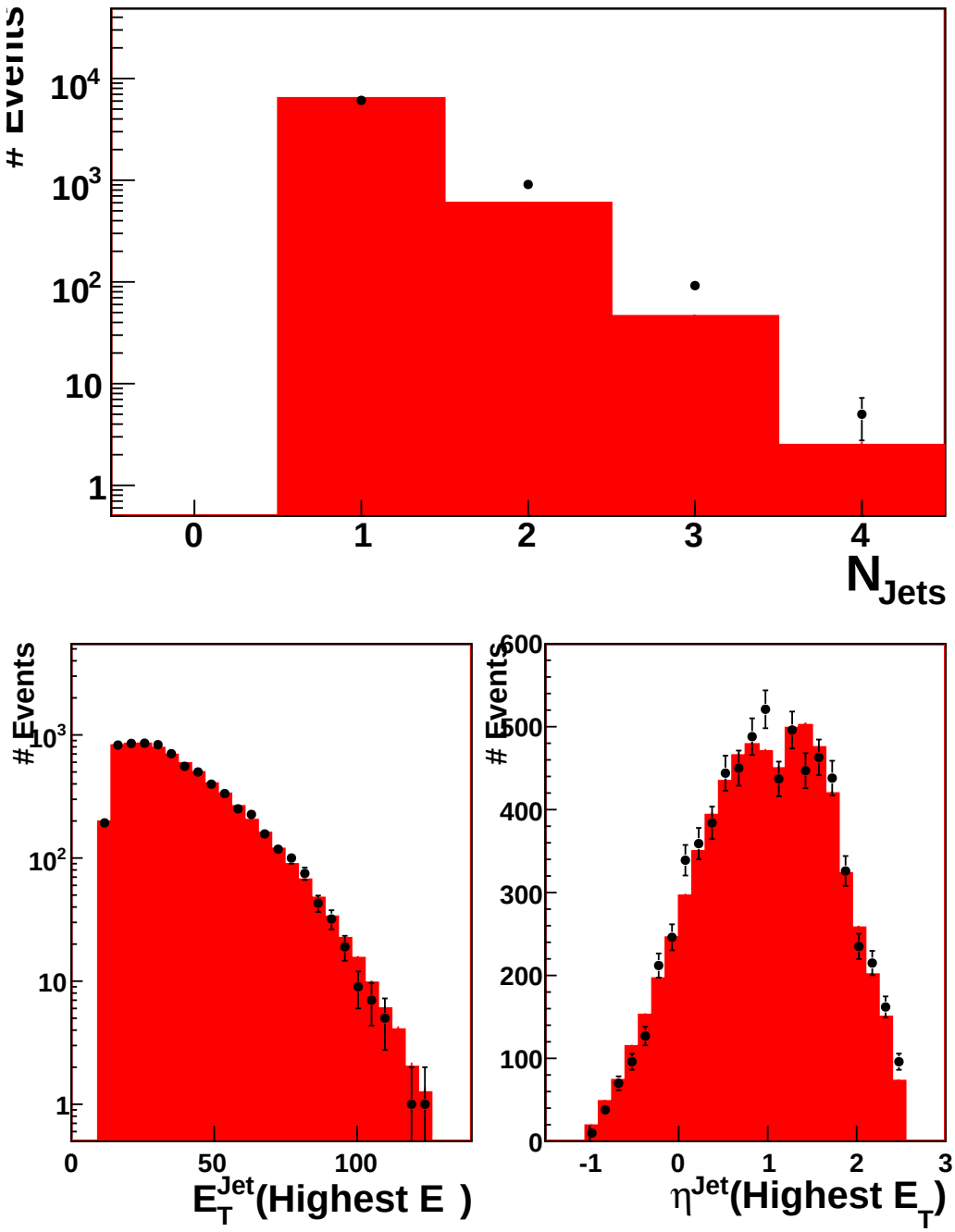

Figure 7.2: Comparison between detector level jet quantities of e^-p data and CC DIS ARIADNE. All events shown appear with all inclusive-jet selection cuts applied, but no correction to jet variables has been applied. Within these plots, a jet is defined as any k_T cluster object with $E_T^{\rm jet}$ greater than 5 GeV and $-1 < \eta^{\rm jet} < 2.5$.

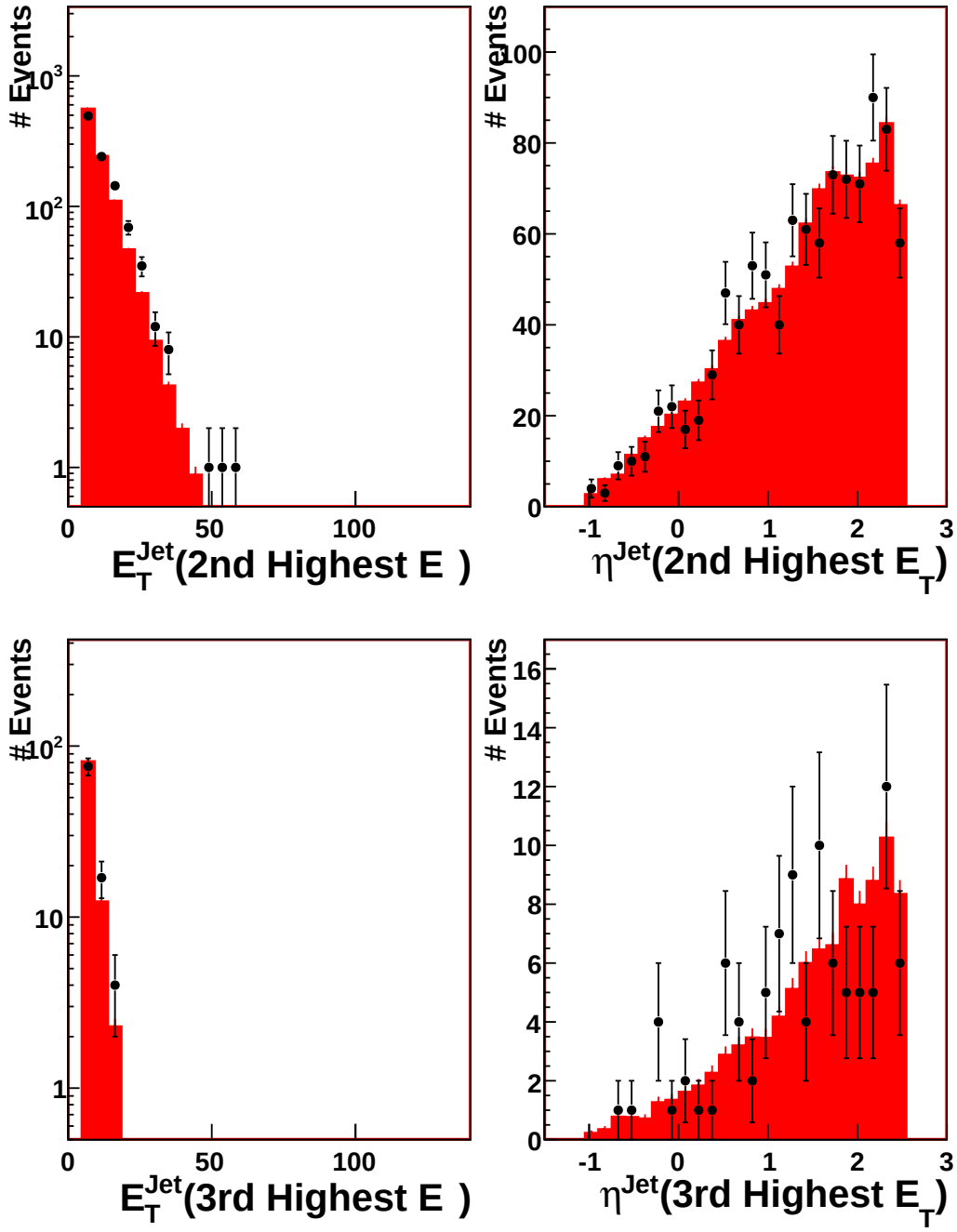

Figure 7.3: Comparison between detector level jet quantities of e^-p data and ARIADNE. All details as in figure 7.2.

cles then passed through the solenoid and more support structures before reaching the CAL. This means that particles would transfer some of their energy to materials without readout before being measured, and their immediately reconstructed quantities would not reflect the state shortly after the ep interaction. In order to estimate and correct these effects, samples of MC with detector simulation were generated, which are described in chapter 5. By comparing parton-level values of generated events and the reconstructed values from the detector simulation, estimations of energy loss or reconstruction bias were performed. Profile histograms were created for parton and reconstructed values in P_T^{miss}, and y, and the resultant values of these histograms showed the average reconstructed value for a certain generated value. Linear fits to these histograms then yielded correction factors. These corrections changed the reconstructed values on the order of 10%, and are presented in detail in appendix F.

These correction factors were then applied to data events, and MC events at the detector level to produce values which are referred to here as at the corrected-detector level, which means detector values corrected for dead material. These values were then used to produce distributions, which in turn were used to produce the cross sections presented in chapter 8. Correction factors were first applied to P_T^{miss} and y, and then these values were used as described in equation 4.5 to produce corrected values of Q^2 and x.

In figures 7.4 and 7.5, the bias and resolution of P_T^{miss} and y, respectively, are presented. MC samples presented here are from $e^- p$ ARIADNE samples described in section 5. The central line indicates the mean reconstructed values for each variable, before and after corrections were applied. Error bands indicate the 1-σ limits as taken

from Gaussian fits along the vertical axis.

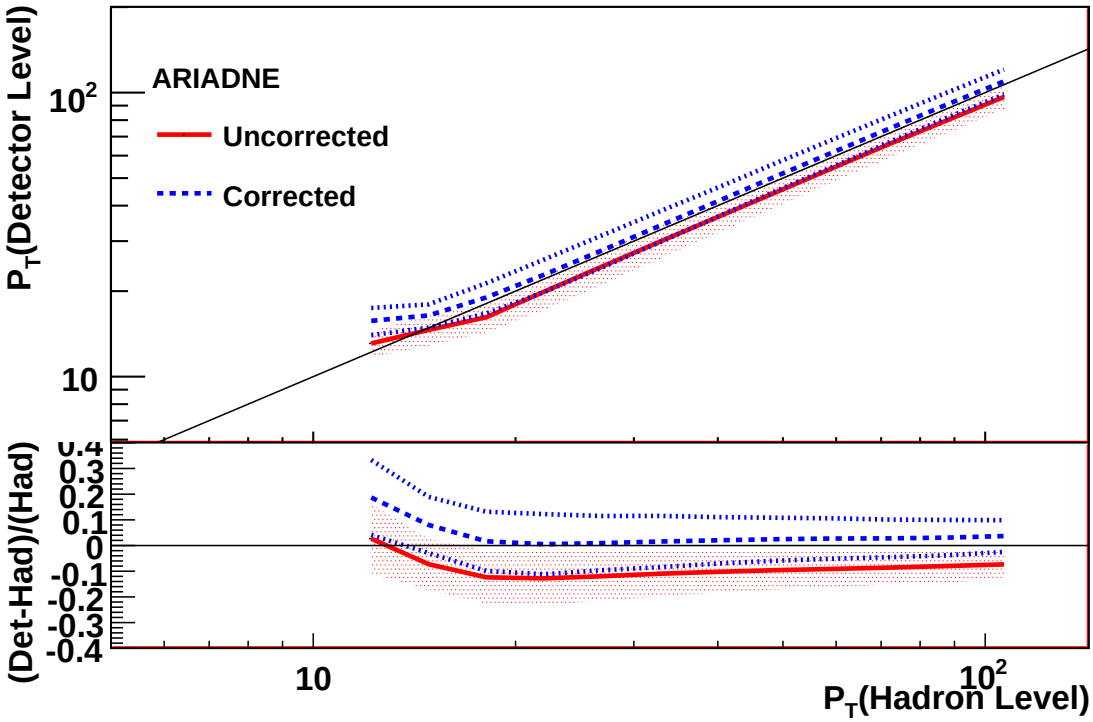

Figure 7.4: Comparison between hadron- and detector-level P_T^{miss} for $e^- p$ CC DIS ARIADNE. Central lines indicate the mean reconstructed value, while the outer lines and shaded regions indicate ± 1-standard-deviations obtained from a Gaussian fit in the reconstructed values for each value of generated P_T^{miss}.

From figure 7.4, it can be observed that P_T^{miss} was reconstructed before corrections on average approximately 10% below its hadron-level value, for $P_T^{\text{miss}} > 20$ GeV. For $P_T^{\text{miss}} < 20$ GeV, the reconstructed bias in P_T^{miss} decreases. The corrected value of P_T^{miss} was within a few percent for $P_T^{\text{miss}} > 20$, but is biased above the hadron-level value for $P_T^{\text{miss}} < 20$. The principle $P_T^{\text{miss}} > 11$ GeV cut was not applied during the production of this histogram, but the supplementary $P_T^{\text{miss}} > 20$ GeV cleaning cut for forward-jet events was retained.

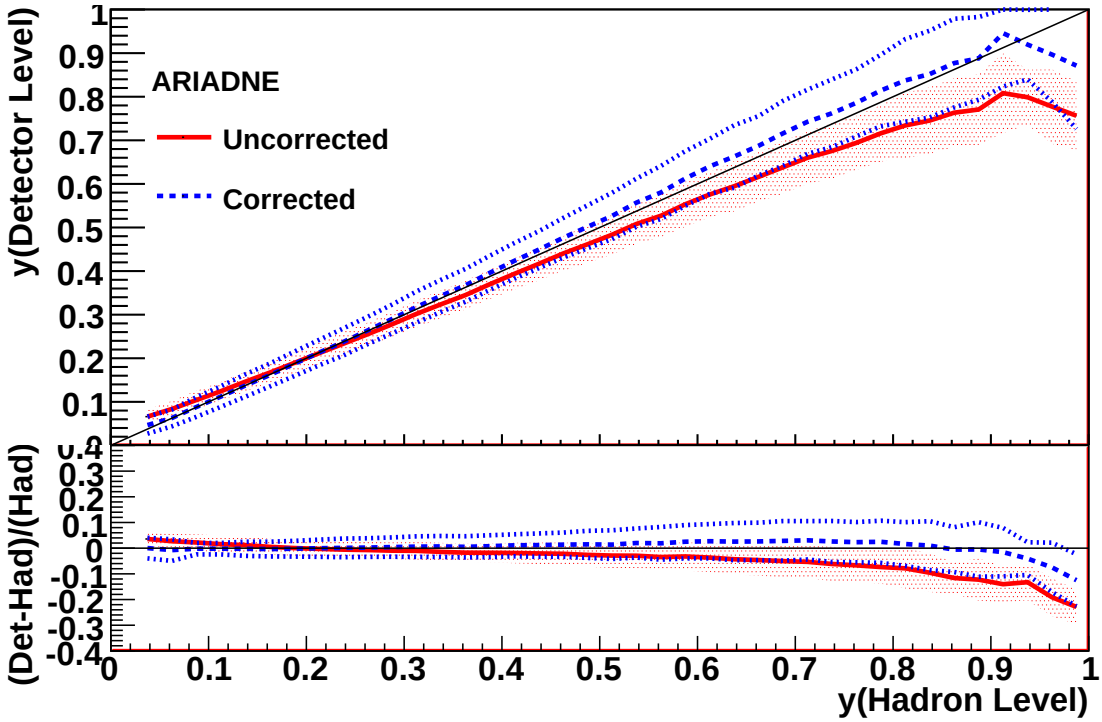

Figure 7.5: Comparison between generator- and detector-level y for $e^{-}p$ CC DIS ARIADNE. Central lines indicate the mean reconstructed value, while the outer lines and shaded regions indicate $\pm$1-standard-deviations obtained from a Gaussian fit in the reconstructed values for each value of generated y.

From figure 7.5, it can be observed that the relative difference between the mean reconstructed y and generated value as a function of the generated y was roughly linear, with negative slope. From the 1-standard deviation lines, it can also be seen that the resolution of y deteriorates with increasing y. After reconstruction, no systematic shift in y can be observed below y of .9, which is the boundary of the chosen phase space. No y cut was applied during the production of this histogram.

Figure 7.6 shows that the reconstructed values of Q^2 were systematically below their hadron-level values by approximately 20% before corrections were applied. Near

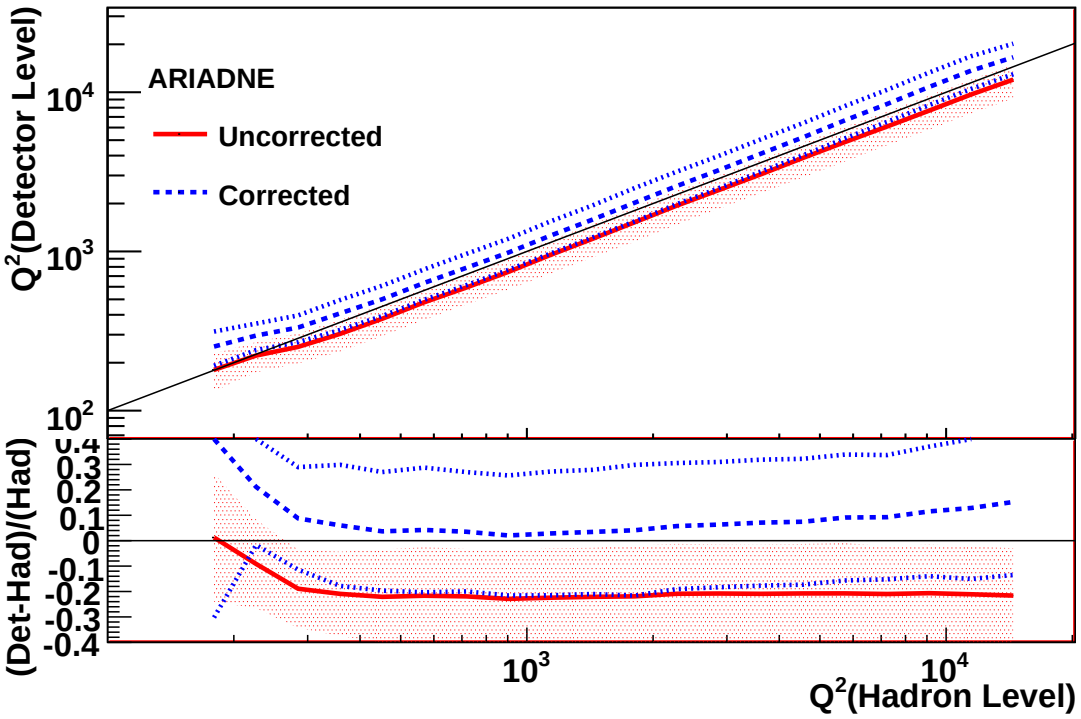

Figure 7.6: *Comparison between hadron- and detector-level Q^2 for e^-p CC DIS ARIADNE. Central lines indicate the mean reconstructed value, while the outer lines and shaded regions indicate ± 1-standard-deviations obtained from a Gaussian fit in the reconstructed values for each value of generated Q^2.*

a generated Q^2 value of approximately 200 GeV^2, events were reconstructed within a few percent of the proper value. After corrections the reconstructed Q^2 is within 10% of the generated value for events with generated $Q^2 > 300$. The relative difference between generated and reconstructed values is no longer constant however, with the mean reconstructed value above the generated. No Q^2 cut was applied during the production of this histogram.

Figure 7.7 shows the trend of reconstructed values of x, before and after corrections. It can be observed that before corrections, the reconstructed value was below

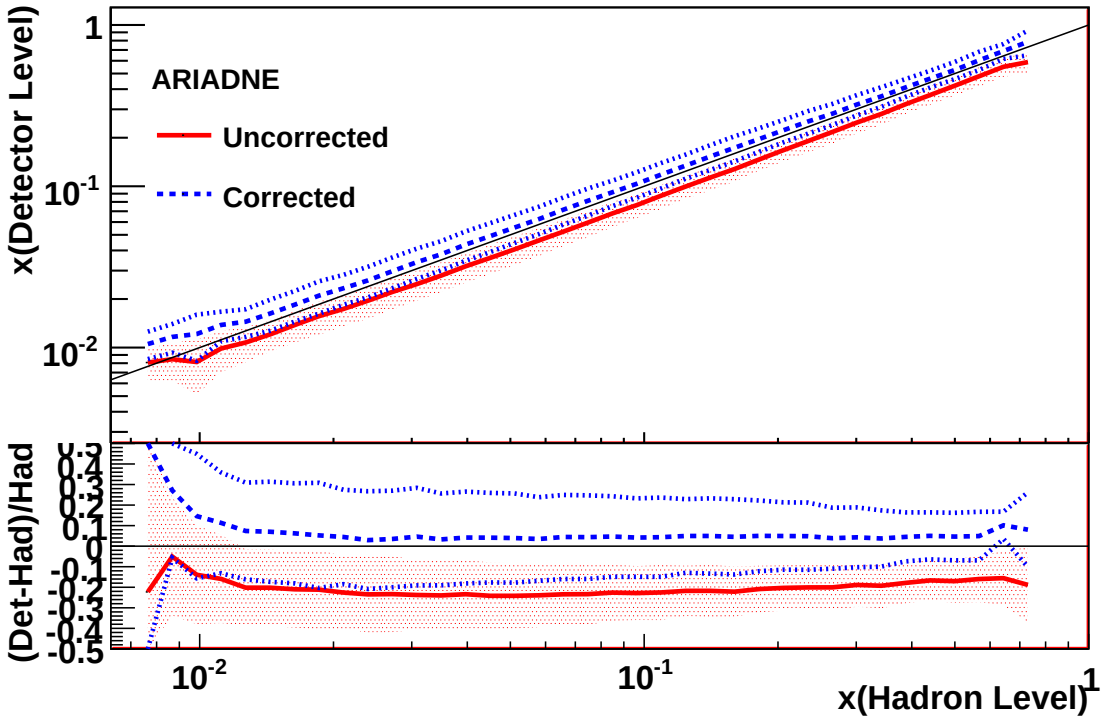

Figure 7.7: *Comparison between hadron- and detector-level x for e^-p CC DIS ARIADNE. Central lines indicate the mean reconstructed value, while the outer lines and shaded regions indicate ± 1-standard-deviations obtained from a Gaussian fit in the reconstructed values for each value of generated x.*

the hadron-level value by nearly 20% over the range (0.01, 0.2). After corrections, the reconstructed values were typically within a few percent of their generated values.

7.2.2 Jet Quantity Corrections

Figure 7.8 compares the reconstructed E_T^{jet} values for all jets with $E_T^{\text{jet}} > 3$ GeV to the hadron-level values for the same jets within the η^{jet} range $-1.5 < \eta^{\text{jet}} < 2.5$. No other jet cuts were applied. It can be seen from the figure that the average reconstructed value for E_T^{jet} is below the hadron-level value over the entire range of accessible values,and that the resolution suffers a notable degradation below approxi-

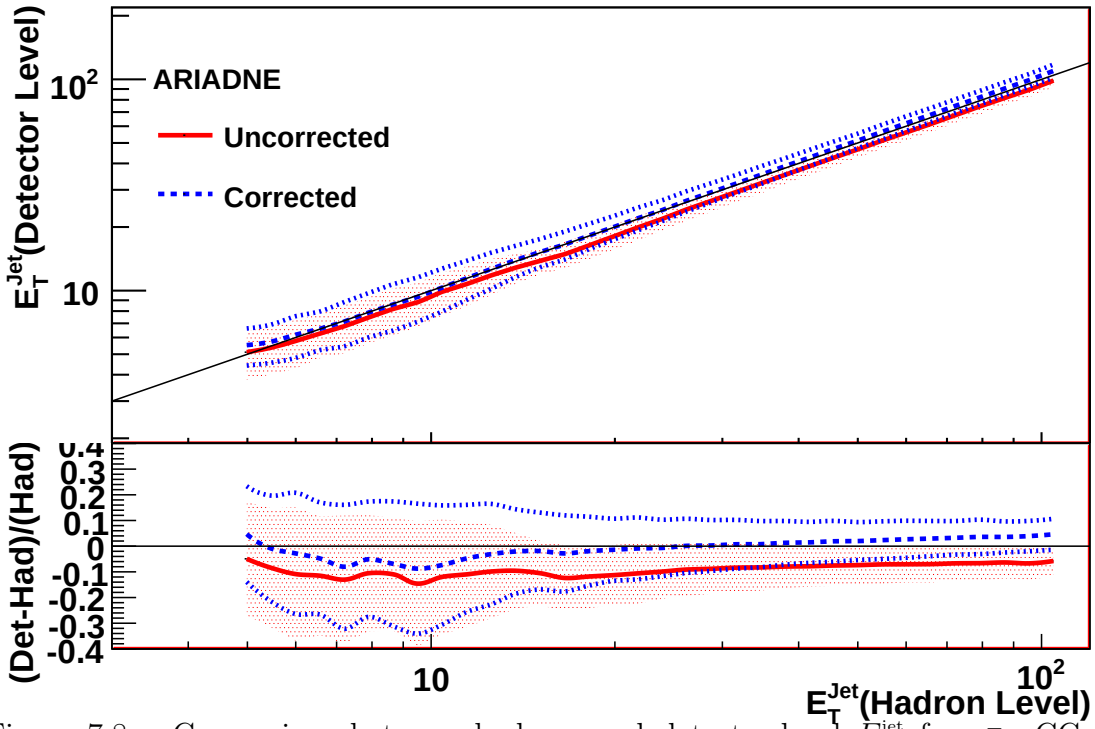

Figure 7.8: Comparison between hadron- and detector-level $E_T^{\rm jet}$ for e^-p CC DIS ARIADNE. Central lines indicate the mean reconstructed value, while the outer lines and shaded regions indicate ± 1-standard-deviations obtained from a Gaussian fit in the reconstructed values for each value of generated $E_T^{\rm jet}$.

mately 15 GeV. After corrections, the resolution remains unchanged, but the average value of reconstructed $E_T^{\rm jet}$ is much closer to the hadron-level value. The resolution for hadron-level jets is approximately 20% in the range $5 < E_T^{\rm jet} < 15\ GeV$, and approximately 10% for $E_T^{\rm jet} > 15$ GeV.

Figure 7.9 compares reconstructed $\eta^{\rm jet}$ values to hadron-level values of the same jets for all jets with $E_T^{\rm jet} > 3$ GeV. No other jet cuts were applied. It can be seen from the figure that the average reconstructed value for $\eta^{\rm jet}$ is in agreement with the hadron-level value over the entire range of accessible values, with the exception of jets with $\eta^{\rm jet} > 2.5$, which were not considered in the final sample. The resolution also suffers a notable degradation at $\eta^{\rm jet} > 2.5$. No corrections were applied to $\eta^{\rm jet}$ values.

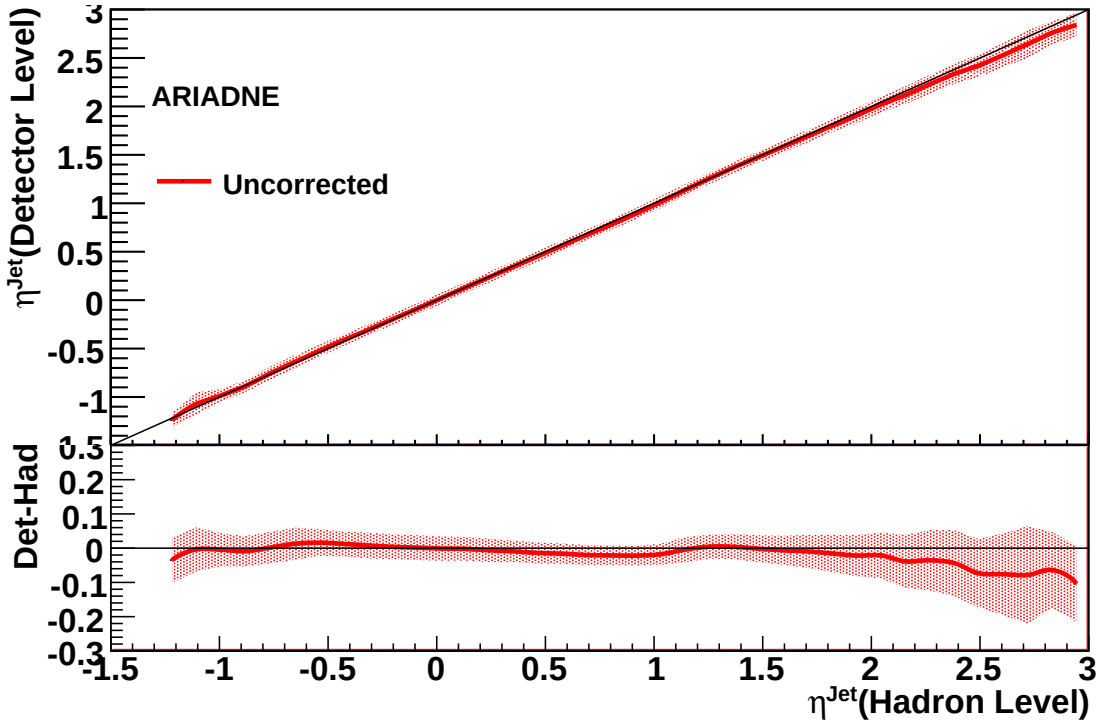

Figure 7.9: Comparison between hadron- and detector-level $\eta^{\rm jet}$ for e^-pCC DIS ARIADNE. Central lines indicate the mean reconstructed value, while the shaded region indicates $\pm$1-standard-deviations obtained from a Gaussian fit in the reconstructed values for each value of generated $\eta^{\rm jet}$.

Figure 7.10 compares reconstructed $\phi^{\rm jet}$ values to hadron level values for the same jets, for all jets with $E_T^{\rm jet} > 3$ GeV, $-1.5 < \eta^{\rm jet} < 2.5$. No other jet cuts were applied. It can be seen from the figure that the average reconstructed value for $\phi^{\rm jet}$ is in agreement with the hadron-level value, within one or two degrees, and that the resolution is on average within 5 degrees. No corrections were applied to $\phi^{\rm jet}$ values.

7.2.3 Transverse Energy Corrections

To understand the the uncertainty in the absolute energy scale of the jets, the differences between data and MC simulation in single-jet NC DIS events was studied [56]. Because the transverse energy of the single jets and electrons is expected to be equal in these events, the reconstructed transverse energy of the electron, $E_{T,\rm DA}$,

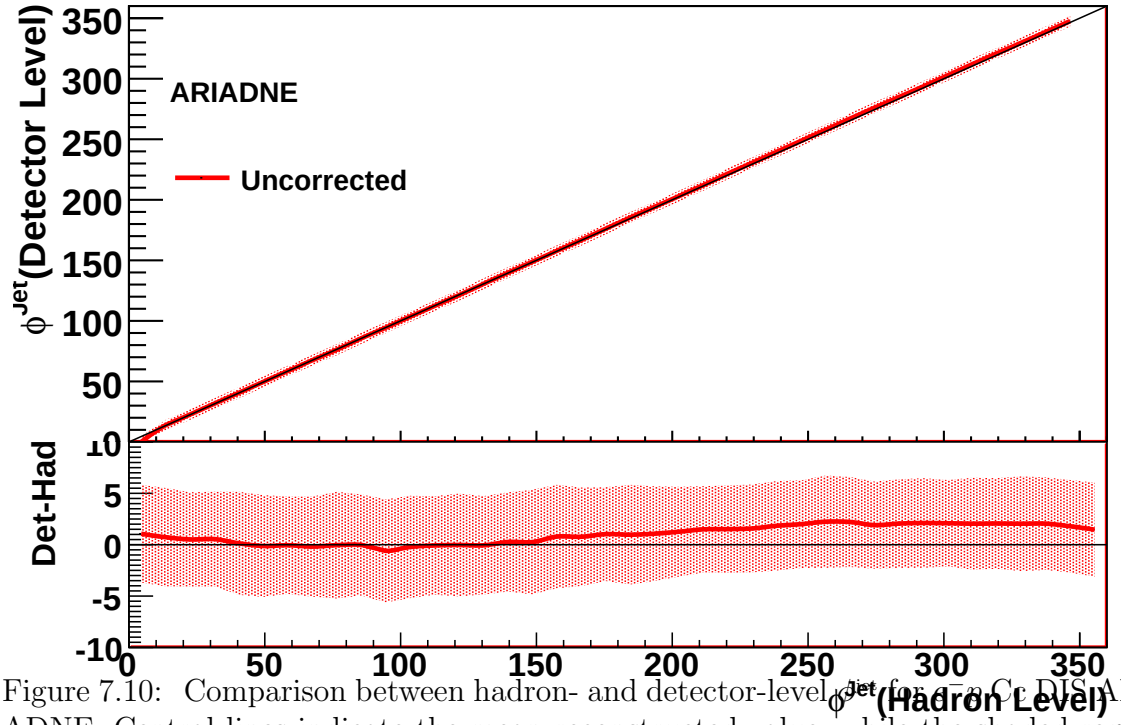

Figure 7.10: Comparison between hadron- and detector-level $\phi^{\rm jet}$ for e^-p CC DIS ARIADNE. Central lines indicate the mean reconstructed value, while the shaded region indicates ± 1-standard-deviations obtained from a Gaussian fit in the reconstructed values for each value of generated $\phi^{\rm jet}$.

provided an alternative means of estimating the transverse energy of the jets. The ratio of jet E_T to electron E_T, $R =< E_T^{\rm jet}/E_{T,\rm DA} >$ was therefore expected to be near one. The double ratio of data to MC, $R_{\rm DATA}/R_{\rm MC} - 1$, vs. $\eta^{\rm jet}$ is presented in figure 7.11 (a) before correction factors were applied. In figure 7.11 (b) the same ratio is plotted after correction factors were applied to the data, showing a far better agreement between data and MC. The same ratio as a function of the hadronic system angle, $\gamma_{\rm H}$ is presented in figures 7.12 and 7.12. These corrected ratios were then used to estimate the final uncertainty on the jet energy scale, as discussed in section 7.4. The correction factors are presented in detail in appendix F.

The same correction factors derived from $R_{\rm DATA}/R_{\rm MC}$ in the NC DIS sample

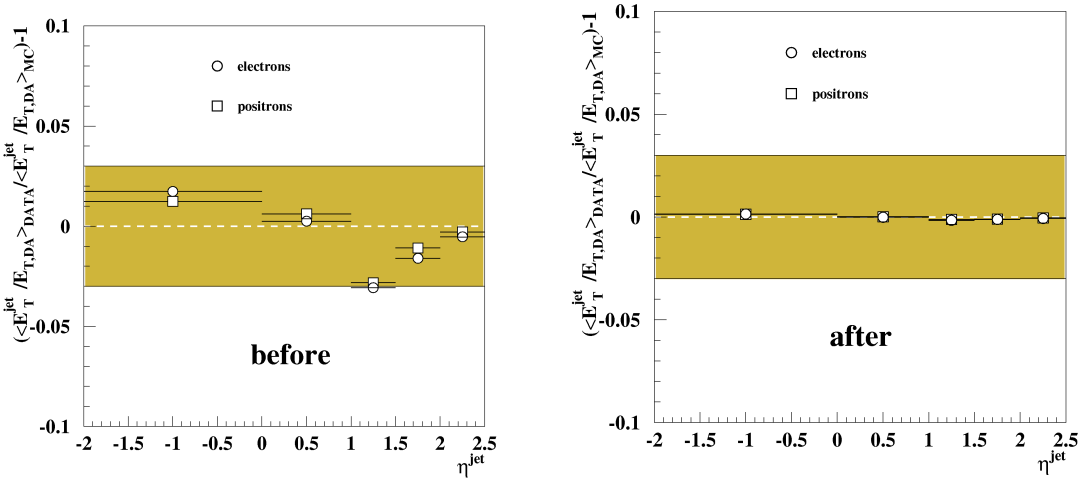

Figure 7.11: Jet transverse energy data-MC double ratios before and after corrections vs. η^{jet} for $e^{-}p$ CC DIS ARIADNE.

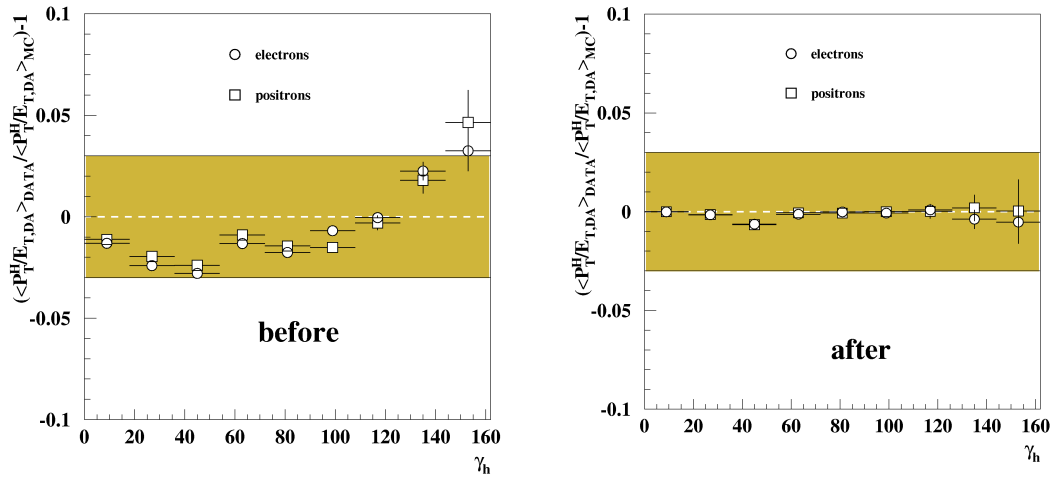

Figure 7.12: Jet transverse energy data-MC double ratios before and after corrections vs. γ_{H} for $e^{-}p$ CC DIS ARIADNE.

were applied to data in the CC DIS samples presented here.

7.3 Correction Procedures Applied to Theoretical Calculations

7.3.1 QED Corrections

Because the MEPJET program does not include QED radiative effects, correction factors were applied to the born-level partonic distributions. The correction factors are presented in the data tables located in appendix G. They were determined by generating samples of MC using the program HERACLES 4.6.1 [50] via DJANGO 1.3 [51], with and without QED radiating effects. The Fermi coupling constant was set to $G_F = 1.1664 \cdot 10^{-5}$ GeV^{-2} and the mass of the Z boson was set to $M_Z = 91.1876$ GeV. The resulting distributions reflected jets of partons including higher order effects in α_{EW}.

7.3.2 Hadronization Corrections

In order to correct the distributions from the fixed-order calculations to the full hadron level, correction factors were applied individually to each bin of each histogram. These correction factors were derived from the ratios between hadronic and partonic distributions in the MC samples described in chapter 5. ARIADNE samples were used to determine the SM predictions, and correction samples from the LEPTO 6.5 program [46] were used to estimate the systematic uncertainty due to the modelling of the QCD cascade. These correction factors are presented in the data tables located in appendix F. The final distributions reflected jets of hadrons including higher order

effects in both $\alpha_{\rm EW}$ and $\alpha_{\rm S}$.

7.4 Estimation of Experimental Systematic Uncertainties

The same NC DIS data and MC samples described in section 7.2.3 were used to estimate the uncertainty of the energy scale of the jets. In figure 7.13(a), the double ratio $R_{\rm DATA}/R_{\rm MC}$ is presented, where individual points correspond to events with jets from specific bins of $\eta^{\rm jet}$. The residual disagreement between data and MC in these regions gives an estimate of the absolute uncertainty in the reconstruction for jets in the CC sample. In figure 7.13(b), the double ratio $R_{\rm DATA}/R_{\rm MC}$, where $R = P_T^H/E_{T,DA}$, is shown. Here P_T^H is the transverse momentum of the hadronic system, and points representing events from specific bins of $\gamma_{\rm H}$. The residual deviation from 1 here represents an estimation of the absolute energy scale uncertainty of calorimetric quantites.

7.5 Estimation of Theoretical Systematic Uncertainties

As described in section 2.7, the uncertainty on the NLO QCD calculations due to terms beyond NLO was estimated by varying the renormalization scale, $\mu_{\rm R}$, between $Q/2$ and $2Q$. The resultant change on the cross sections was typically below $\pm 2\%$ for the inclusive-jet cross sections and below $\pm 5\%$ for the dijet cross sections. For the trijets, the$\mathcal{O}(\alpha_{\rm S}^2)$ calculations were only LO, and the resulting uncertainty on the cross sections was $\approx \pm 30\%$ for all bins. This uncertainty was far larger than all other theoretical uncertainties, so no other theoretical uncertainty source was taken into account for these cross sections. The uncertainty of the calculations due to the value of the factorization $\mu_{\rm F}$ was estimated by repeating the calculations with $\mu_{\rm F} = Q/2$ and

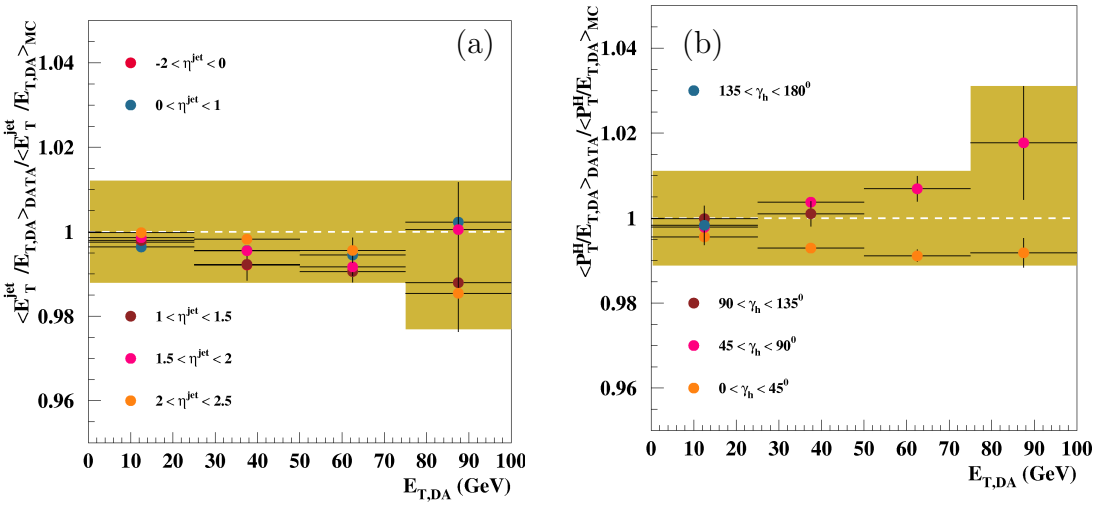

Figure 7.13: E_T reconstruction in bins of $\eta^{\rm jet}$ (a) and $\gamma_{\rm H}$ (b) vs. $E_{T,DA}$ for e^-p NC DIS ARIADNE, where $E_{T,DA}$ is the transverse energy of the isolated electron. The vertical axis represents the double ratio of ZEUS Data over MC for the quantites $E_T^{\rm jet}/E_{T,DA}$(a) and $P_T^H/E_{T,DA}$(b), were P_T^H is the transvese momentum of the entire hadronic system.

$2Q$. The effect was negligible.

The uncertainty on the NLO QCD calculations due to the uncertainty from the proton PDFs was estimated by repeating the calculations using the 22 additional sets from the ZEUS-S [24] PDF extraction, which takes into account the statistical and correlated systematic experimental uncertainties of each data set used in the determination of the proton PDFs. The resulting uncertainty in the inclusive-jet e^-p (e^+p) cross sections was below $\pm 2(4)\%$, except in the regions $E_T^{\rm jet} > 80$GeV , $Q^2 > 2 \times 10^4$ and $\log_{10}(x) > .5$ regions where it reached $\pm 4(10)\%$. The resulting uncertainty in the dijet e^-p (e^+p) cross sections was below $\pm 5(5)\%$, except in the region $\overline{E}_T^{\rm jet} > 50$GeV where it reached $\pm 7(15)\%$.

The uncertainty on the NLO QCD calculations due to the uncertainty from $\alpha_s(M_Z)$ was estimated by repeating the calculations using two additional sets of ZEUS-S proton PDFs, for which different values of $\alpha_s(M_Z)$ were assumed in the fits. The difference between the calculations using these various sets was scaled by a factor such as to reflect the uncertainty on the current world average of $\alpha_s(M_Z)$ [57]. The resulting uncertainty in the cross sections was below $\pm 1\%$.

The uncertainty from the modeling of the QCD cascade was estimated as the difference between the hadronization corrections obtained using MC samples generated by the ARIADNE and LEPTO programs. The resulting uncertainty on the inclusive-jet and dijet cross sections was typically below $\pm 1\%$.

Chapter 8

Results

In this chapter, hadron-level cross sections for jet production in CC DIS are presented. The cross sections represent an integrated luminosity of 180 pb^{-1} of e^-p data, and 179 pb^{-1} of e^+p data, using the ZEUS detector at the HERA collider. The cross sections are grouped into four categories, depending on the lepton longitudinal-polarization and jet topology considered; Inclusive-jet polarized, Inclusive-jet unpolarized, Dijet unpolarized and trijet unpolarized. The unpolarized cross sections represent extrapolations from polarized cross sections using the SM relation $\sigma_{\text{CC}}^{e^\pm p}(P) = (1 \pm P)\sigma_{\text{CC}}^{e^\pm p}(0)$, where P is the luminosity-averaged lepton longitudinal polarization. The inclusive jet measurements represent 5335 negatively-polarized e^-p jets, 870 negatively polarized e^+p jets, 2122 positively-polarized e^-p jets and 2284 positively polarized e^+p jets. The dijet samples represent 1117 e^-p and 464 e^+p events. These events form a subset of the inclusive jet sample. The trijet sample is a subset of the dijet sample, with 109 events for e^-p data and 30 for e^+p.

In all figures and tables, measured cross sections are compared to SM predictions provided by the MEPJET 2.1 [10] program. The calculations from MEPJET were corrected from the electroweak born-level to represent cross sections for jets of hadrons

with ISR/FSR via LO MC as described in section 7.3. All calculations were for unpolarized leptons, but polarized predictions were produced by scaling by a factor of $1/(1 \pm P)$ for $e^{\pm}p$ data. Numerical tables for all figures presented here are given in appendix G.

8.1 Inclusive Jet Polarized Differential Cross Sections

The inclusive-jet differential cross sections presented here represent samples of negatively- (positively-) polarized electron beams with an integrated luminosity of 106.4 (73.6) pb^{-1} and luminosity-weighted average polarization of $P_{e^-}^{\rm neg} = -0.27 \pm 0.01$ ($P_{e^-}^{\rm pos} = +0.29 \pm 0.01$) were analyzed. For positrons, the samples analyzed were of 76.5 and 102.1 pb^{-1} with a luminosity-weighted average polarization of $P_{e^+}^{\rm neg} = -0.37^{+0.01}_{-0.02}$ and $P_{e^+}^{\rm pos} = +0.32 \pm 0.01$, respectively.

The cross sections $\frac{d\sigma_{\rm jet}}{dE_T^{\rm jet}}$, for negatively- and positively-polarized e^-p (e^+p) collisions are shown in Fig. 8.1a (8.1b). Jets were defined as $E_T^{\rm jet} > 14$ GeV and $-1 < \eta^{\rm jet} < 2.5$. Jets with $E_T^{\rm jet}$ up to 120 GeV are accessible within present statistics. The figures also show the ratio of the cross sections for negatively- and positively-polarized lepton beams. This ratio is nearly constant within errors and in agreement with the measured polarization ratio, given by the luminosity averaged polarization during data taking as described in sections 6.1 and 6.3.1. This was $(1 - P_e^{\rm neg})/(1 - P_e^{\rm pos}) = 1.79 \pm 0.05$ for e^-p collisions and $(1 - P_e^{\rm neg})/(1 - P_e^{\rm pos}) = 2.10 + 0.08 - 0.14$ for e^+p collisions. The integrated polarized inclusive-jet cross sections, $\sigma_{\rm jets}$, are given in Table 8.1. The measured integrated cross sections are in good agreement with the predictions of the SM as given by the MEPJET calculations. The unpolarized inclusive-jet cross sections as functions of Q^2, $\eta^{\rm jet}$ and x show similar levels of agreement with the predictions,

and are included in appendix H.

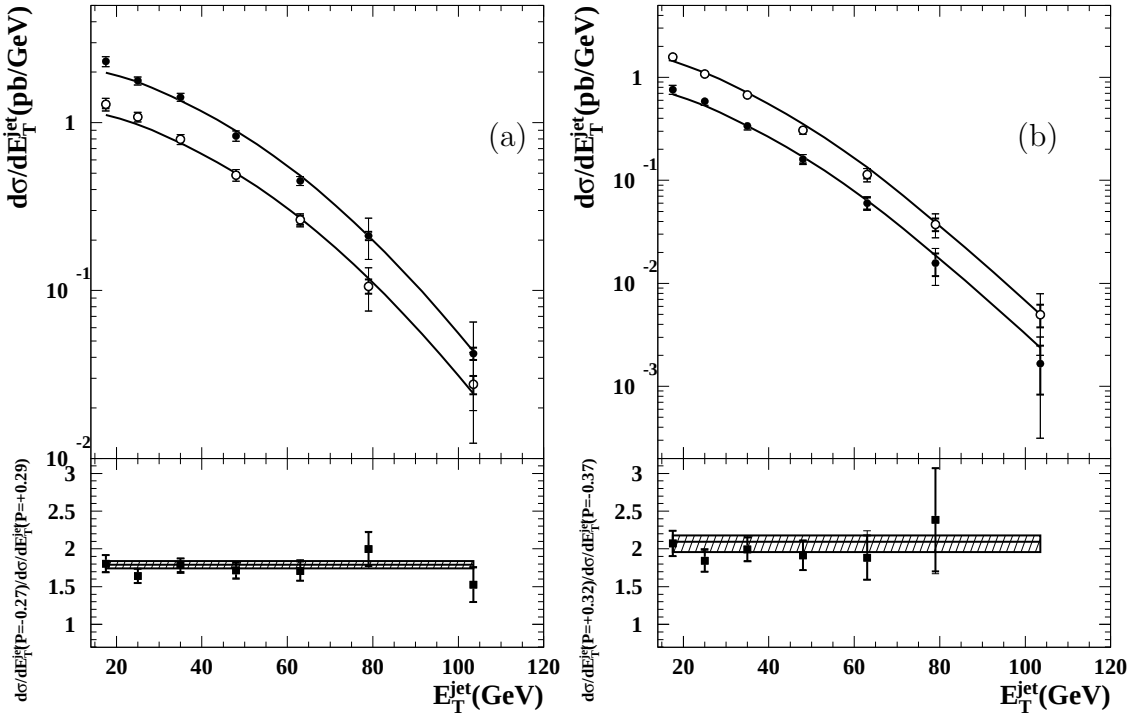

Figure 8.1: Polarized e^-p (a) and e^+p (b) inclusive-jet differential cross sections as a function of $E_T^{\rm jet}$. Cross sections for left-handed leptons are shown in filled circles, while right-handed are shown in open circles. The lower part of the figure (a) displays the ratio of left-handed to right-handed cross sections, and the lower part of (b) shows the ratio of right- to left-handed.

8.2 Inclusive Jet Unpolarized Differential Cross Sections

Figures 8.2a, 8.3a, 8.4a and 8.5a show the unpolarized inclusive-jet differential cross sections as functions of $\eta^{\rm jet}$, x, $E_T^{\rm jet}$ and Q^2 in CC $e^{\pm}p$ DIS. The measured cross sections represent the combination of data from left- and right-handed polarizations. These were extrapolated to unpolarized measurements by $\sigma_{\rm CC}^{e^{\pm}p}(P) = (1 \pm P)\sigma_{\rm CC}^{e^{\pm}p}(0)$, where P is the luminosity-averaged lepton polarization. Theoretical prediction curves

lepton / polarization	σ_{jets} (pb)	δ_{stat} (pb)	δ_{syst} (pb)	δ_{ES} (pb)	σ_{SM} (pb)
$P_{e^-} = -0.27 \pm 0.01$	70.54	0.97	0.58	$^{+0.43}_{-0.40}$	69.17
$P_{e^-} = +0.29 \pm 0.01$	40.53	0.88	0.45	$^{+0.24}_{-0.23}$	38.67
$P_{e^+} = -0.37^{+0.01}_{-0.02}$	17.55	0.60	0.57	± 0.11	16.86
$P_{e^+} = +0.32 \pm 0.01$	34.51	0.72	1.05	$^{+0.23}_{-0.22}$	35.33

Table 8.1: Integrated polarized inclusive-jet cross-sections σ_{jets} for jets of hadrons in the laboratory frame selected with the longitudinally invariant k_T cluster algorithm, described in section 4.5. The statistical, uncorrelated systematic and energy-scale (ES) uncertainties are shown separately. The uncertainty coming from the luminosity measurement is not listed. The predictions of the SM as given by the MEPJET calculations and are shown in the last column.

from MEPJET calculations using the ZEUS-S PDF sets [24] are also compared to the data. The relative difference to the NLO calculations and the ratios of e^-p cross sections to e^+p are presented in figures 8.2b, 8.3b, 8.4b and 8.5b.

The measured $\frac{d\sigma}{d\eta^{\text{jet}}}$, shown in Figure 8.2a, has a maximum at $\eta^{\text{jet}} \approx 1$, and is roughly similar in shape to $\frac{d\sigma}{dx}$, shown in Figure 8.3a. This similarity in shape is because the center-of-mass frame of the eq system is boosted in the electron direction relative to the lab system at low-x, and boosted in the proton direction at high-x. Thus, jets at low-x are likely to be scattered far in η from the proton remnant, and close to the remnant at high-x [58]. The values in x accessible by the data are within the range $0.013 < x < 0.63$. The MEPJET predictions give a reasonable description of the shape and normalization of the data. The measured ratio as a function of x, shown in Figure 8.3b, increases as a function of x, because of the increased contribution of u-PDF relative to the d-PDF at high-x. The measured ratio as a function of η^{jet} is

approximately 2 across the entire range, which is expected since the integral of valence u and d quarks densities are 2 and 1 respectively [59]. The ratio slightly increases as a function of η^{jet}, due to its kinematic relationship with x.

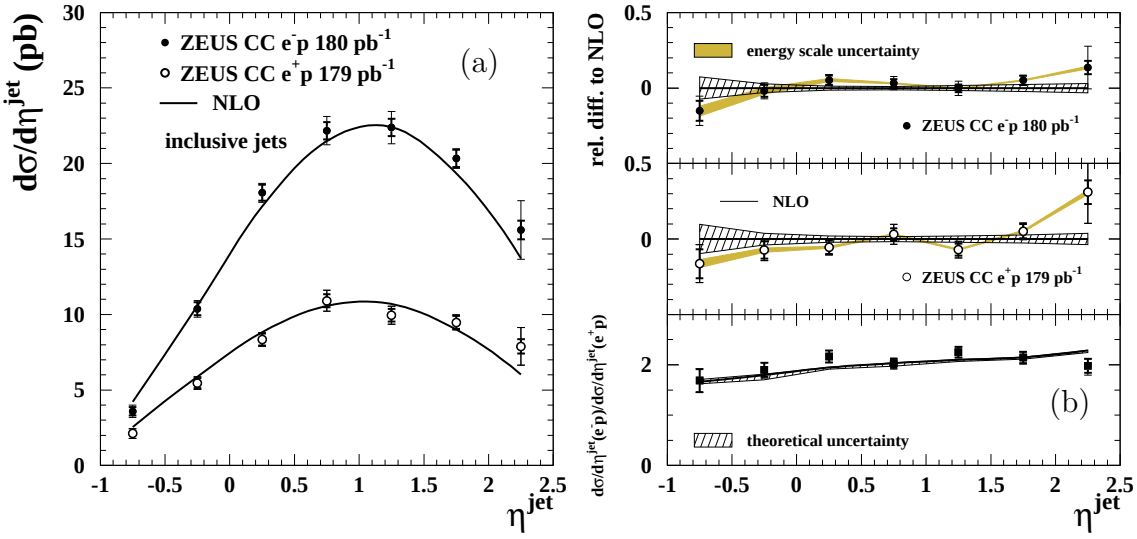

Figure 8.2: Unpolarized e^-p (filled circles) and e^+p (empty circles) Inclusive-Jet Differential Cross sections as a function of η^{jet} are displayed in (a). Relative differences to NLO pQCD calculations and ratios of $e^{\pm}p$ cross sections are shown in (b).

The measured $\frac{d\sigma}{dE_T^{\text{jet}}}$ exhibits a fall-off of two (three) orders of magnitude in the e^-p (e^+p) sample, which is similar to the behavior observed by the ZEUS and H1 collaborations in previous CC DIS jet production publications [60, 55]. Values of E_T^{jet} on the order of 120 GeV are accessible with the present statistics. For $200 < Q^2 < 2000$ GeV^2, the distributions display a weak dependence on Q^2. The cross sections as functions of E_T^{jet} and Q^2 show a less rapid fall-off below values of $E_T^{\text{jet}} \sim M_W$ and $Q^2 \sim M_W^2$ than what is observed in NC DIS processes due to the massive W propagator [61]. Similar shapes were observed in previous inclusive CC DIS [54, 62, 63] publications by the ZEUS and H1 collaborations. The cross sections with respect to

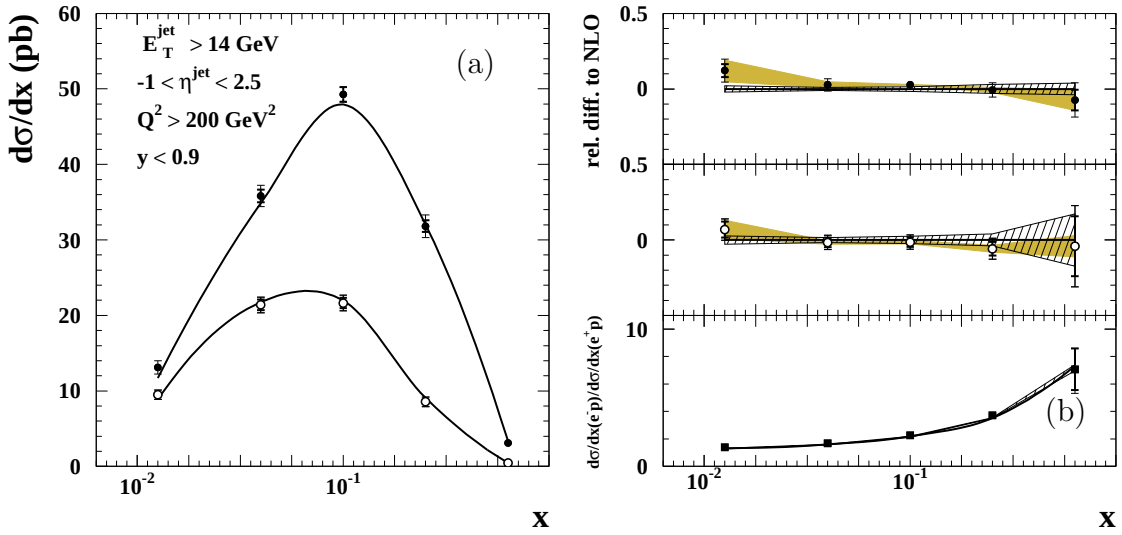

Figure 8.3: Unpolarized e^-p and e^+p x Inclusive-Jet Cross sections

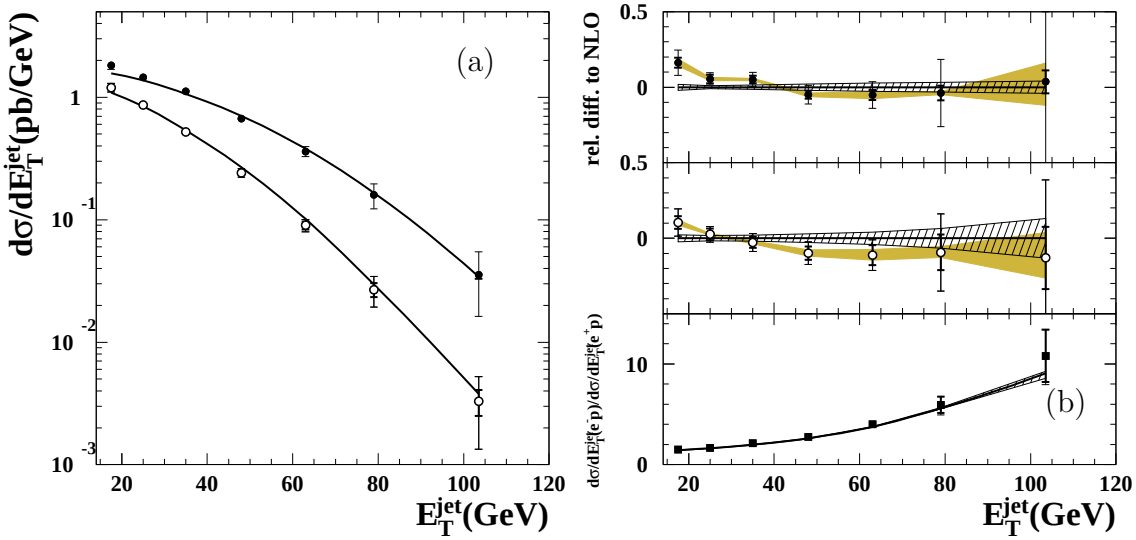

Figure 8.4: Unpolarized e^-p and e^+p $E_T^{\rm jet}$ Inclusive-Jet Cross sections

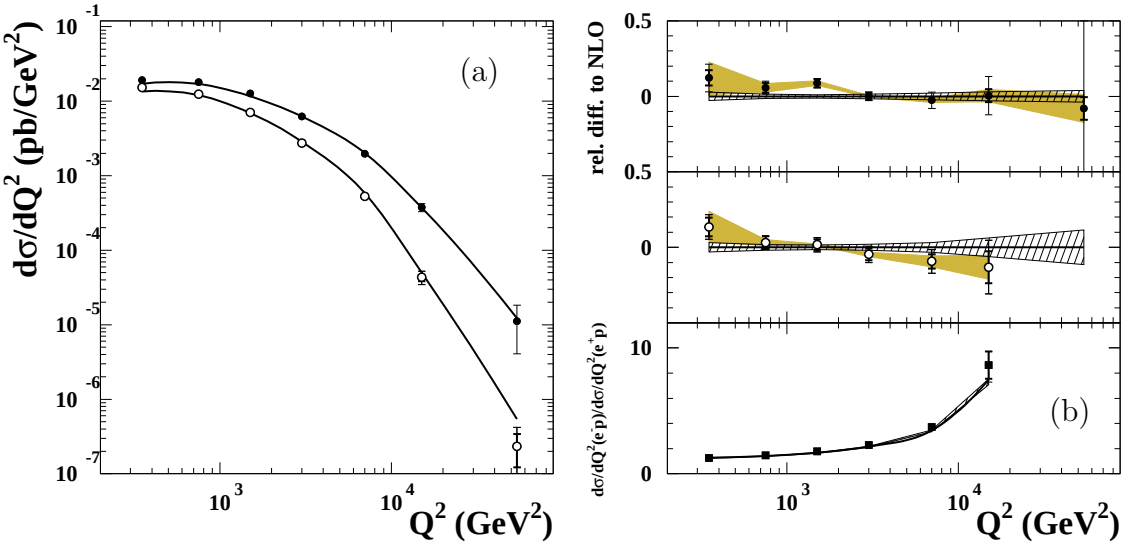

Figure 8.5: Unpolarized e^-p and e^+p Q^2 Inclusive-Jet Cross sections

Q^2 (E_T^{jet}) shows a slightly different shape than the predictions, with the data above the predictions at low Q^2 (E_T^{jet}), and the data below the predictions at high Q^2 (E_T^{jet}). This was also observed in the previous e^+p ZEUS CC DIS jet production measurement [55]. However, the measured ratios of e^-p to e^+p are in very good agreement with the predictions.

The measured cross sections for the e^+p sample decrease more rapidly as a function of E_T^{jet} and Q^2 than for the e^-p sample, which is visible in the ratios presented in Figures 8.4b and 8.5b. The increase of e^-p relative to e^+p at high values is expected due to the increasing contribution from the valence-quark densities in the proton at high x [64]. The observed ratios of the measured cross sections as a function of Q^2 is similar to the ratio of u and d parton densities, showing increase as a function of Q^2, a rise of the ration of the cross sections as a function of x is also observed, but to a lesser degree.

Figures 8.6a-d show the estimates of theoretical uncertainty from the terms be-

yond NLO, the parton-shower model and the uncertainty in the PDFs, separately for e^-p and e^+p collisions. The methods used to produce these estimates are described in section 2.9. Calculations using the PDF sets CTEQ6 [18, 19, 20] and MRST2001 [21] are also shown. These PDF sets are widely used in high energy physics, and include data from HERA, the Tevatron, and fixed target experiments. With the exception of $\frac{d\sigma_{\rm jets}}{d\eta^{\rm jet}}$ in the range $-1 < \eta^{\rm jet} < 0$, the uncertainty coming from the PDFs is dominant for all inclusive-jet $e^{\pm}p$ CC cross sections. At high $E_T^{\rm jet}$, Q^2 and x, the uncertainty in the predicted cross sections for positron beams is larger than for electron beams. This difference in the uncertainty due to the PDFs in the calculations for e^- and e^+ beams can be attributed to the different flavor content probed: in e^-p (e^+p) at high x the W^- (W^+) will couple predominantly to the u (d) valence quark in the proton; at present, the uncertainty in the d parton density is larger than that for the u quark [64]. The predictions derived from the alternative PDF sets shows a wide spread in the predictions, especially for positron beams. These measurements, in a phase-space region where the other theoretical uncertainties are well under control, have the potential to constrain the flavor content of the proton if used together with other data in PDF extractions. A fast and accurate method to perform fits to extract the proton PDFs on data sets that included jet cross sections in NC DIS and photoproduction was recently developed by the ZEUS Collaboration [22]; the result was a sizable reduction of the uncertainty on the gluon density for $x \gtrsim 10^{-2}$. Using the data presented here and extending such a method to jet cross sections in CC DIS may help to constrain the u and d valence quark distributions at high x. The integrated unpolarized inclusive-jet cross sections, σ-jets , are shown in Table 8.2. The measured

cross sections are in good agreement with the MEPJET predictions, also shown in the table using the alternative PDF sets.

lepton/ jet multiplicity	σ_{jets} (pb)	δ_{stat} (pb)	δ_{syst} (pb)	δ_{ES} (pb)	QCD predictions (pb)		
					ZEUS-S	CTEQ6	MRST
e^-/inclusive jet	56.18	0.68	0.53	$^{+0.34}_{-0.32}$	54.47 ± 0.75	54.05	54.56
e^+/inclusive jet	26.88	0.51	0.82	$^{+0.18}_{-0.17}$	26.77 ± 0.45	25.85	26.49
e^-/dijet	10.87	0.34	0.80	$^{+0.24}_{-0.23}$	9.14 ± 0.35	9.05	9.26
e^+/dijet	5.83	0.29	0.45	$^{+0.13}_{-0.12}$	4.57 ± 0.19	4.38	4.55
e^-/three jet	1.52	0.15	0.09	± 0.06	0.79 ± 0.22	0.79	0.82
e^+/three jet	0.563	0.110	0.037	$^{+0.025}_{-0.022}$	0.397 ± 0.118	0.386	0.409

Table 8.2: Integrated unpolarized jet cross-sections σ_{jets} for jets of hadrons in the laboratory frame selected with the longitudinally invariant k_T cluster algorithm. The statistical, uncorrelated systematic and energy-scale (ES) uncertainties are shown separately. The predictions of QCD as given by the MEPJET calculations using the ZEUS-S PDFs are shown at NLO for the inclusive-jet and dijet cross sections and at LO for the three-jet cross sections, together with the total theoretical uncertainty. Also shown are the total cross sections predicted by QCD using the CTEQ6 or MRST PDF sets.

8.3 Dijet Unpolarized Differential Cross Sections

Unpolarized dijet differential cross sections were measured in the kinematic regime $Q^2 > 200$ GeV^2 and $y < 0.9$. The cross sections were determined for jets with $E_T^{\text{jet1}} > 14$ GeV, $E_T^{\text{jet2}} > 5$ GeV and $-1 < \eta^{\text{jet}} < 2.5$. Figures 8.7a, 8.8a, 8.9a and 8.10a show the unpolarized dijet differential cross sections as functions of $\overline{\eta}^{\text{jet}}$, $\overline{E}_T^{\text{jet}}$, Q^2 and the dijet invariant mass, m^{jj} , where $\overline{\eta}^{\text{jet}} = (\eta^{\text{jet1}} + \eta^{\text{jet2}})/2$ and $\overline{E}_T^{\text{jet}} = (E_T^{\text{jet1}} + E_T^{\text{jet2}})/2$ in CC $e^{\pm}p$ DIS. Both measured cross sections and NLO QCD predictions are presented.

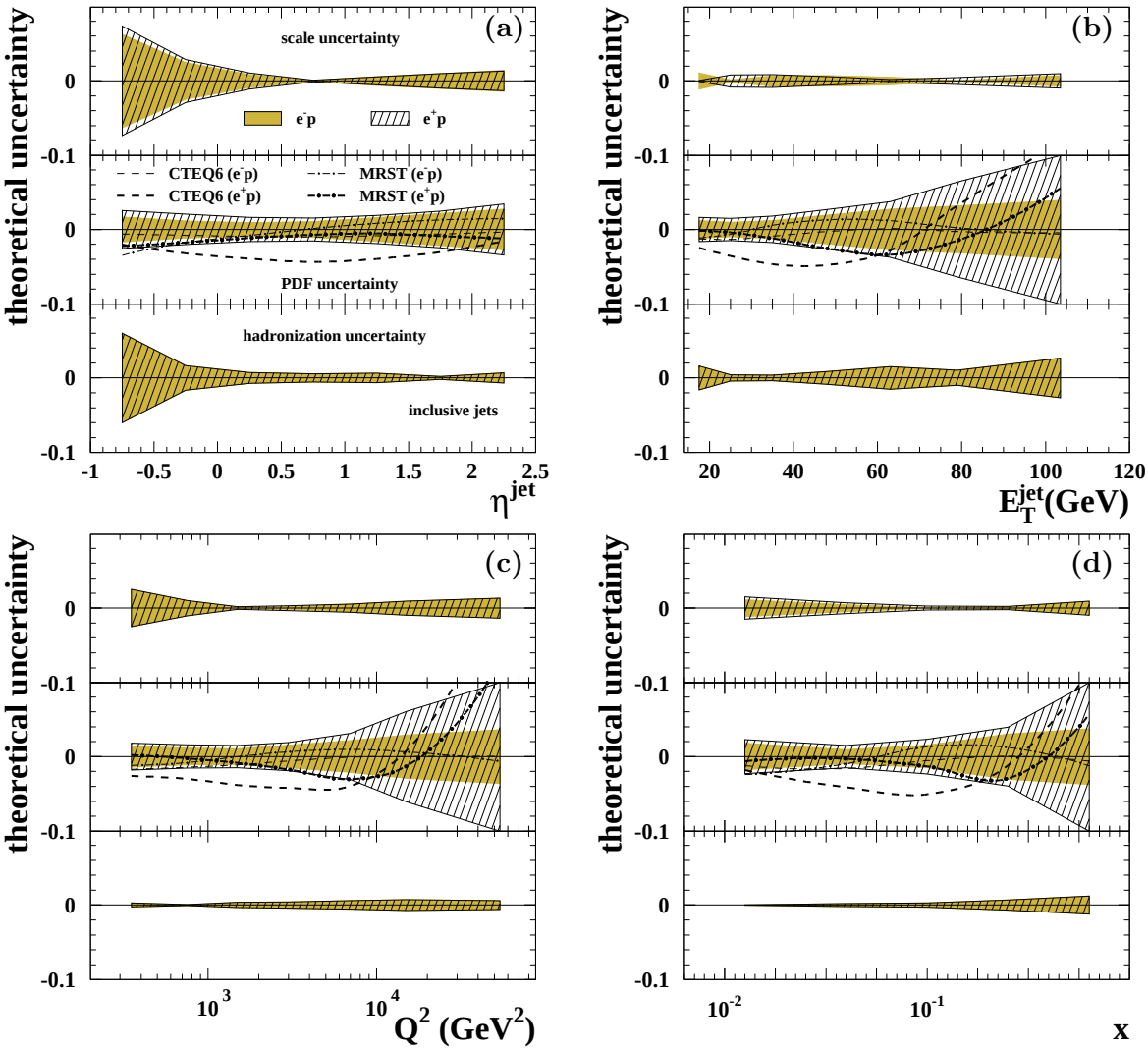

Figure 8.6: *Overview of theoretical uncertainties for the inclusive-jet cross sections in CC DIS for jets with* $E_T^{jet} > 14$ *GeV and* $-1 < \eta^{jet} < 2.5$ *in the kinematic regime given by* $Q^2 > 200$ GeV^2 *and* $y < 0.9$ *as functions of (a)* η^{jet}*, (b)* E_T^{jet}*, (c)* Q^2 *and (d)* x *in* e^-p *(shaded areas) and* e^+p *(hatched areas) collisions. Shown are the relative uncertainties induced by the variation of the renormalization scale* μ_R*, the uncertainties on the proton PDFs and hadronization model. Also shown are the relative differences between the NLO QCD calculations using the CTEQ6 (dashed lines) or MRST (dot-dashed lines) PDF sets to the calculations based on the ZEUS sets.*

Figures 8.7b, 8.8b, 8.9b and 8.10b show the relative differences of the measured and predicted cross sections, as well as the ratio of e^-p to e^-p cross sections.

The measured $\overline{\eta}^{\text{jet}}$ cross section has a maximum at $\overline{\eta}^{\text{jet}} \approx 1.25$. The measured cross section as a function of $\overline{E}_T^{\text{jet}}$ exhibits a fall-off of two orders of magnitude for $\overline{E}_T^{\text{jet}} \gtrsim$ 20 GeV. For $200 < Q^2 < 2000$ GeV^2, the distribution displays a weak dependence on Q^2 . Values of m^{jj} from 10 to 120 GeV are accessible with the present statistics. The MEPJET predictions are compared to the measured m^{jj} cross sections in Fig. 8.10a. Figure 8.10b shows the relative difference to the predictions. The MEPJET predictions do not give an adequate description in shape and normalization of the measured differential cross sections over the entire phase space. In particular, for m^{jj}, the data tend to be above the predictions for $m^{\text{jj}} \gtrsim 70$ GeV. The presented $\mathcal{O}(\alpha_{\text{s}}^2)$ calculations are NLO for dijet production, but higher order terms could contribute to the observed difference. This is partially implied by the integrated unpolarized dijet cross sections, shown in Table 8.2, in which a larger data cross section is observed than predicted by a factor of $\sim 19\%$ and $\sim 28\%$ for e^-p and e^+p data, respectively.

While the predictions show shape and normalization differences from the cross sections, they do provide a reasonable description of the ratios of the cross sections for e^-p and e^+p interactions. Dijet distributions include large contributions from boson-gluon-fusion (discussed in section 1.7), which is sensitive to the gluon PDF [22]. Understanding of the gluon PDF is critical to reducing the total uncertainty of measured cross sections at the Large Hadron Collider [64], because a large fraction of particle production is derived from gluons in the range $x \lesssim 10^{-2}$. In order to use the differential dijet cross sections presented here in global PDF fits, the ratios of e^-p to

e^-p cross sections present a means to attain sensitivity to the PDFs, while avoiding the discrepancies between the measured and predicted cross sections.

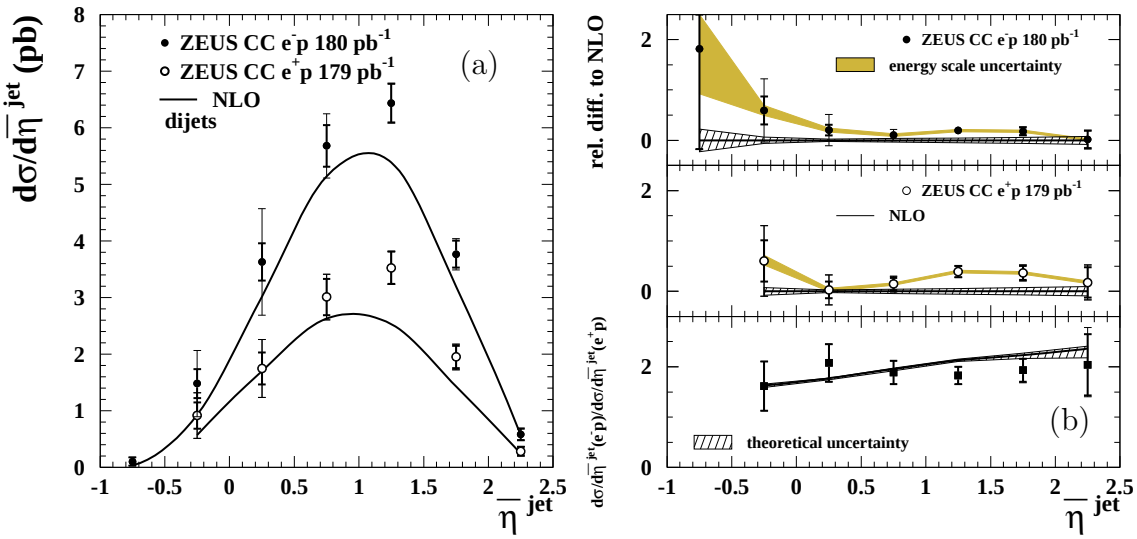

Figure 8.7: Unpolarized e^-p (filled circles) and e^+p (open circles) dijet differential cross sections as a function of $\overline{\eta}^{\rm jet}$ are shown in (a). The relative difference to NLO pQCD calculations are shown in the upper two portions of (b), while the ratio of e^-p and e^+p cross sections are shown in the bottom portion.

8.4 Trijet Unpolarized Differential Cross Sections

Three-jet cross sections are measured for the first time in CC DIS. The cross sections are measured in the kinematic regime $Q^2 > 200$ GeV^2 and $y < 0.9$, for jets with $E_T^{\rm jet1} > 14$ GeV, $E_T^{\rm jet2} > 5$ GeV, $E_T^{\rm jet3} > 5$ GeV and $-1 < \eta^{\rm jet} < 2.5$. Figure 8.11 shows a three-jet candidate event in the ZEUS detector: a distinct three-jet topology and large net transverse momentum are observed.

Figure 8.12a presents the differential cross sections as functions of the average rapidity of the three-jet system, $\overline{\eta}^{\rm jet}$, where $\overline{\eta}^{\rm jet} = (\eta^{\rm jet1} + \eta^{\rm jet2} + \eta^{\rm jet3})/3$. The currently

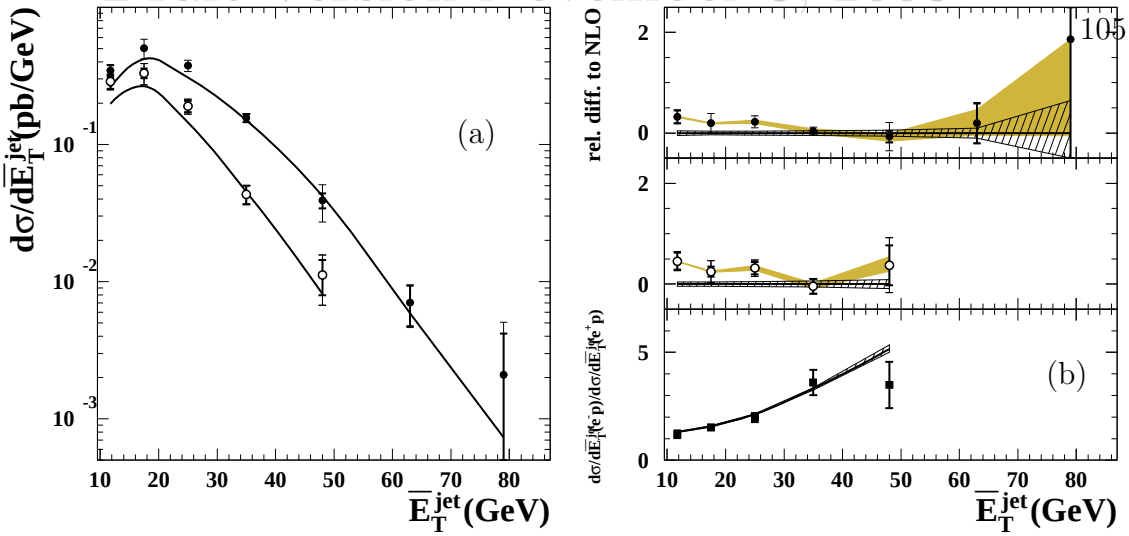

Figure 8.8: Unpolarized e^-p (filled circles) and e^+p (open circles) dijet differential cross sections as a function of $\overline{E}_T^{\rm jet}$ are shown in (a). The relative difference to NLO pQCD calculations are shown in the upper two portions of (b), while the ratio of e^-p and e^+p cross sections are shown in the bottom portion.

available QCD calculations are only lowest order and do not predict the normalization of the data. They were scaled by 1.92 and 1.42 for e^-p and e^+p collisions, respectively, so as to reproduce the measured integrated three-jet cross sections. The integrated cross sections for both data and predictions are presented in Table 8.2. The central values of calculations provide a far better description of the shape of the distributions compared to the dijet cross sections presented in section 8.3, although statistical and theoretical errors are much larger. The peak of the cross section is also near 1, as it was for the dijet systems.

Figures 8.13 to 8.15 show the unpolarized three-jet $\overline{E}_T^{\rm jet}$, Q^2 and the three-jet invariant mass, $m^{\rm 3j}$, where and $\overline{E}_T^{\rm jet} = (E_T^{\rm jet1} + E_T^{\rm jet2} + E_T^{\rm jet3})/3$. Values of $m^{\rm 3j}$ from 20 to 120 GeV are accessible with the present statistics. The predictions of LO QCD are

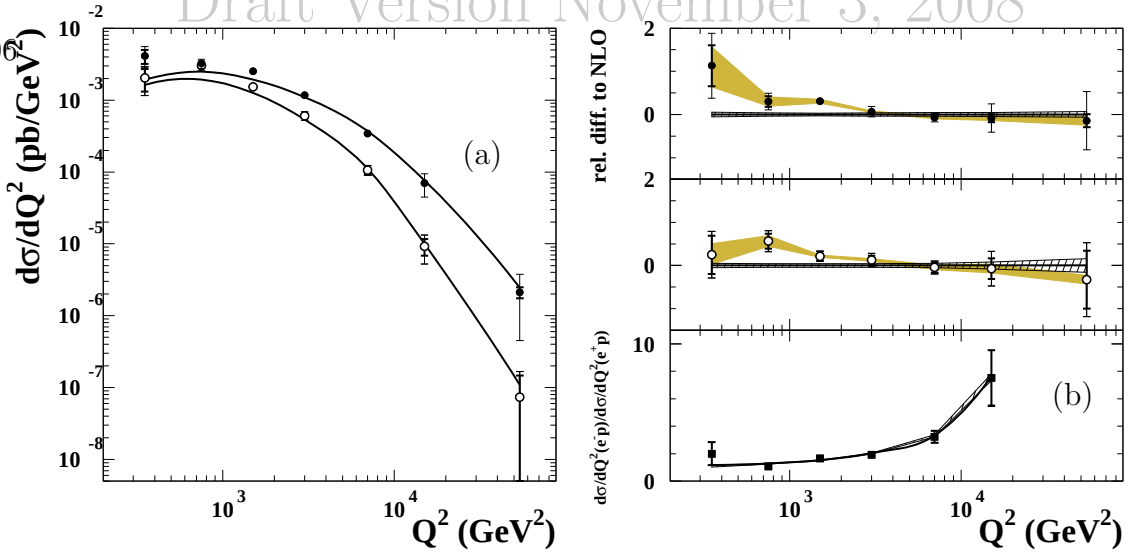

Figure 8.9: Unpolarized e^-p (filled circles) and e^+p (open circles) dijet differential cross sections as a function of Q^2 are shown in (a). The relative difference to NLO pQCD calculations are shown in the upper two portions of (b), while the ratio of e^-p and e^+p cross sections are shown in the bottom portion.

also compared to the data in the figures, and are scaled as described for the $\overline{\eta}^{\rm jet}$ cross sections. The scaled LO calculations give a good description of the shape of the data within statistical uncertainties.

The ratio of e^-p to e^+p differential cross sections versus $\overline{E}_T^{\rm jet}$, presented in the lower part of Figure 8.13b rises from 1 to 4 over the measured range of 8 GeV $< \overline{E}_T^{\rm jet} <$ 29 GeV. The ratios of inclusive, dijet and trijet differential cross sections versus Q^2, presented in Figure 8.5b, Figure 8.9b and Figure 8.14b. Each show similar ranges of change over the range in $400 < Q^2 < 7000$, but higher values of Q^2 were not statistically accessible in the trijet sample.

The three-jet selected sample also contains 9 e^-p and 2 e^+p candidates with a fourth jet of transverse energy above 5 GeV in the $\eta^{\rm jet}$ range $-1 < \eta^{\rm jet} < 2.5$.

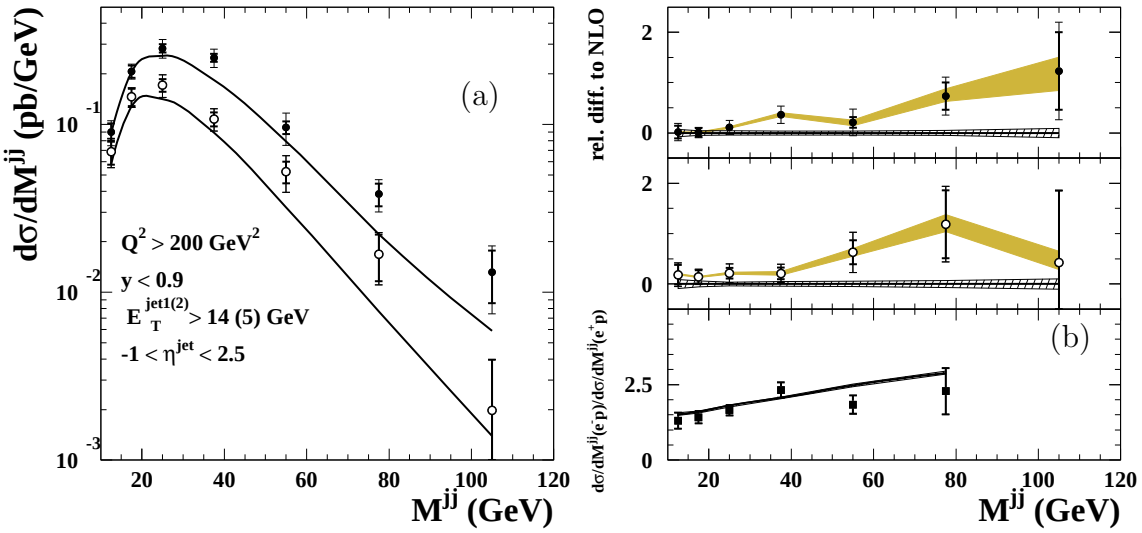

Figure 8.10: Unpolarized e^-p (filled circles) and e^+p (open circles) dijet differential cross sections as a function of m^{jj} are shown in (a). The relative difference to NLO pQCD calculations are shown in the upper two portions of (b), while the ratio of e^-p and e^+p cross sections are shown in the bottom portion.

There are no calculations available at present that would predict the number of 4-jet events in the sample. Assuming that the leading contribution differentiating dijet and trijet systems is single gluon emission, and that the same mechanism is the principle differentiating 3 and 4-jet samples, then the respective ratios should be similar. The ratio of dijets to trijets is approximately 0.098 (0.065), and the ratio of 4-jets to trijets is 0.082 (0.067) for e^-p (e^+p) data, which supports this reasoning.

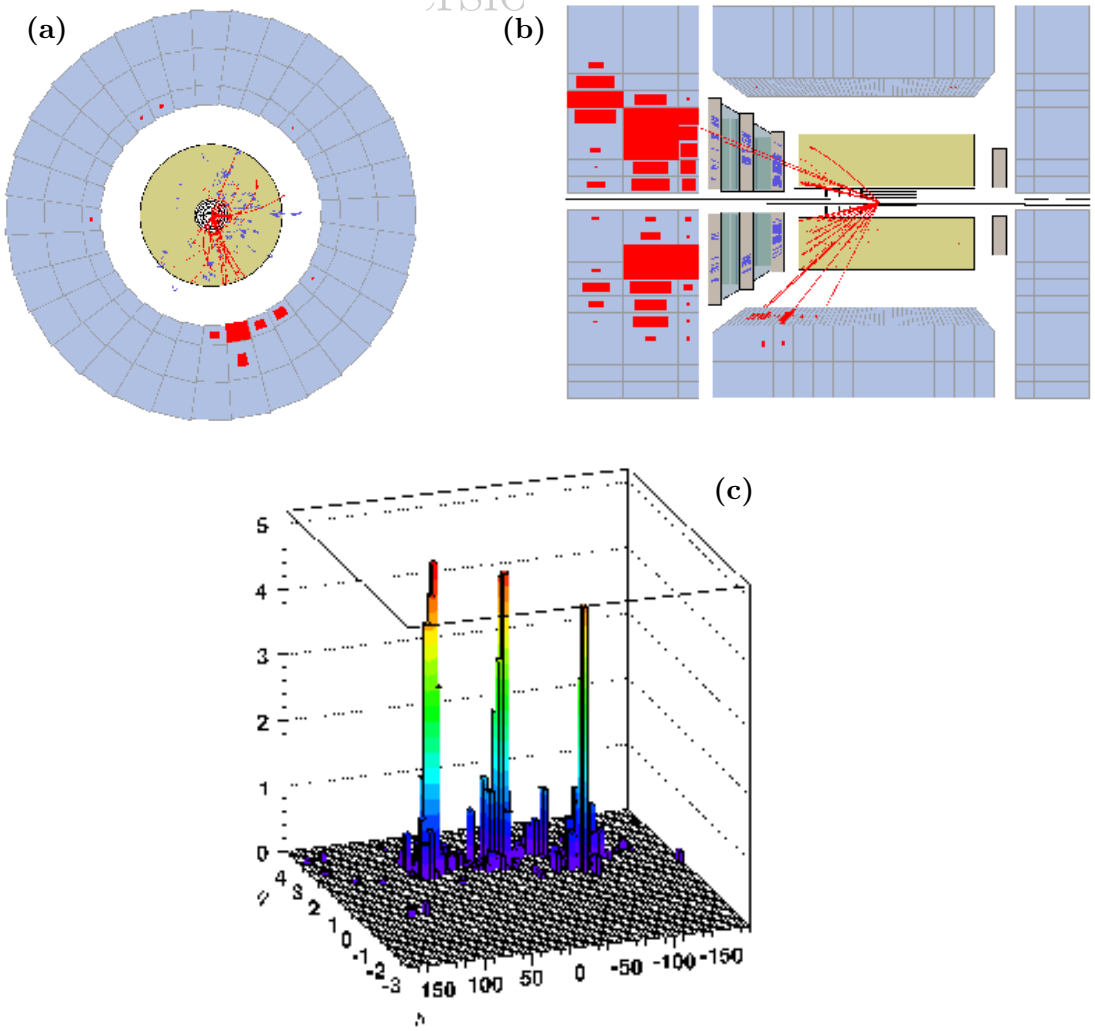

Figure 8.11: Three-jet candidate event in CC DIS in the ZEUS detector. The event is viewed in the $x-y$ plane in (a), the $z-r$ view in (b), and E_T of CAL deposition $\eta-\phi$ plane in (c). In (a) and (b), reconstructed tracks are superimposed over CTD hits, and CAL depositions are drawn proportional to the energy deposited. In (a), only the energy deposition in the barrel calorimeter is shown. In (a) an imbalance in the azimuthal distribution of tracks is observed. In (c), three broad CAL deposits are observed, which are separated in the $\eta-\phi$ plane. In (b), these are observed to penetrate into the second hadronic section of the CAL. These deposits were reconstructed as three jets.

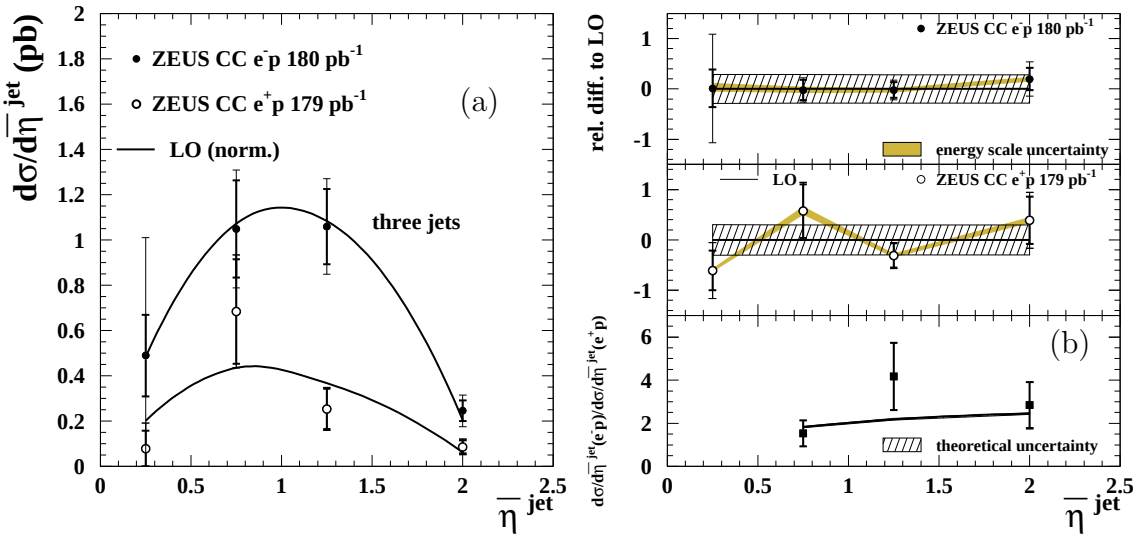

Figure 8.12: Unpolarized e^-p (filled circles) and e^+p (open circles) trijet differential cross sections as a function of $\overline{\eta}^{\rm jet}$ are shown in (a). The relative difference to LO pQCD calculations are shown in the upper two portions of (b), while the ratio of e^-p and e^+p cross sections are shown in the bottom portion.

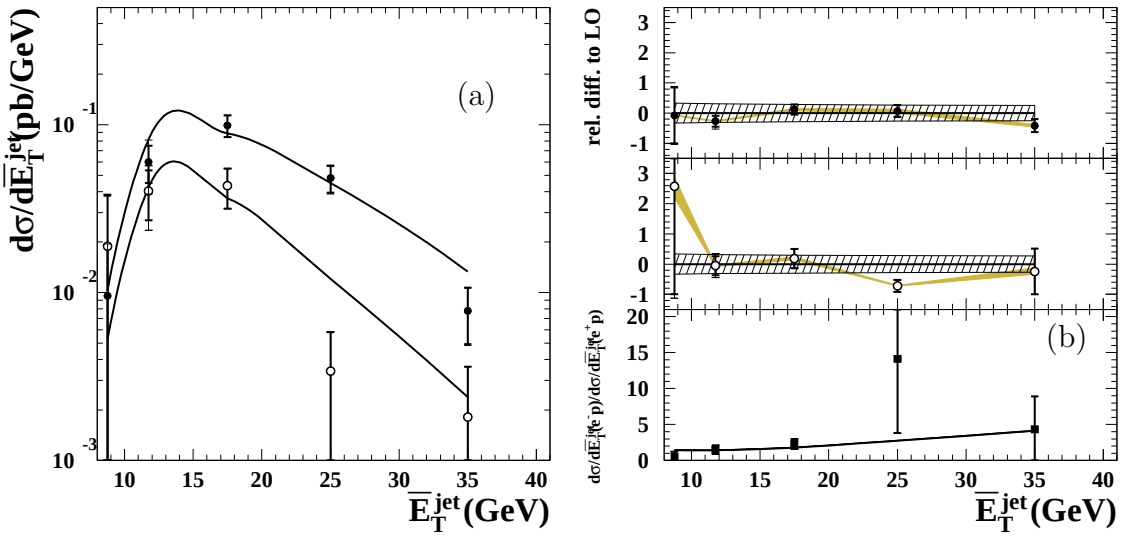

Figure 8.13: Unpolarized e^-p (filled circles) and e^+p (open circles) trijet differential cross sections as a function of $\overline{E}_T^{\rm jet}$ are shown in (a). The relative difference to LO pQCD calculations are shown in the upper two portions of (b), while the ratio of e^-p and e^+p cross sections are shown in the bottom portion.

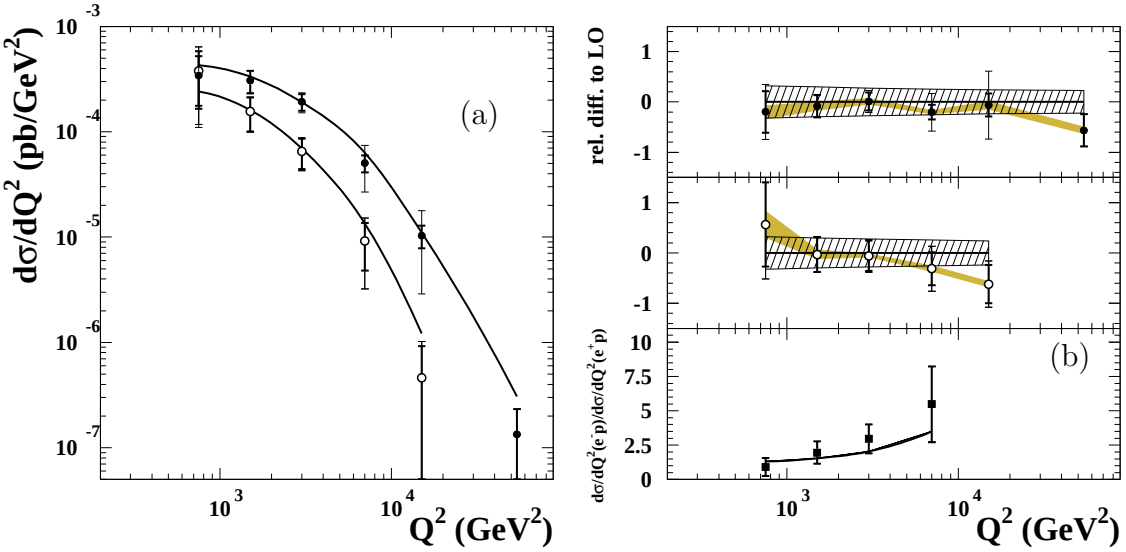

Figure 8.14: Unpolarized e^-p (filled circles) and e^+p (open circles) trijet differential cross sections as a function of Q^2 are shown in (a). The relative difference to LO pQCD calculations are shown in the upper two portions of (b), while the ratio of e^-p and e^+p cross sections are shown in the bottom portion.

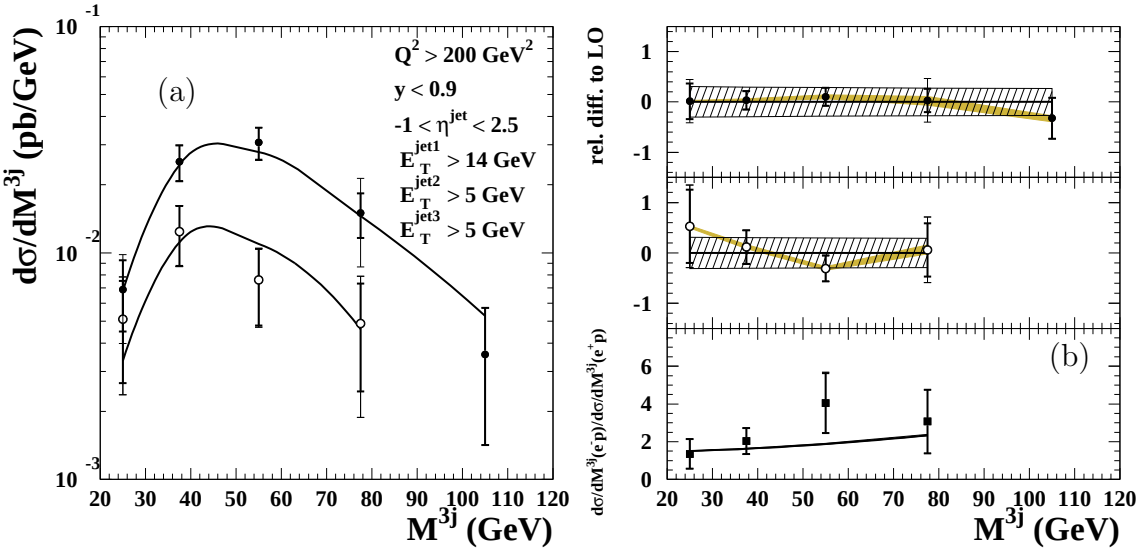

Figure 8.15: Unpolarized e^-p (filled circles) and e^+p (open circles) trijet differential cross sections as a function of m^{3j} are shown in (a). The relative difference to LO pQCD calculations are shown in the upper two portions of (b), while the ratio of e^-p and e^+p cross sections are shown in the bottom portion.

Chapter 9

Conclusions

Measurements of polarized and unpolarized integrated and differential multi-jet cross sections in CC $e^{\pm}p$ DIS were made using 0.36 fb^{-1} of data collected with the ZEUS detector at HERA, covering the entire HERA II data sample. The measurements were made in the kinematic region defined by $Q^2 > 200$ GeV^2 and $y < 0.9$. Jets were identified in the laboratory frame using the k_T cluster algorithm in the longitudinally invariant inclusive mode.

Polarized differential and integrated inclusive-jet cross sections were measured over the phase-space region as functions of η^{jet}, E_T^{jet}, Q^2 and x for jets with $E_T^{\text{jet}} > 14$ GeV and $-1 < \eta^{\text{jet}} < 2.5$. The measured cross sections are in good agreement with the SM predictions provided by MEPJET 2.1 [10] calculations. The ratios of the differential cross sections for negative and positive longitudinally-polarized lepton beams are also well described by the same predictions.

Unpolarized differential inclusive-jet cross sections were measured as functions of η^{jet}, E_T^{jet}, Q^2 and x for jets with $E_T^{\text{jet}} > 14$ GeV and $-1 < \eta^{\text{jet}} < 2.5$. The ratio of the differential cross sections for e^-p and e^+p collisions as a function of η^{jet} is ≈ 2 in the range $-1 < \eta^{\text{jet}} < 2.5$, as predicted by the SM predictions provided by MEPJET 2.1

calculations. The ratio as a function of $E_T^{\rm jet}$ (Q^2) increases as $E_T^{\rm jet}$ (Q^2) increases, in agreement with the expected increased contribution from the valence-quark densities in the proton at high x and the fact that both reactions are sensitive to different quark flavors.

NLO QCD predictions for inclusive-jet CC DIS computed using the MEPJET 2.1 program were observed to provide a good description of the measured cross sections. A detailed study of the theoretical uncertainties was performed: they are dominated by the uncertainty contributed by the ZEUS-S [22] PDF set. The predictions from the MRST2001 [21] and CTEQ5D [18, 19, 20] PDF sets were also compared to the measured inclusive-jet cross sections, and show differences between predictions on the order of the uncertainties from the ZEUS-S set. The uncertainties due to the PDFs are larger for e^+p than for e^-p collisions, due to the larger relative uncertainty of the d PDF [22]. Therefore, these measurements, if used together with other data in global PDF fits such as CTEQ or MSTW, have the potential to constrain the flavor content of the proton at $x \gtrsim 10^{-2}$.

Unpolarized Dijet differential cross sections were measured for jets with $E_T^{\rm jet1} >$ 14 GeV, $E_T^{\rm jet2} > 5$ GeV and $-1 < \eta^{\rm jet} < 2.5$. These cross sections were measured as functions of Q^2, dijet invariant mass, mean $E_T^{\rm jet}$, and mean $\eta^{\rm jet}$ of the two jets. The comparison of NLO QCD predictions computed using the MEPJET 2.1 program with the measured dijet differential cross sections shows a poor agreement in both shape and normalization. Because these dijet distributions contain significant contributions from boson-gluon fusion, they are sensitive to the gluon content of the proton.

Three-jet differential cross sections were measured for the first time in CC DIS.

The cross sections were measured for jets with $E_T^{\text{jet1}} > 14$ GeV, $E_T^{\text{jet2}} > 5$ GeV, $E_T^{\text{jet3}} > 5$ GeV and $-1 < \eta^{\text{jet}} < 2.5$. The LO QCD predictions provide a good description of the shape of the data, but do not describe the normalization. The dominant source of theoretical uncertainty was due to higher order terms not present in the calculations.

The three-jet sample also contains eleven candidates with a fourth jet of $E_T^{\text{jet}} > 5$ GeV in the range $-1 < \eta^{\text{jet}} < 2.5$. This represents the first observation of 4-jet events in CC DIS. This number cannot be accurately predicted with present calculations, but the naive comparison of the ratio of the number of 4-jet events to the number of trijet events is similar to the same ratio for trijets and dijets.

The largest source of uncertainty in the measured cross sections are statistical. The natural suggestion to improve the present study would then be increased statistics, but because no other *ep* collider is currently approved for funding, this increase must come from alteration of event selection over the existing data. The trigger selection for the present sample was observed to be $\sim 95\%$ efficient, and the final sample was observed to contain negligible contamination by other processes. The event selection after triggering, however, showed significant reduction in efficiency to 60% for inclusive-jets, so improvements to the selection could prove beneficial. The present value of P_T^{miss} cut is already optimized because of trigger conditions. The minimum E_T^{jet} cut for inclusive jets or the highest E_T^{jet}-jet are predetermined by the P_T^{miss} cut due to kinematic correlation between P_T^{miss} and the E_T of the highest E_T^{jet}-jet. The choice of the phase space cut $y < 0.9$ is needed to ensure proper reconstruction of Q^2, and very few events are present above this cut. Increasing statistics of the sample would therefore imply the improvement of cleaning cuts, which is challenging due to

the large variety of ep and non-ep background sources. Because the cleaning cuts chosen have already been optimized, any alternative method would risk introducing additional systematic uncertainty.

The measurements contained in this work represent the largest sample of Multi-jets in CC DIS, from the world's first and only ep collider. These results are at present the only published sample of jets in CC DIS with longitudinally-polarized leptons. While the theoretical predictions match the data within uncertainties for inclusive-jet production, the uncertainty due to the choice of PDFs dominates, and the data shows the capacity to differentiate between competing PDF sets, specifically the d PDF. Therefore, the results presented here show the potential to constrain the proton PDFs, and should be included in PDF fits to global data.

Appendix A

Monte Carlo And Data Comparisons

In this appendix, supplimentary comparisons between data and monte carlo are presented for e^+p events. Equivalent comparisons are shown in section 7.1.2.

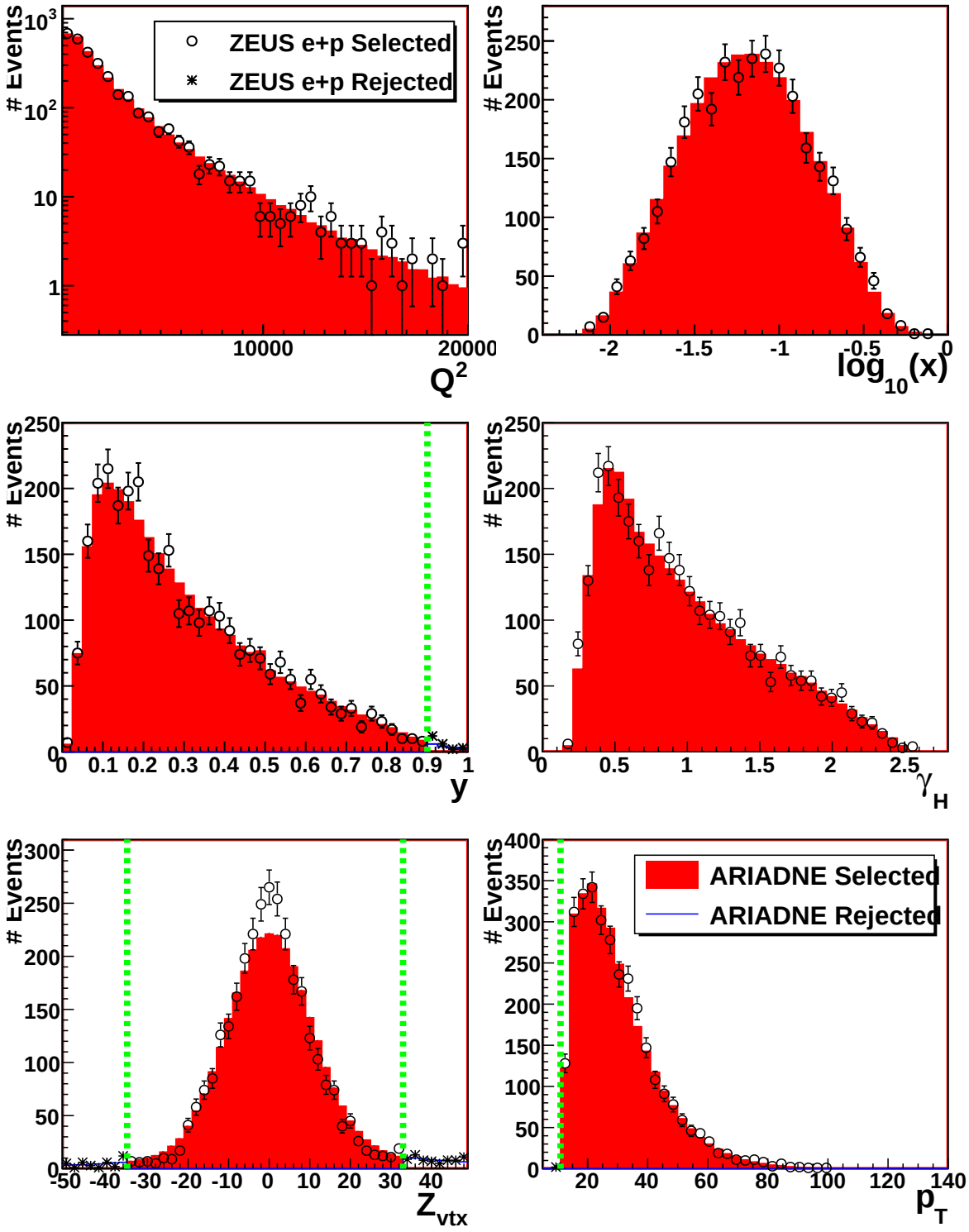

Figure A.1: Comparison between detector level kinematic quantities of e^+p data and ARIADNE. All details as in figure 7.1.

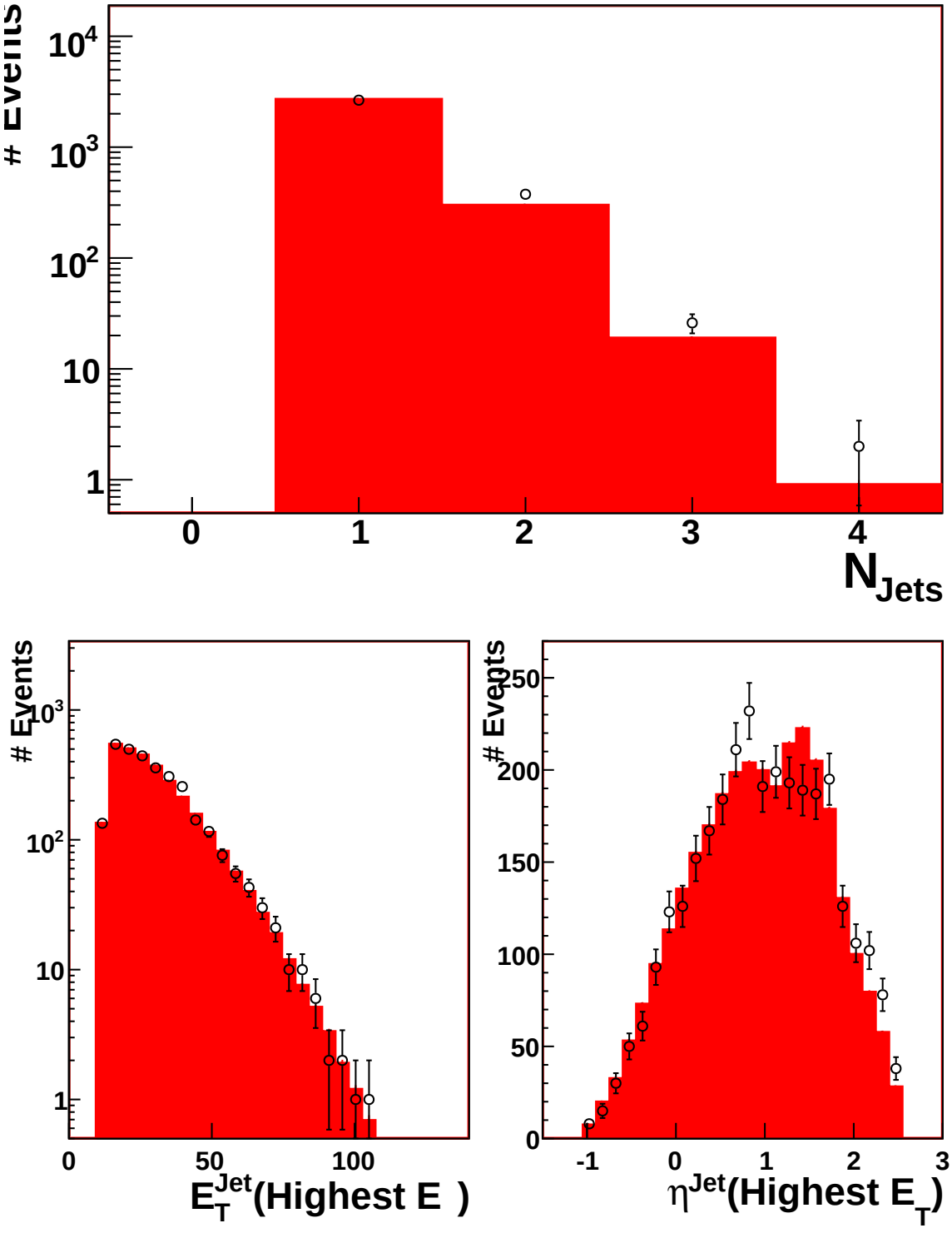

Figure A.2: Comparison between detector level jet quantities of e^+p data and ARIADNE. All details as in figure 7.2.

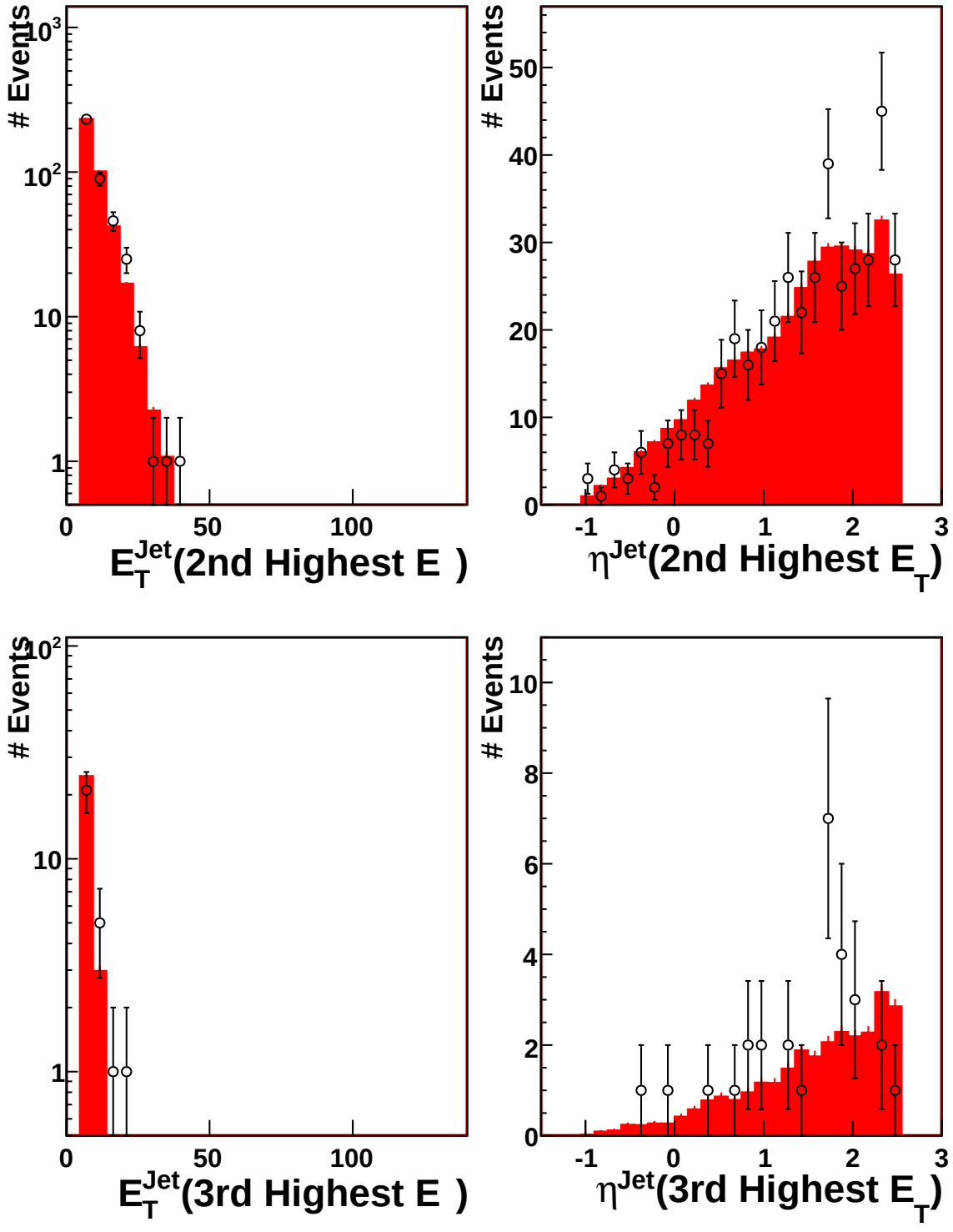

Figure A.3: Comparison between detector level jet quantities of e^+p data and ARIADNE. All details as in figure 7.2.

Appendix B

Reweighting Factors

The weight as a function of the generated z_{vtx} was computed as

$$w_z(z_{vtx}^{gen}) = 0.999 - 1.272 \times 10^{-3} * z_{vtx}^{gen} \text{ for electrons} \quad \text{(B.1)}$$

$$w_z(z_{vtx}^{gen}) = 0.982 - 4.966 \times 10^{-3} * z_{vtx}^{gen} \text{ for positrons} \quad \text{(B.2)}$$

The weight as a function of the generated Q^2 was computed as

$$w_{Q^2}(Q^2_{gen}) = 1.464 - 0.1385 \times 10^{-3} * \log_{10}(Q^2_{gen}) \text{ for electrons} \quad \text{(B.3)}$$

$$w_{Q^2}(Q^2_{gen}) = 1.5542 + -0.2147 \times 10^{-3} * \log_{10}(Q^2_{gen}) \text{ for positrons} \quad \text{(B.4)}$$

The weight function to account for the tracking veto was provided by the ZEUS tracking group, and will not be discussed here.

The effects of the reweighting are shown in figures B.1 and B.2. It can be seen from the figures that the reweighting procedure greatly improves the overal description of Q^2 for both samples. The z_{vtx} distribution for all ZEUS monte carlo is generated to empirically match the data for the run ranges considered. The difference in shape of the z_{vtx} distribution shown for positron data in figure B.2 is because the monte carlo was generated before the end of data taking, and the z_{vtx} distribution used does not represent that of the final data sample.

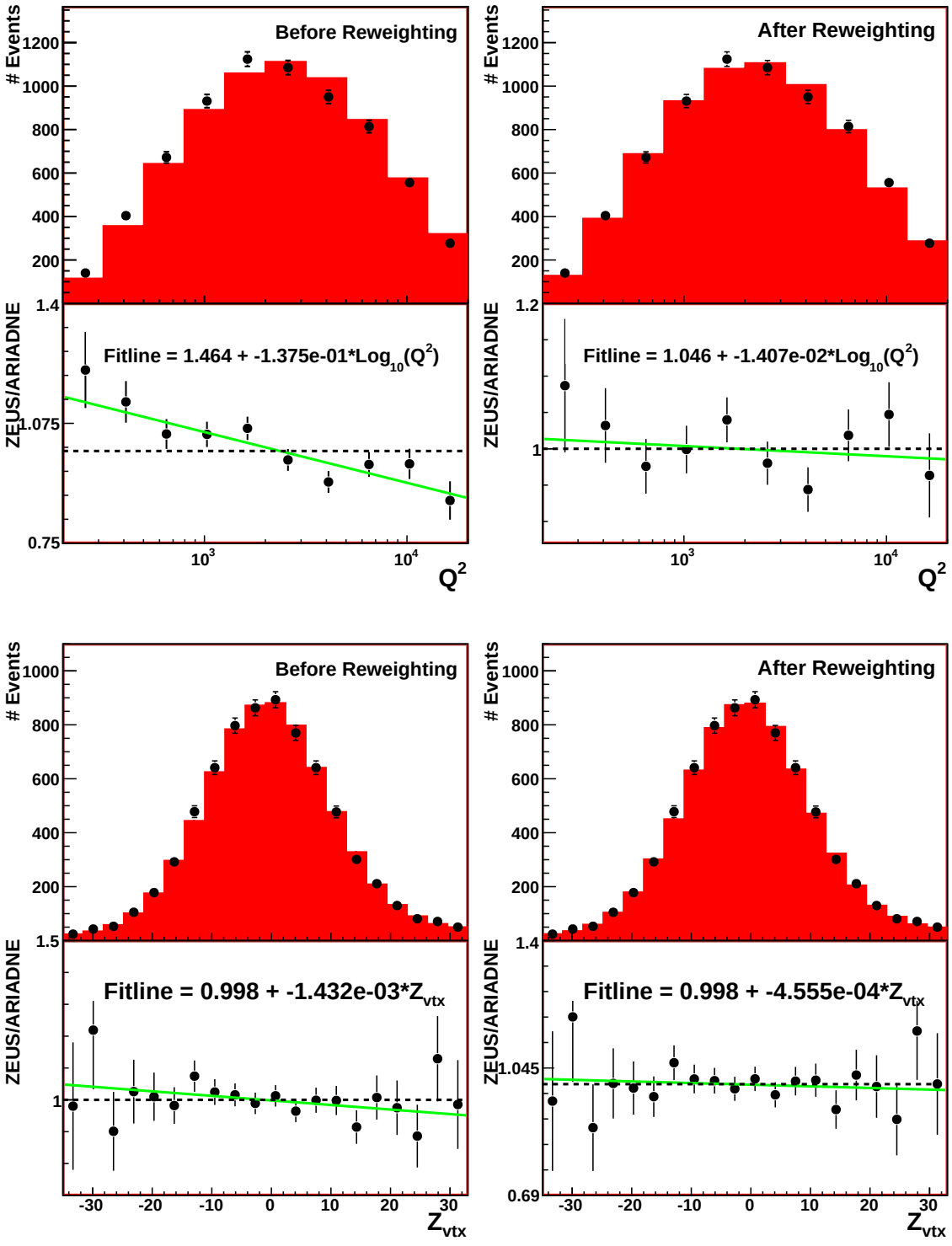

Figure B.1: Plots comparing detector level distributions of $e^- p$ data versus ARIADNE. The two upper plots show Q^2, while the bottom two show z_{vtx}. The left two plots show distributions without monte carlo reweighting, while the right two show the same data distributions, but compared to reweighted monte carlo. The monte carlo distributions have been area-normalized to the data. Below each distribution, a ratio plot is shown of data/ARIADNE. A linear χ^2 fit is shown for each ratio.

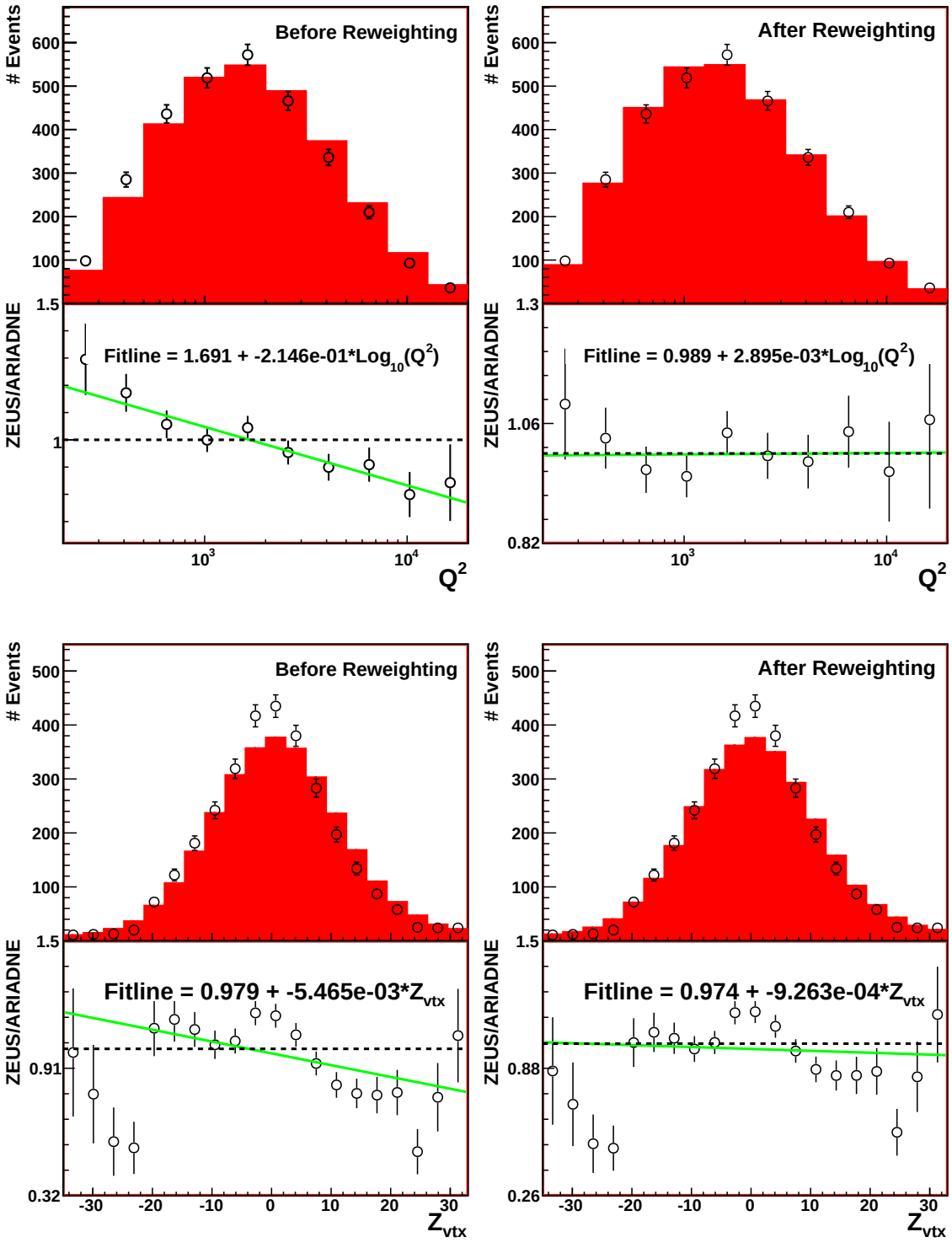

Figure B.2: Plots comparing detector level distributions of e^+p data versus ARIADNE. All details as in figure B.1.

Appendix C

Purities, Efficiencies, Acceptances

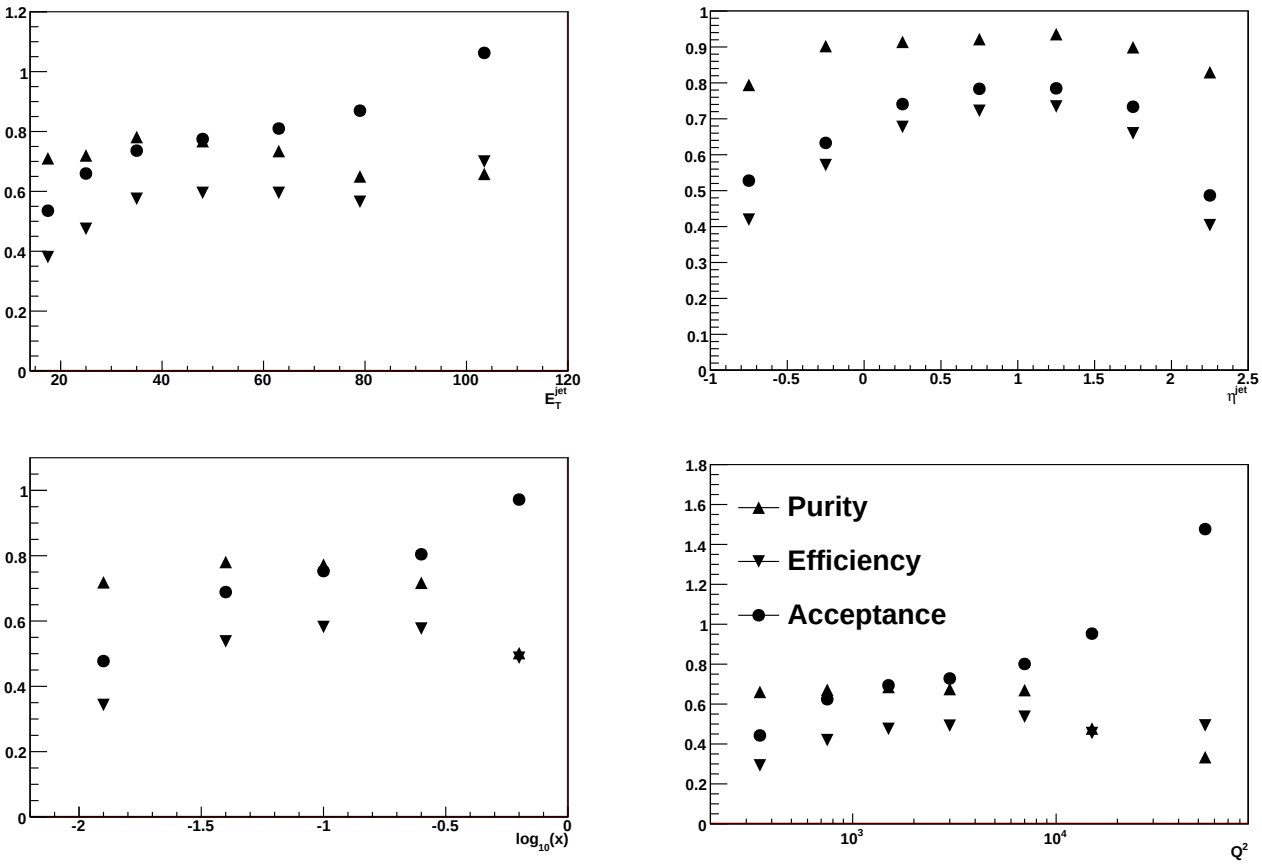

Figure C.1: *Inclusive Jet Purity, Efficiency, Acceptance e^-p ARIADNE*

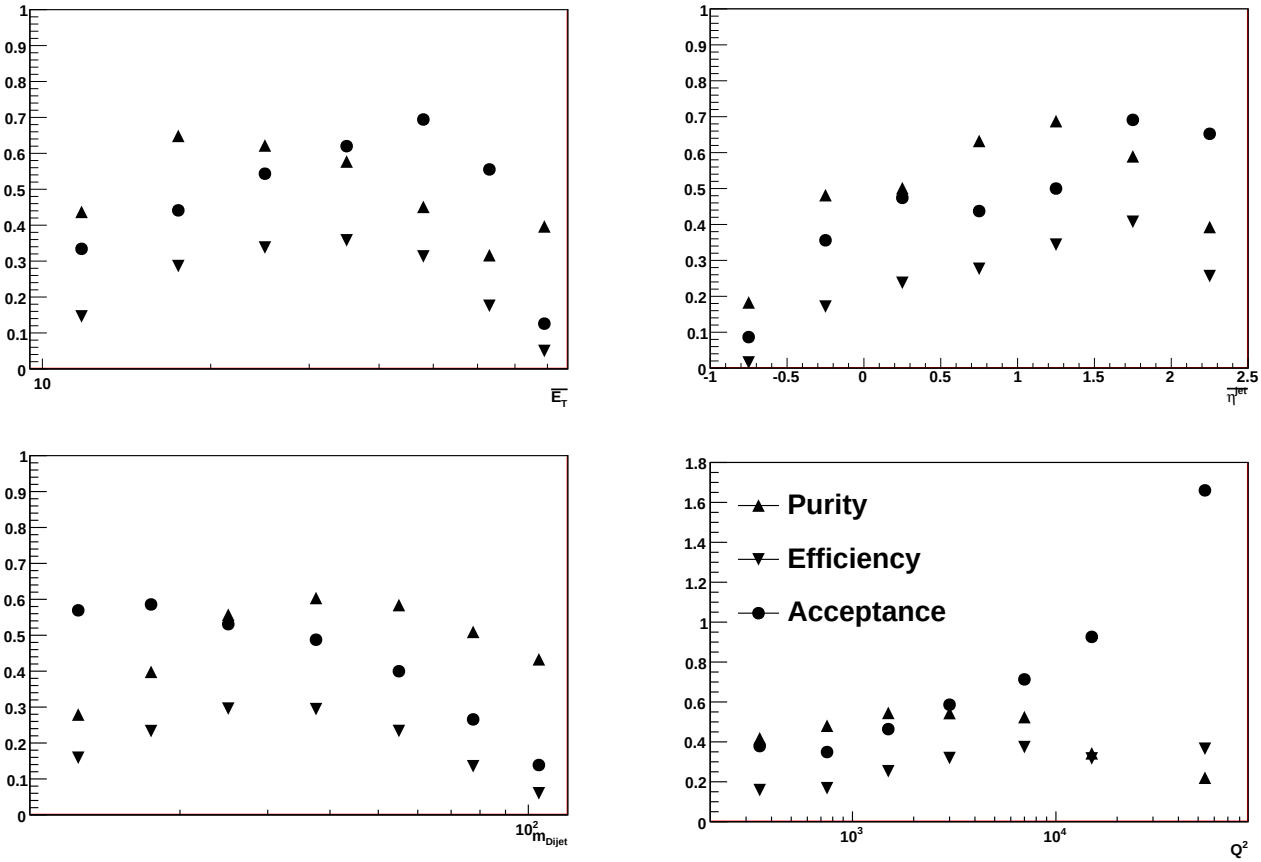

Figure C.2: *Dijet Jet Purity, Efficiency, Acceptance $e^{-}p$ ARIADNE*

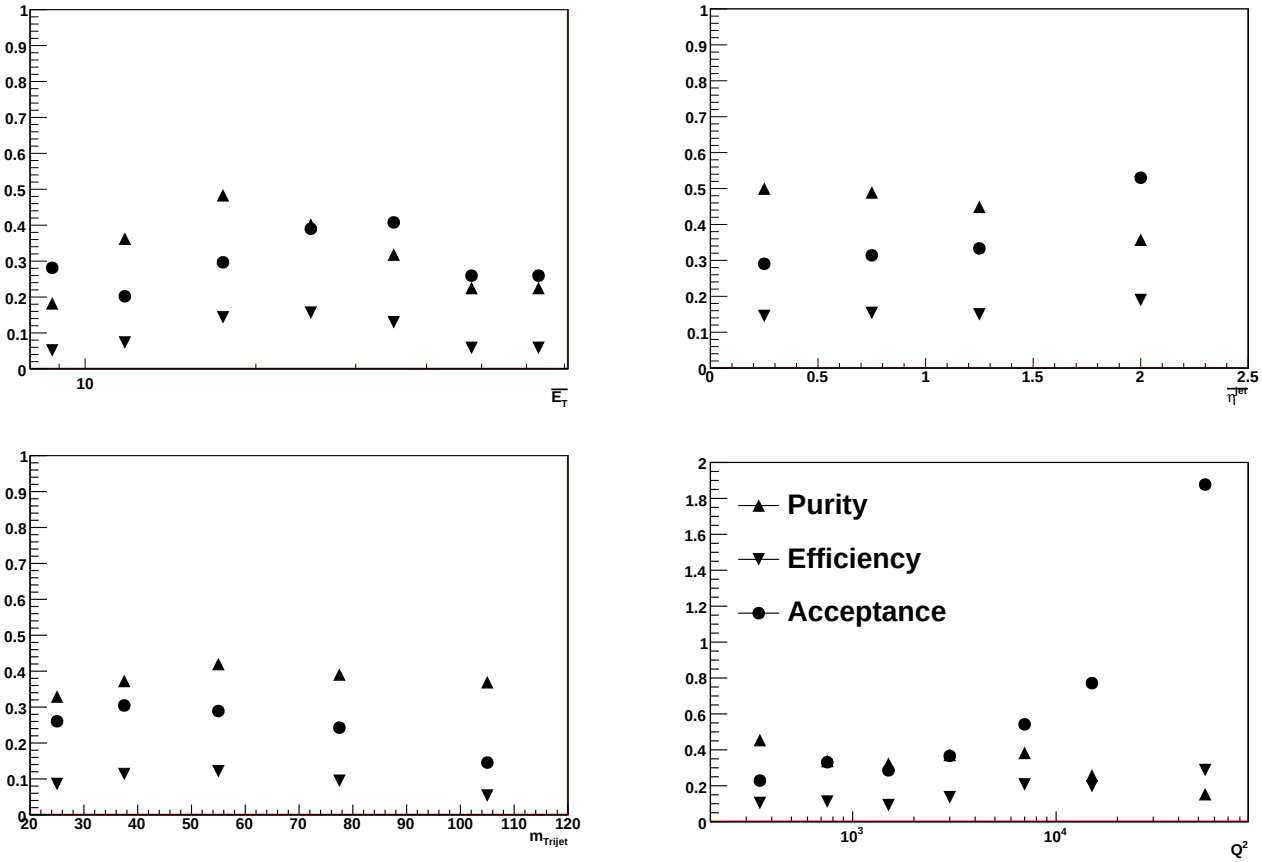

Figure C.3: *Trijet Jet Purity, Efficiency, Acceptance e^-p ARIADNE*

Appendix D

Systematic Uncertainties

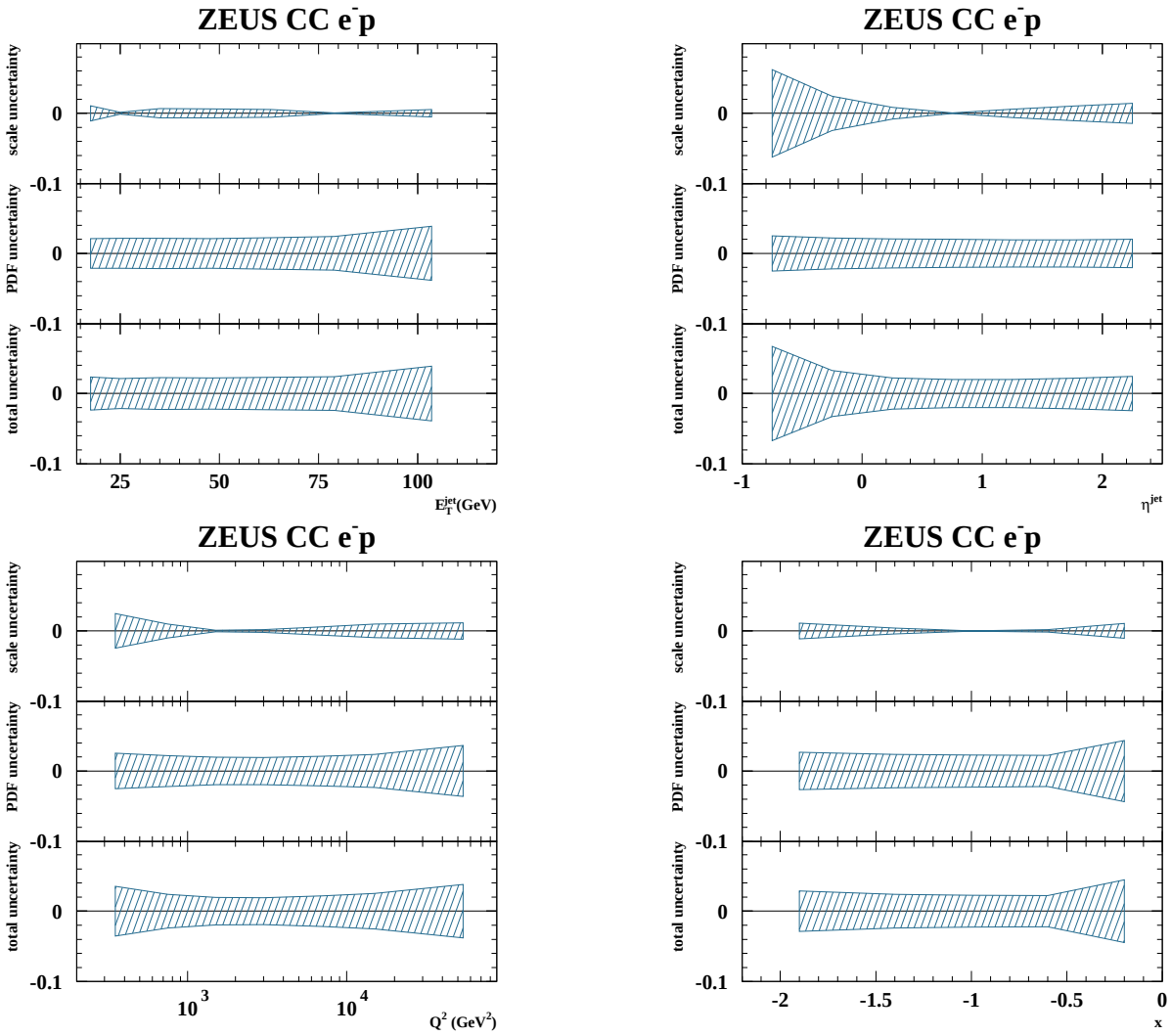

Figure D.1: *Inclusive Jet Theoretical Uncertainties* $e^- p$

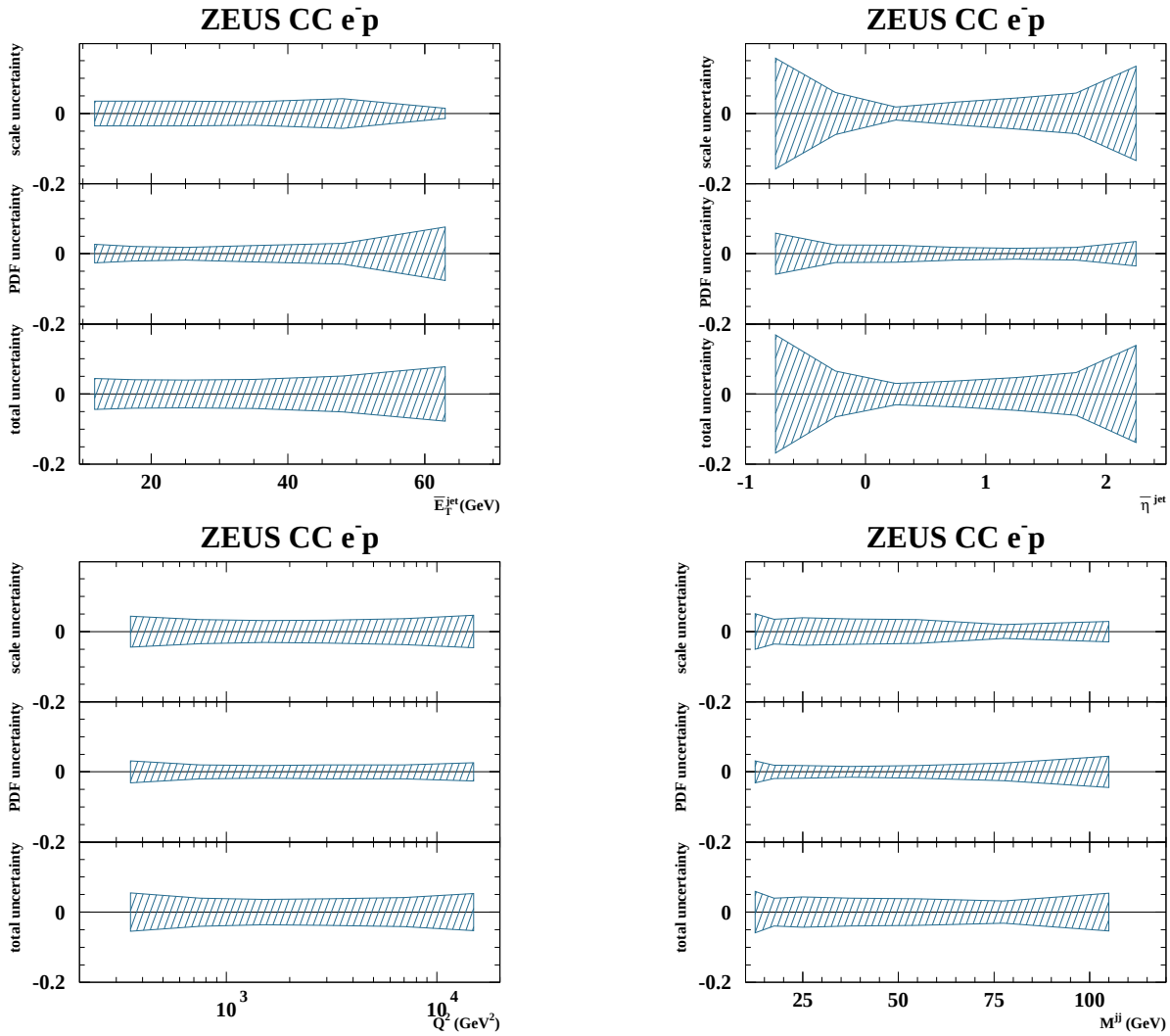

Figure D.2: *Dijet Theoretical Uncertainties* $e^- p$

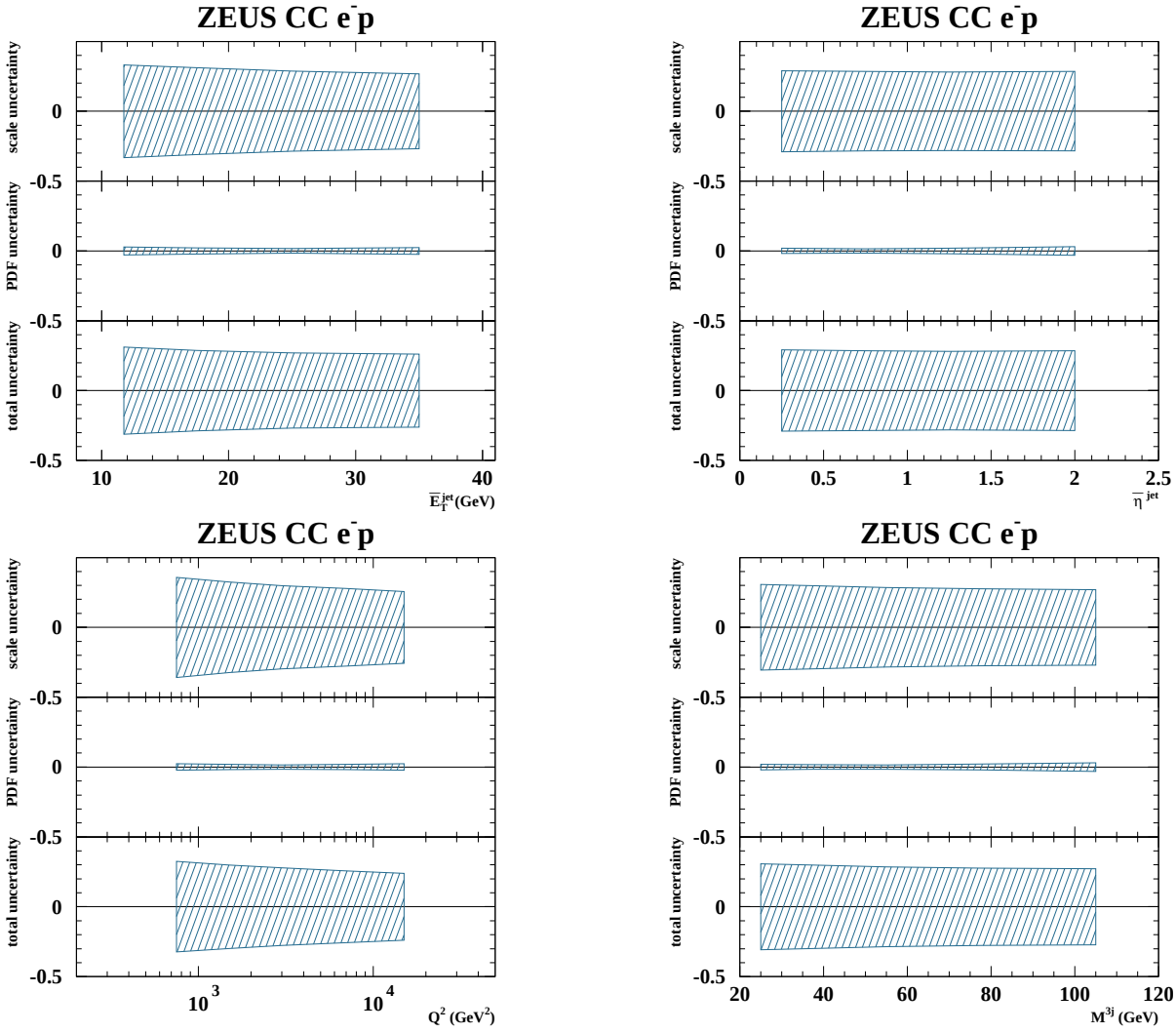

Figure D.3: *Trijet Theoretical Uncertainties* $e^- p$

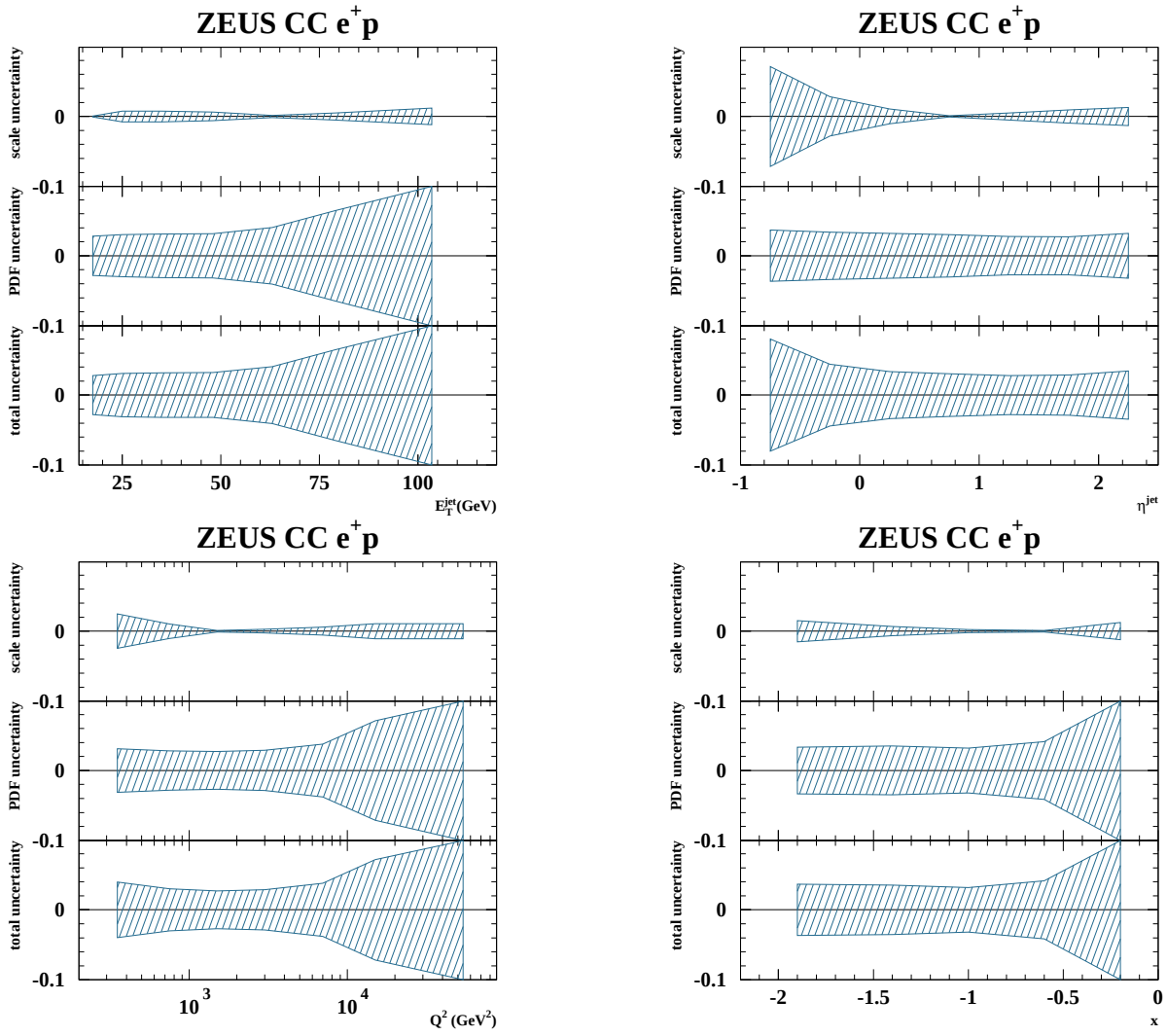

Figure D.4: *Inclusive Jet Theoretical Uncertainties* e^+p

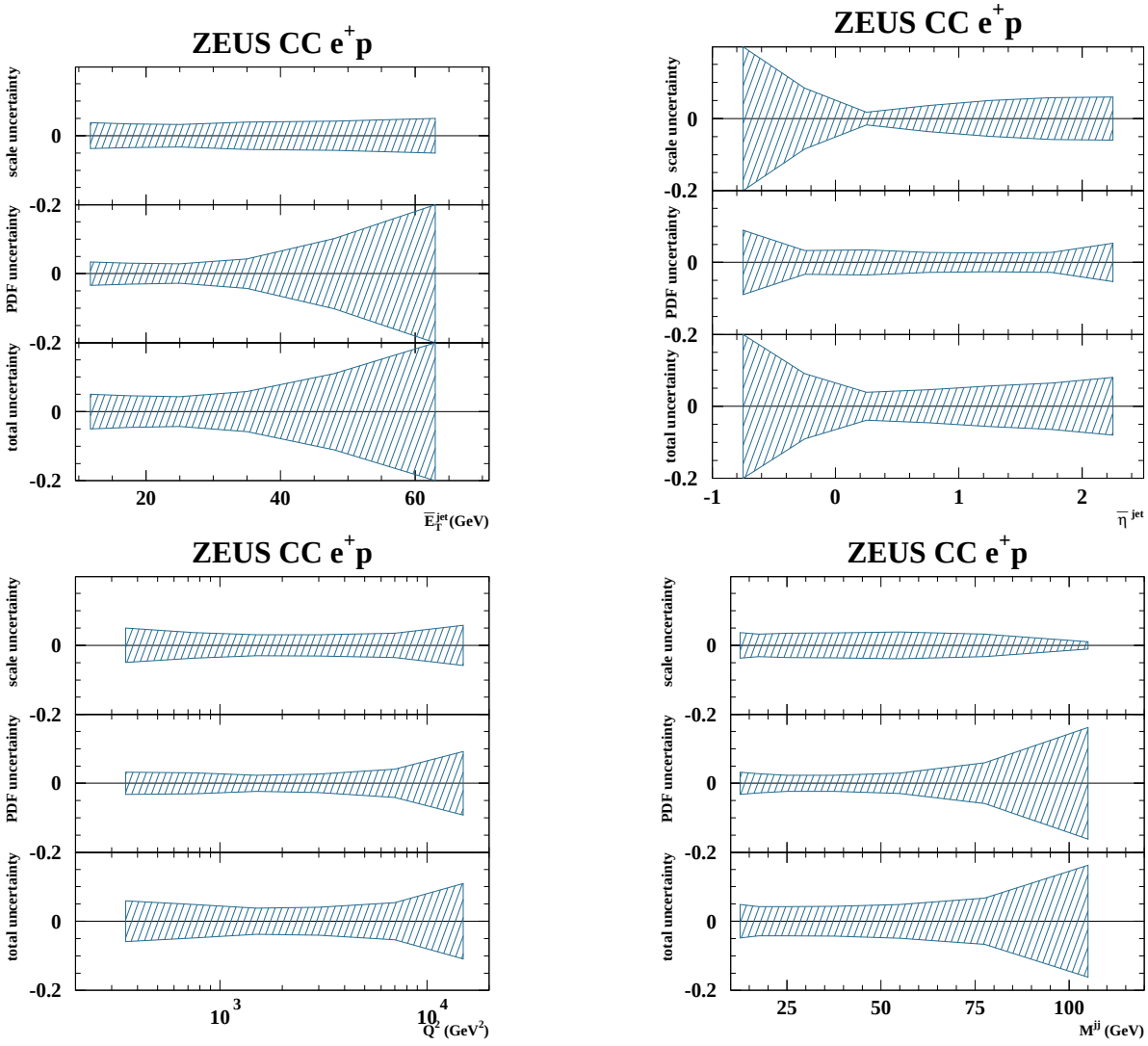

Figure D.5: *Dijet Theoretical Uncertainties* e^+p

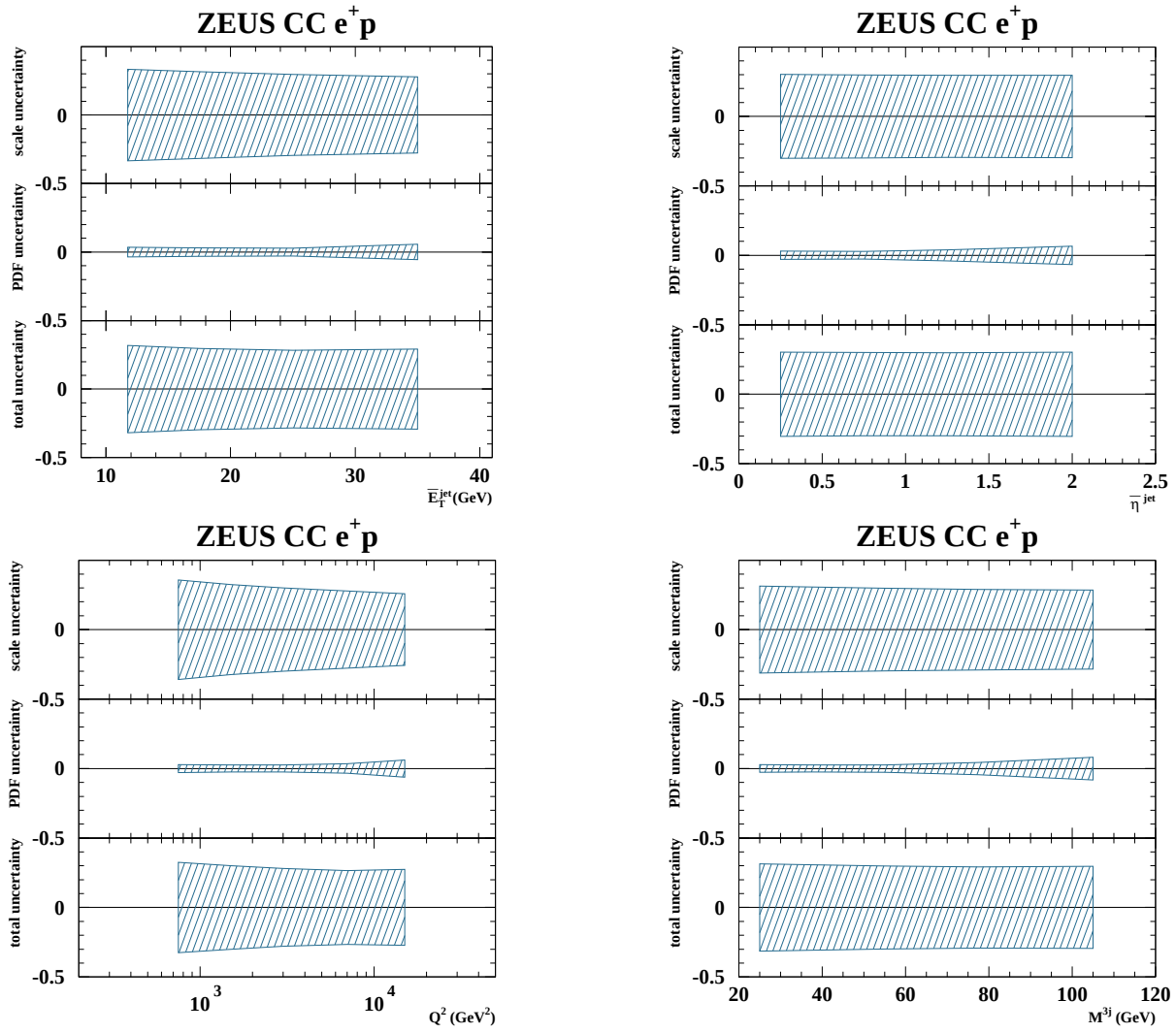

Figure D.6: *Trijet Theoretical Uncertainties* e^+p

Appendix E

Technical Trigger Specifications

All trigger bits at each level described below additionally have overriding vetoes from timing information provided by the calorimeter, C5, SRTD, or Global Calorimeter. This timing information is used to reject background events including beamgas, halo muon, cosmic muons.

E.1 First Level Trigger Selection

The FLT was divided into 64 independent bits, each of which recorded a true or false state for each event depending on specific physical conditions. The FLT bits used in the principle and secondary selections are listed in table E.1. For each trigger analysis, at least one bit in the FLT selection was required to be set to true. The bits definition depended on the run number, specifically in the case of bits 60 and 63, which changed on run 54115.

In table E.1, tight track veto refers to selection vetoes where events were rejected due to a large number of non-vertex tracks. B_{isoe} is true if an isolated calorimeter deposit in the BCAL was located which is consistent with an isolated electron. N_{gt} is the number of tracks found with strict quality standards. E_{EMC} and E_{BEMC} are the

FLT bit number	Principle	Alternative	Description
31		✓	$E_{T,Fbp} + E_T \geq 45$ GeV
39	✓	✓	$E_{BEMC} \geq 3$ GeV and B_{isoe} and $N_{\rm gt} \geq 1$ and Loose Track Veto
40	✓	✓	$E_{EMC} \geq 25$ GeV and Tight Track Veto
41	✓	✓	$E_T \geq 30$ GeV and Tight Track Veto
43	✓	✓	$E_T \geq 12$ GeV and $N_{\rm gt} \geq 1$ and Tight Track Veto
44	✓	✓	($E_{BEMC} \geq 10$ GeV or $E_{REMC} \geq 3$ GeV), B_{isoe}, $N_{\rm gt} \geq 1$, and Tight Track Veto
50		✓	$(E_{CAL} \geq 15$ GeV$\|\|E_{EMC} \geq 10$ GeV$\|\|E_{BEMC} \geq 3$ GeV$\|\|E)_{REMC} >= 2$ GeV)&&TRK_q95b&&$(Et_HFL >= 892)$
60 (Run $\leq$ 54115)	✓	✓	($P_T^{\rm miss} > 5$ GeV and $E_{T,-2IR} > 5$ GeV and $N_{vtxtrk} \geq 1$) or ($P_T^{\rm miss} > 8$ GeV and $N_{trks} \geq 1$) or ($P_T^{\rm miss} > 8$ GeV and $E_{FCAL} \geq 10$ GeV) and not FCLR beam gas
60 (Run $>$ 54115)	✓	✓	($P_T^{\rm miss} > 5$ GeV and $E_{T,-2IR} > 5$ GeV and $N_{vtxtrk} \geq 1$) or ($P_T^{\rm miss} > 11.5$ GeV and $N_{trks} \geq 1$) or ($P_T^{\rm miss} > 11.5$ GeV and $E_{FCAL} \geq 10$ GeV) and not FCLR beam gas
63 (Run $>$ 54115)	✓	✓	($P_T^{\rm miss} > 5$ GeV and $E_{T,-2IR} > 5$ GeV and $N_{vtxtrk} \geq 1$) or ($P_T^{\rm miss} > 8$ GeV and $N_{trks} \geq 1$) or ($P_T^{\rm miss} > 11.5$ GeV and $E_{FCAL} \geq 10$ GeV) and not FCLR beam gas

Table E.1: First Level Trigger bits used in this analysis.

energies located in the entire EMC and Barrel EMC, respectively. Additional vetoes from the C5 counter and Veto Wall apply to all bits.

In FLT60 before run 54115, an event was vetoed by the FCLR if the highest energy RCAL cluster had an energy greater than 50 GeV, and the highest energy tower in the highest energy RCAL cluster was located in the inner ring of the RCAL. Due to increased dead time during 2005 data taking, the requirements of FLT60 was divided up into two bits: FLT60 and FLT63. FLT60 and FLT63 after run 54115 had the same veto conditions as FLT60 before run 54115, but afterwards FLT63 additionally was FCLR vetoed if $E - p_z < 3$ GeV

E.2 Second Level Trigger Selection

In the principle selection, events were required to have SLT bit EXO04 set to true. Elements of SLT EXO04 are defined in table E.2. SLT EXO04 was true if all of the following conditions were satisfied:

- (CCtimeOK||CCCTDOK)
- NoOffBeamProton
- (CC1||CC2 ||CC3||CC4)

The alternate selection required that the SLT bit HPP05 was set to true, which was satisfied if all the following conditions were met:

- FLT: 28,30,31,39,40,41,42,43,44,50, or 60
- $N_{\mathrm{gt}} \geq 1$
- $P_T^{\mathrm{miss}} > 8$ GeV

$N^{\mathrm{G}}{}_{\mathrm{PMT}}$	The number of PMTs in the global calorimeter
CCtimeOK	$\lvert T_{\mathrm{G}}\rvert < 7\,\mathrm{ns}$ and $N^{\mathrm{G}}{}_{\mathrm{PMT}} > 1$
CCCTDOK	$N_{\mathrm{trk}} \geq 1$ and $Z_{\mathrm{vtx}} < 100\,\mathrm{cm}$
NoOffBeamProton	$\lvert p_y\rvert > 3$ GeV or $P_T^{\mathrm{miss}} > 15$ GeV or $P_T^{\mathrm{miss}}(-1IR) > 6$ GeV or $P_T^{\mathrm{miss}} > 0.06 p_z$
CC1	$P_T^{\mathrm{miss}} > 6$ GeV and $E_T(-2IR) > 6$ GeV and $N_{\mathrm{gt}} > 1$
CC2	$P_T^{\mathrm{miss}} > 9$ GeV and $P_T^{\mathrm{miss}}(-1IR) > 8$ GeV and $E_{FCAL} > 20$ GeV
CC3	$P_T^{\mathrm{miss}} > 9$ GeV and $(P_T^{\mathrm{miss}})^2 > 2.31 \times E_T$ and $E_{FCAL} > 80$ GeV
CC4	$E - p_z > 6$ GeV and $(P_T^{\mathrm{miss}})^2 > 2.25 \times E_T$ and $N_{\mathrm{gt}} > 1$

Table E.2: EXO4 Second Level Trigger Definitions

- $E_T^{cone} > 8$ GeV
- $P_T^{\rm miss}/E_T > 0.3$

E.3 Third Level Trigger Selection

The principle selection required that either the TLT bit EXO02 or EXO06 was set to true. TLT EXO02 was true if all of the following conditions were satisfied:

- $P_T^{\rm miss} > 6$ GeV
- $|z_{vtx}| < 60$ cm
- UDTimeOK

where UDTimeOK compares the timing information from the upper and lower half of the calorimeter. This condition rejected cosmic rays, which often come from above the ZEUS detector, and interact with the top and bottom at different times. The veto was set to 8ns. EXO06 was set to true if all of the following conditions were met:

- $P_T^{\rm miss} > 6$ GeV
- $\left(E_{FCAL} > 10 \text{ GeV} \parallel N_{\rm gt} > 0\right)$
- OffBeamProton
- BeamGasVertex
- (TooManyBeamGasTracks —— (Good Vertex && $N_{vtxtracks} \geq 2$))
- $\left(N_{CTDhits} < 2500 \| P_T^{\rm miss} > 10 \text{ GeV}\right)$

- UDTimeOK

The alternative trigger required one of TLT bits HPP05, HPP06, HPP10 to be set to true. HPP TLT 05 true was equivalent to all of the following being true:

- HPP SLT 5 == true
- $P_T^{\text{miss}} > 8$ GeV
- $E_T^{cone} > 8$ GeV

HPP TLT 06 true was equivalent to all of the following being true:

- HPP SLT 5 == true
- $P_T^{\text{miss}} > 8$ GeV
- at least 1 cone jet with $E_T^{\text{jet}} > 8$ GeV, $\eta^{\text{jet}} < 2.5$

Note that this is the only condition in this thesis where cone jets were considered. In all other points, a jet will refer explicitly to jets found using the k_T cluster algorithm. HPP TLT 10 true was equivalent to all of the following being true:

- HPP SLT 5 == true
- $P_T^{\text{miss}} > 8$ GeV
- at least 1 k_T jet with $E_T^{\text{jet}} > 8$ GeV, $\eta^{\text{jet}} < 2.5$

E.4 DST Bits

In the principle trigger selection, data events were required to have DST bit 34 set to true. This bit was equivalent to the principle trigger selection described in the following sections. In the secondary selection, at least one of DST bits 34, 68, 69 and 73 was required to be set to true. These bits form a superset of the alternative trigger selection.

E.5 Selection Flags

The ZEUS reconstruction library contains a flag EVTAKE for each event, which is set to true if the event was taken during reliable conditions. Data events were only selected if the EVTAKE flag was set to true. MC events were not subject to this selection.

The two methods of polarization measurement, LPOL and TPOL, produced comparable but different measurements of the average polarization during each data taking run. The ZEUS reconstruction library contains two boolean flags, LPOLTAKE and TPOLTAKE, which indicate if the event was taken when the LPOL and TPOL were functioning properly. If the integrated luminosity for a given run measured by the LPOL L_{LPOL} was greater than or equal to that that of the TPOL, L_{TPOL}, then data events were only selected if LPOLTAKE was true. If $L_{\mathrm{TPOL}} > L_{\mathrm{LPOL}}$ during the run, then events were only taken if TPOLTAKE was true. MC events were not subject to this selection. The average polarization value and integrated luminosity for each data run was exclusively taken from the LPOL if $L_{\mathrm{LPOL}} < L_{\mathrm{TPOL}}$, otherwise values from the TPOL were used. All MC presented here have zero average polarization.

Events were required to have $P_T^{\text{miss}} > 9$ GeV, $P_T^{\text{miss}}/E_T > 0.3$, and at least one calorimeter jet within $-1 < \eta^{\text{jet}} < 2.5$ and $E_T^{\text{jet}} > 3$ GeV, where E_T^{jet} was computed purely from cell energies. These cuts are less restrictive forms of applied cuts and will be described later in this chapter in detail. Events meeting all these criteria were then retrieved from the ZARAH computing farm and stored on a local workstation for analysis.

Appendix F

Correction Functions

Appendix G

Data Tables

η^{jet} bin	$d\sigma/d\eta^{\text{jet}}$ (pb)	δ_{stat}	δ_{syst}	δ_{ES}
$P_{e^-} = -0.27$ - inclusive jets				
$-1.0, -0.5$	4.22	± 0.38	± 0.32	$^{+0.17}_{-0.16}$
$-0.5, 0.0$	13.35	± 0.62	± 0.51	$^{+0.30}_{-0.29}$
$0.0, 0.5$	23.40	± 0.77	± 0.29	$^{+0.23}_{-0.22}$
$0.5, 1.0$	27.77	± 0.81	± 0.82	± 0.09
$1.0, 1.5$	28.30	± 0.82	± 0.92	$^{+0.08}_{-0.09}$
$1.5, 2.0$	24.71	± 0.79	± 0.40	$^{+0.10}_{-0.09}$
$2.0, 2.5$	19.41	± 0.87	± 2.36	± 0.15
$P_{e^-} = +0.30$ - inclusive jets				
$-1.0, -0.5$	2.81	± 0.37	± 0.21	$^{+0.11}_{-0.10}$
$-0.5, 0.0$	7.22	± 0.55	± 0.28	± 0.16
$0.0, 0.5$	12.45	± 0.67	± 0.47	$^{+0.12}_{-0.11}$
$0.5, 1.0$	16.05	± 0.74	± 0.48	± 0.05
$1.0, 1.5$	15.99	± 0.74	± 0.50	± 0.05
$1.5, 2.0$	15.34	± 0.75	± 0.42	$^{+0.06}_{-0.05}$
$2.0, 2.5$	11.39	± 0.80	± 1.37	± 0.09
$P_{e^+} = -0.37$ - inclusive jets				
$-1.0, -0.5$	1.26	± 0.28	± 0.14	± 0.04
$-0.5, 0.0$	3.33	± 0.38	± 0.16	± 0.05
$0.0, 0.5$	5.68	± 0.47	± 0.14	± 0.04
$0.5, 1.0$	6.64	± 0.49	± 0.40	± 0.04
$1.0, 1.5$	6.74	± 0.49	± 0.24	± 0.03
$1.5, 2.0$	6.52	± 0.50	± 0.07	± 0.04
$2.0, 2.5$	5.09	± 0.55	± 0.93	± 0.06
$P_{e^+} = +0.32$ - inclusive jets				
$-1.0, -0.5$	2.92	± 0.36	± 0.30	± 0.09
$-0.5, 0.0$	7.37	± 0.49	± 0.29	± 0.11
$0.0, 0.5$	10.34	± 0.54	± 0.41	± 0.08
$0.5, 1.0$	14.75	± 0.63	± 0.65	± 0.08
$1.0, 1.5$	12.38	± 0.58	± 0.65	± 0.06
$1.5, 2.0$	11.64	± 0.58	± 0.50	$^{+0.07}_{-0.06}$
$2.0, 2.5$	10.22	± 0.68	± 1.26	± 0.12

Table G.1: Differential polarized inclusive-jet cross-sections $d\sigma/d\eta^{\text{jet}}$ for jets of hadrons in the laboratory frame selected with the longitudinally invariant k_T cluster algorithm. The statistical, uncorrelated systematic and energy-scale (ES) uncertainties are shown separately.

$E_T^{\rm jet}$ bin (GeV)	$d\sigma/dE_T^{\rm jet}$ (pb/GeV)	$\delta_{\rm stat}$	$\delta_{\rm syst}$	$\delta_{\rm ES}$
$P_{e^-} = -0.27$ - inclusive jets				
14, 21	2.318	± 0.076	± 0.140	$^{+0.045}_{-0.051}$
21, 29	1.776	± 0.056	± 0.079	$^{+0.019}_{-0.018}$
29, 41	1.419	± 0.038	± 0.070	$^{+0.009}_{-0.010}$
41, 55	0.834	± 0.027	± 0.051	$^{+0.011}_{-0.010}$
55, 71	0.450	± 0.018	± 0.022	± 0.011
71, 87	0.212	± 0.012	± 0.057	$^{+0.003}_{-0.002}$
87, 120	0.0421	± 0.0035	± 0.0225	$^{+0.0063}_{-0.0050}$
$P_{e^-} = +0.30$ - inclusive jets				
14, 21	1.284	± 0.068	± 0.089	$^{+0.025}_{-0.028}$
21, 29	1.081	± 0.052	± 0.049	$^{+0.012}_{-0.011}$
29, 41	0.795	± 0.035	± 0.041	$^{+0.005}_{-0.006}$
41, 55	0.486	± 0.024	± 0.030	± 0.006
55, 71	0.263	± 0.017	± 0.016	$^{+0.007}_{-0.006}$
71, 87	0.106	± 0.010	± 0.029	± 0.001
87, 120	0.0276	± 0.0035	± 0.0149	$^{+0.0041}_{-0.0033}$
$P_{e^+} = -0.37$ - inclusive jets				
14, 21	0.761	± 0.053	± 0.058	± 0.012
21, 29	0.584	± 0.039	± 0.031	$^{+0.003}_{-0.004}$
29, 41	0.338	± 0.023	± 0.019	$^{+0.004}_{-0.003}$
41, 55	0.160	± 0.014	± 0.011	± 0.004
55, 71	0.0602	± 0.0079	± 0.0037	$^{+0.0025}_{-0.0023}$
71, 87	0.0157	± 0.0039	± 0.0047	$^{+0.0007}_{-0.0006}$
87, 120	0.00166	± 0.00083	± 0.00106	$^{+0.00032}_{-0.00025}$
$P_{e^+} = +0.32$ - inclusive jets				
14, 21	1.576	± 0.066	± 0.112	$^{+0.026}_{-0.024}$
21, 29	1.077	± 0.045	± 0.020	$^{+0.006}_{-0.007}$
29, 41	0.675	± 0.028	± 0.037	$^{+0.007}_{-0.006}$
41, 55	0.307	± 0.017	± 0.020	± 0.007
55, 71	0.1135	± 0.0094	± 0.0143	$^{+0.0047}_{-0.0043}$
71, 87	0.0374	± 0.0052	± 0.0083	$^{+0.0016}_{-0.0014}$
87, 120	0.0050	± 0.0012	± 0.0027	$^{+0.0010}_{-0.0008}$

Table G.2: Differential polarized inclusive-jet cross-sections $d\sigma/dE_T^{\rm jet}$. Other details as in the caption to Table G.1.

Q^2 bin (GeV^2)	$d\sigma/dQ^2$ (pb/GeV^2)	$\delta_{\rm stat}$	$\delta_{\rm syst}$	$\delta_{\rm ES}$
$P_{e^-} = -0.27$ - inclusive jets				
$200, 500$	0.0246	± 0.0013	± 0.0015	$^{+0.0024}_{-0.0023}$
$500, 1000$	0.02226	± 0.00079	± 0.00090	$^{+0.00061}_{-0.00059}$
$1000, 2000$	0.01578	± 0.00046	± 0.00053	± 0.00022
$2000, 4000$	0.00797	± 0.00023	± 0.00007	± 0.00004
$4000, 10000$	0.002532	± 0.000072	± 0.000134	± 0.000038
$10000, 20000$	0.000429	± 0.000022	± 0.000029	± 0.000018
$20000, 88000$	$1.4 \cdot 10^{-5}$	$\pm 1.3 \cdot 10^{-6}$	$\pm 5.7 \cdot 10^{-6}$	$\pm 1.4 \cdot 10^{-6}$
$P_{e^-} = +0.30$ - inclusive jets				
$200, 500$	0.0135	± 0.0011	± 0.0011	± 0.0013
$500, 1000$	0.01332	± 0.00074	± 0.00051	$^{+0.00036}_{-0.00035}$
$1000, 2000$	0.00926	± 0.00042	± 0.00030	± 0.00013
$2000, 4000$	0.00437	± 0.00020	± 0.00004	± 0.00002
$4000, 10000$	0.001364	± 0.000064	± 0.000075	± 0.000020
$10000, 20000$	$30.6 \cdot 10^{-5}$	$\pm 2.2 \cdot 10^{-5}$	$\pm 2.0 \cdot 10^{-5}$	$\pm 1.3 \cdot 10^{-5}$
$20000, 88000$	$8.1 \cdot 10^{-6}$	$\pm 1.2 \cdot 10^{-6}$	$\pm 3.3 \cdot 10^{-6}$	$\pm 0.8 \cdot 10^{-6}$
$P_{e^+} = -0.37$ - inclusive jets				
$200, 500$	0.00984	± 0.00096	± 0.00049	$^{+0.00091}_{-0.00087}$
$500, 1000$	0.00814	± 0.00058	± 0.00026	± 0.00016
$1000, 2000$	0.00463	± 0.00030	± 0.00022	± 0.00002
$2000, 4000$	0.00182	± 0.00013	± 0.00007	± 0.00003
$4000, 10000$	$34.1 \cdot 10^{-5}$	$\pm 3.1 \cdot 10^{-5}$	$\pm 2.0 \cdot 10^{-5}$	$\pm 1.4 \cdot 10^{-5}$
$10000, 20000$	$25.0 \cdot 10^{-6}$	$\pm 5.9 \cdot 10^{-6}$	$\pm 5.7 \cdot 10^{-6}$	$\pm 2.3 \cdot 10^{-6}$
$P_{e^+} = +0.32$ - inclusive jets				
$200, 500$	0.0198	± 0.0012	± 0.0010	$^{+0.0018}_{-0.0017}$
$500, 1000$	0.01586	± 0.00070	± 0.00023	$^{+0.00030}_{-0.00031}$
$1000, 2000$	0.00905	± 0.00036	± 0.00027	$^{+0.00004}_{-0.00004}$
$2000, 4000$	0.00345	± 0.00016	± 0.00014	$^{+0.00005}_{-0.00005}$
$4000, 10000$	$68.8 \cdot 10^{-5}$	$\pm 3.9 \cdot 10^{-5}$	$\pm 5.6 \cdot 10^{-5}$	$\pm 2.7 \cdot 10^{-5}$
$10000, 20000$	$61.3 \cdot 10^{-6}$	$\pm 8.0 \cdot 10^{-6}$	$\pm 10.0 \cdot 10^{-6}$	$\pm 5.6 \cdot 10^{-6}$
$20000, 88000$	$3.5 \cdot 10^{-7}$	$\pm 1.8 \cdot 10^{-7}$	$\pm 2.8 \cdot 10^{-7}$	$\pm 0.6 \cdot 10^{-7}$

Table G.3: Differential polarized inclusive-jet cross-sections $d\sigma/dQ^2$. Other details as in the caption to Table G.1.

x bin	$d\sigma/dx$ (pb/GeV)	δ_{stat}	δ_{syst}	δ_{ES}
$P_{e^-} = -0.27$ - inclusive jets				
$0.006, 0.025$	16.17	± 0.70	± 0.83	$^{+1.06}_{-1.01}$
$0.025, 0.063$	46.9	± 1.3	± 1.6	± 0.9
$0.063, 0.16$	60.6	± 1.4	± 0.9	± 0.2
$0.16, 0.40$	39.7	± 1.1	± 1.7	± 0.7
$0.40, 1.0$	3.94	± 0.33	± 0.53	± 0.29
$P_{e^-} = +0.30$ - inclusive jets				
$0.006, 0.025$	9.71	± 0.65	± 0.76	$^{+0.64}_{-0.61}$
$0.025, 0.063$	24.3	± 1.1	± 0.9	± 0.5
$0.063, 0.16$	36.6	± 1.3	± 0.6	± 0.1
$0.16, 0.40$	23.2	± 1.0	± 1.2	± 0.4
$0.40, 1.0$	2.21	± 0.30	± 0.38	± 0.16
$P_{e^+} = -0.37$ - inclusive jets				
$0.006, 0.025$	6.10	± 0.54	± 0.28	$^{+0.35}_{-0.34}$
$0.025, 0.063$	13.59	± 0.81	± 0.53	± 0.15
$0.063, 0.16$	14.90	± 0.82	± 0.62	± 0.16
$0.16, 0.40$	5.22	± 0.47	± 0.30	± 0.13
$0.40, 1.0$	0.33	± 0.11	± 0.12	± 0.02
$P_{e^+} = +0.32$ - inclusive jets				
$0.006, 0.025$	12.34	± 0.67	± 0.56	$^{+0.71}_{-0.69}$
$0.025, 0.063$	28.1	± 1.0	± 1.0	± 0.3
$0.063, 0.16$	26.57	± 0.95	± 0.88	± 0.29
$0.16, 0.40$	11.55	± 0.60	± 0.65	± 0.28
$0.40, 1.0$	0.50	± 0.12	± 0.06	± 0.04

Table G.4: Differential polarized inclusive-jet cross-sections $d\sigma/dx$. Other details as in the caption to Table G.1.

$\eta^{\rm jet}$ bin	$d\sigma/d\eta^{\rm jet}$ (pb)	$\delta_{\rm stat}$	$\delta_{\rm syst}$	$\delta_{\rm ES}$	$C_{\rm QED}$	$C_{\rm had}$
unpolarized - inclusive jets						
$-1.0, -0.5$	3.58	± 0.28	± 0.30	$^{+0.15}_{-0.13}$	0.97	0.93
$-0.5, 0.0$	10.38	± 0.43	± 0.35	$^{+0.24}_{-0.22}$	0.97	0.98
$0.0, 0.5$	18.06	± 0.53	± 0.34	± 0.17	0.98	0.99
$0.5, 1.0$	22.17	± 0.57	± 0.75	± 0.07	0.97	1.00
$1.0, 1.5$	22.38	± 0.58	± 0.90	± 0.07	0.97	1.00
$1.5, 2.0$	20.33	± 0.57	± 0.31	$^{+0.08}_{-0.07}$	0.96	1.01
$2.0, 2.5$	15.59	± 0.61	± 1.85	± 0.12	0.96	1.01
$\overline{\eta}^{\rm jet}$ bin	$d\sigma/d\overline{\eta}^{\rm jet}$ (pb)	$\delta_{\rm stat}$	$\delta_{\rm syst}$	$\delta_{\rm ES}$	$C_{\rm QED}$	$C_{\rm had}$
unpolarized - dijets						
$-1.0, -0.5$	0.103	± 0.073	± 0.003	$^{+0.033}_{-0.032}$	0.80	0.60
$-0.5, 0.0$	1.48	± 0.26	± 0.52	± 0.09	0.96	0.81
$0.0, 0.5$	3.63	± 0.33	± 0.88	± 0.12	0.97	0.89
$0.5, 1.0$	5.68	± 0.37	± 0.43	$^{+0.14}_{-0.13}$	0.98	0.91
$1.0, 1.5$	6.43	± 0.34	± 0.07	$^{+0.12}_{-0.11}$	0.97	0.92
$1.5, 2.0$	3.77	± 0.24	± 0.14	± 0.07	0.95	0.92
$2.0, 2.5$	0.58	± 0.10	± 0.05	± 0.01	0.93	0.88
unpolarized - three jets						
$0.0, 0.5$	0.49	± 0.18	± 0.49	$^{+0.03}_{-0.05}$	0.95	0.75
$0.5, 1.0$	1.05	± 0.21	± 0.15	$^{+0.05}_{-0.06}$	0.93	0.78
$1.0, 1.5$	1.06	± 0.17	± 0.13	$^{+0.04}_{-0.03}$	0.99	0.80
$1.5, 2.5$	0.246	± 0.046	± 0.053	$^{+0.009}_{-0.007}$	0.99	0.80

Table G.5: Differential unpolarized inclusive-jet, dijet and three-jet cross-sections $d\sigma/d\eta^{\rm jet}$ and $d\sigma/d\overline{\eta}^{\rm jet}$ in $e^- p$ collisions for jets of hadrons in the laboratory frame selected with the longitudinally invariant k_T cluster algorithm. The statistical, uncorrelated systematic and jet-energy-scale (ES) uncertainties are shown separately. The multiplicative corrections for QED radiative effects, $C_{\rm QED}$, and the corrections for hadronization effects, $C_{\rm had}$, to be applied to the parton-level NLO QCD calculations, are shown in the last two columns.

η^{jet} bin	$d\sigma/d\eta^{\text{jet}}$ (pb)	δ_{stat}	δ_{syst}	δ_{ES}	C_{QED}	C_{had}
unpolarized - inclusive jets						
$-1.0, -0.5$	2.12	± 0.24	± 0.21	$^{+0.07}_{-0.06}$	0.92	0.94
$-0.5, 0.0$	5.45	± 0.34	± 0.23	± 0.08	0.94	0.98
$0.0, 0.5$	8.34	± 0.39	± 0.22	± 0.06	0.95	0.99
$0.5, 1.0$	10.90	± 0.43	± 0.54	± 0.06	0.95	1.00
$1.0, 1.5$	9.95	± 0.42	± 0.42	± 0.05	0.95	1.00
$1.5, 2.0$	9.48	± 0.42	± 0.26	$^{+0.06}_{-0.05}$	0.94	1.01
$2.0, 2.5$	7.88	± 0.48	± 1.15	± 0.09	0.93	1.02
$\overline{\eta}^{\text{jet}}$ bin	$d\sigma/d\overline{\eta}^{\text{jet}}$ (pb)	δ_{stat}	δ_{syst}	δ_{ES}	C_{QED}	C_{had}
unpolarized - dijets						
$-0.5, 0.0$	0.92	± 0.23	± 0.33	$^{+0.07}_{-0.05}$	0.94	0.83
$0.0, 0.5$	1.75	± 0.28	± 0.42	$^{+0.06}_{-0.05}$	0.94	0.90
$0.5, 1.0$	3.01	± 0.32	± 0.24	$^{+0.07}_{-0.06}$	0.95	0.94
$1.0, 1.5$	3.52	± 0.28	± 0.06	$^{+0.07}_{-0.06}$	0.95	0.94
$1.5, 2.0$	1.95	± 0.20	± 0.11	± 0.04	0.94	0.94
$2.0, 2.5$	0.287	± 0.073	± 0.043	$^{+0.008}_{-0.005}$	0.93	0.91
unpolarized - three jets						
$0.0, 0.5$	0.079	± 0.079	± 0.079	$^{+0.006}_{-0.003}$	0.92	0.72
$0.5, 1.0$	0.68	± 0.23	± 0.09	$^{+0.04}_{-0.03}$	0.93	0.79
$1.0, 1.5$	0.254	± 0.086	± 0.033	$^{+0.011}_{-0.010}$	0.94	0.81
$1.5, 2.5$	0.087	± 0.029	± 0.019	± 0.003	0.91	0.83

Table G.6: Differential unpolarized inclusive-jet, dijet and three-jet cross-sections $d\sigma/d\eta^{\text{jet}}$ and $d\sigma/\overline{\eta}^{\text{jet}}$ in e^+p collisions. Other details as in the caption to Table G.5.

$E_T^{\rm jet}$ bin (GeV)	$d\sigma/dE_T^{\rm jet}$ (pb/GeV)	$\delta_{\rm stat}$	$\delta_{\rm syst}$	$\delta_{\rm ES}$	$C_{\rm QED}$	$C_{\rm had}$
unpolarized - inclusive jets						
$14, 21$	1.819	± 0.053	± 0.120	$^{+0.035}_{-0.040}$	1.03	0.99
$21, 29$	1.449	± 0.040	± 0.040	$^{+0.016}_{-0.014}$	1.01	1.00
$29, 41$	1.118	± 0.027	± 0.042	$^{+0.007}_{-0.008}$	0.97	1.00
$41, 55$	0.668	± 0.019	± 0.039	± 0.008	0.95	1.00
$55, 71$	0.361	± 0.013	± 0.031	± 0.009	0.92	0.99
$71, 87$	0.1596	± 0.0082	± 0.0360	$^{+0.0020}_{-0.0015}$	0.88	0.99
$87, 120$	0.0355	± 0.0026	± 0.0190	$^{+0.0053}_{-0.0042}$	0.83	0.98
$\overline{E}_T^{\rm jet}$ bin (GeV)	$d\sigma/d\overline{E}_T^{\rm jet}$ (pb/GeV)	$\delta_{\rm stat}$	$\delta_{\rm syst}$	$\delta_{\rm ES}$	$C_{\rm QED}$	$C_{\rm had}$
unpolarized - dijets						
$9.5, 14$	0.345	± 0.032	± 0.017	± 0.004	1.03	0.88
$14, 21$	0.502	± 0.028	± 0.077	$^{+0.007}_{-0.004}$	0.99	0.91
$21, 29$	0.375	± 0.021	± 0.030	± 0.010	0.94	0.92
$29, 41$	0.156	± 0.011	± 0.005	± 0.007	0.92	0.90
$41, 55$	0.0390	± 0.0049	± 0.0107	$^{+0.0037}_{-0.0026}$	0.88	0.90
$55, 71$	0.0070	± 0.0023	± 0.0007	$^{+0.0014}_{-0.0016}$	0.90	0.95
$71, 87$	0.0021	± 0.0021	± 0.0021	$^{+0.0014}_{-0.0000}$	1.00	0.94
unpolarized - three jets						
$8, 9.5$	0.0096	± 0.0096	± 0.0025	$^{+0.0016}_{-0.0017}$	1.02	0.72
$9.5, 14$	0.060	± 0.015	± 0.015	± 0.001	1.02	0.77
$14, 21$	0.099	± 0.015	± 0.003	± 0.004	0.96	0.79
$21, 29$	0.0481	± 0.0087	± 0.0036	$^{+0.0030}_{-0.0027}$	0.92	0.78
$29, 41$	0.0078	± 0.0029	± 0.0008	$^{+0.0007}_{-0.0006}$	0.86	0.85

Table G.7: Differential unpolarized inclusive-jet, dijet and three-jet cross-sections $d\sigma/dE_T^{\rm jet}$ and $d\sigma/d\overline{E}_T^{\rm jet}$ in $e^- p$ collisions. Other details as in the caption to Table G.5.

$E_T^{\rm jet}$ bin (GeV)	$d\sigma/dE_T^{\rm jet}$ (pb/GeV)	$\delta_{\rm stat}$	$\delta_{\rm syst}$	$\delta_{\rm ES}$	$C_{\rm QED}$	$C_{\rm had}$
unpolarized - inclusive jets						
$14, 21$	1.200	± 0.046	± 0.087	$^{+0.020}_{-0.019}$	0.99	1.00
$21, 29$	0.863	± 0.033	± 0.029	$^{+0.005}_{-0.006}$	0.96	1.00
$29, 41$	0.522	± 0.019	± 0.025	± 0.005	0.93	1.00
$41, 55$	0.242	± 0.012	± 0.016	± 0.006	0.91	0.99
$55, 71$	0.0901	± 0.0067	± 0.0078	$^{+0.0037}_{-0.0034}$	0.87	0.99
$71, 87$	0.0269	± 0.0035	± 0.0067	$^{+0.0011}_{-0.0010}$	0.84	0.98
$87, 120$	0.00329	± 0.00078	± 0.00179	$^{+0.00064}_{-0.00050}$	0.79	0.97
$\overline{E}_T^{\rm jet}$ bin (GeV)	$d\sigma/d\overline{E}_T^{\rm jet}$ (pb/GeV)	$\delta_{\rm stat}$	$\delta_{\rm syst}$	$\delta_{\rm ES}$	$C_{\rm QED}$	$C_{\rm had}$
unpolarized - dijets						
$9.5, 14$	0.288	± 0.033	± 0.017	$^{+0.001}_{-0.002}$	0.99	0.90
$14, 21$	0.330	± 0.026	± 0.052	± 0.004	0.95	0.93
$21, 29$	0.190	± 0.018	± 0.015	$^{+0.007}_{-0.006}$	0.93	0.93
$29, 41$	0.0433	± 0.0066	± 0.0023	$^{+0.0026}_{-0.0022}$	0.88	0.93
$41, 55$	0.0112	± 0.0032	± 0.0031	$^{+0.0014}_{-0.0010}$	0.90	0.95
unpolarized - three jets						
$8, 9.5$	0.019	± 0.019	± 0.005	± 0.002	0.82	0.73
$9.5, 14$	0.040	± 0.013	± 0.010	± 0.001	0.96	0.76
$14, 21$	0.043	± 0.012	± 0.002	± 0.002	0.93	0.80
$21, 29$	0.0034	± 0.0024	± 0.0003	$^{+0.0003}_{-0.0002}$	0.86	0.82
$29, 41$	0.0018	± 0.0018	± 0.0002	$^{+0.0003}_{-0.0002}$	0.88	0.86

Table G.8: Differential unpolarized inclusive-jet, dijet and three-jet cross-sections $d\sigma/dE_T^{\rm jet}$ and $d\sigma/d\overline{E}_T^{\rm jet}$ in e^+p collisions. Other details as in the caption to Table G.5.

Q^2 bin (GeV^2)	$d\sigma/dQ^2$ (pb/GeV^2)	$\delta_{\rm stat}$	$\delta_{\rm syst}$	$\delta_{\rm ES}$	$C_{\rm QED}$	$C_{\rm had}$
unpolarized - inclusive jets						
$200, 500$	0.01921	± 0.00087	± 0.00131	$^{+0.00190}_{-0.00180}$	0.98	0.97
$500, 1000$	0.01803	± 0.00056	± 0.00047	$^{+0.00049}_{-0.00048}$	0.99	1.00
$1000, 2000$	0.01268	± 0.00032	± 0.00017	± 0.00018	0.98	1.00
$2000, 4000$	0.00623	± 0.00016	± 0.00006	± 0.00003	0.97	1.00
$4000, 10000$	0.001963	± 0.000050	± 0.000097	± 0.000029	0.95	1.00
$10000, 20000$	0.000376	± 0.000016	± 0.000045	$^{+0.000015}_{-0.000016}$	0.94	1.00
$20000, 88000$	$1.121 \cdot 10^{-5}$	$\pm 0.091 \cdot 10^{-5}$	$\pm 0.706 \cdot 10^{-5}$	$^{+0.113}_{-0.114} \cdot 10^{-5}$	0.93	1.00
unpolarized - dijets						
$200, 500$	0.00409	± 0.00091	± 0.00112	$^{+0.00094}_{-0.00083}$	1.00	0.91
$500, 1000$	0.00323	± 0.00031	± 0.00037	$^{+0.00027}_{-0.00026}$	0.97	0.92
$1000, 2000$	0.00251	± 0.00016	± 0.00004	± 0.00009	0.97	0.91
$2000, 4000$	0.001170	± 0.000071	± 0.000112	$^{+0.000024}_{-0.000023}$	0.96	0.91
$4000, 10000$	0.000343	± 0.000021	± 0.000029	± 0.000011	0.95	0.89
$10000, 20000$	$69.8 \cdot 10^{-6}$	$\pm 6.9 \cdot 10^{-6}$	$\pm 23.9 \cdot 10^{-6}$	$\pm 4.1 \cdot 10^{-6}$	0.99	0.87
$20000, 88000$	$2.11 \cdot 10^{-6}$	$\pm 0.37 \cdot 10^{-6}$	$\pm 1.62 \cdot 10^{-6}$	$\pm 0.26 \cdot 10^{-5}$	0.96	0.86
unpolarized - three jets						
$500, 1000$	0.00034	± 0.00018	± 0.00015	$^{+0.00006}_{-0.00005}$	0.98	0.78
$1000, 2000$	0.000306	± 0.000073	± 0.000025	$^{+0.000027}_{-0.000026}$	0.96	0.78
$2000, 4000$	0.000193	± 0.000034	± 0.000024	$^{+0.000011}_{-0.000010}$	0.95	0.79
$4000, 10000$	$5.04 \cdot 10^{-5}$	$\pm 0.93 \cdot 10^{-5}$	$\pm 2.18 \cdot 10^{-5}$	$\pm 0.20 \cdot 10^{-5}$	0.95	0.79
$10000, 20000$	$1.04 \cdot 10^{-5}$	$\pm 0.25 \cdot 10^{-5}$	$\pm 0.70 \cdot 10^{-5}$	$^{+0.09}_{-0.08} \cdot 10^{-5}$	0.95	0.75
$20000, 88000$	$1.34 \cdot 10^{-7}$	$\pm 0.99 \cdot 10^{-7}$	$\pm 0.06 \cdot 10^{-7}$	$\pm 0.19 \cdot 10^{-7}$	0.92	0.77

Table G.9: Differential unpolarized inclusive-jet, dijet and three-jet cross-sections $d\sigma/dQ^2$ in $e^- p$ collisions. Other details as in the caption to Table G.5.

Q^2 bin (GeV^2)	$d\sigma/dQ^2$ (pb/GeV^2)	$\delta_{\rm stat}$	$\delta_{\rm syst}$	$\delta_{\rm ES}$	$C_{\rm QED}$	$C_{\rm had}$
unpolarized - inclusive jets						
$200, 500$	0.01525	± 0.00082	± 0.00074	$^{+0.00141}_{-0.00134}$	0.96	0.97
$500, 1000$	0.01241	± 0.00050	± 0.00018	± 0.00024	0.96	1.00
$1000, 2000$	0.00707	± 0.00026	± 0.00021	± 0.00003	0.95	1.00
$2000, 4000$	0.00273	± 0.00011	± 0.00010	± 0.00004	0.94	1.00
$4000, 10000$	0.000530	± 0.000027	± 0.000037	± 0.000021	0.91	1.00
$10000, 20000$	$4.35 \cdot 10^{-5}$	$\pm 0.53 \cdot 10^{-5}$	$\pm 0.71 \cdot 10^{-5}$	$\pm 0.40 \cdot 10^{-5}$	0.88	1.00
$20000, 88000$	$2.3 \cdot 10^{-7}$	$\pm 1.1 \cdot 10^{-7}$	$\pm 1.5 \cdot 10^{-7}$	$\pm 0.4 \cdot 10^{-7}$	0.81	1.00
unpolarized - dijets						
$200, 500$	0.00204	± 0.00072	± 0.00051	$^{+0.00042}_{-0.00037}$	0.98	0.92
$500, 1000$	0.00301	± 0.00033	± 0.00033	$^{+0.00025}_{-0.00024}$	0.96	0.93
$1000, 2000$	0.00152	± 0.00014	± 0.00003	$^{+0.00004}_{-0.00003}$	0.95	0.93
$2000, 4000$	0.000605	± 0.000058	± 0.000060	± 0.000016	0.94	0.92
$4000, 10000$	0.000106	± 0.000013	± 0.000011	± 0.000006	0.91	0.92
$10000, 20000$	$9.3 \cdot 10^{-6}$	$\pm 2.4 \cdot 10^{-6}$	$\pm 3.2 \cdot 10^{-5}$	$^{+1.1}_{-1.0} \cdot 10^{-6}$	0.92	0.92
$20000, 88000$	$7.4 \cdot 10^{-8}$	$\pm 7.4 \cdot 10^{-8}$	$\pm 5.8 \cdot 10^{-8}$	$\pm 1.1 \cdot 10^{-8}$	0.93	0.88
unpolarized - three jets						
$500, 1000$	0.00038	± 0.00020	± 0.00017	± 0.00006	0.97	0.78
$1000, 2000$	0.000156	± 0.000055	± 0.000013	$^{+0.000014}_{-0.000013}$	0.91	0.80
$2000, 4000$	0.000065	± 0.000021	± 0.000008	$^{+0.000003}_{-0.000002}$	0.91	0.80
$4000, 10000$	$9.2 \cdot 10^{-6}$	$\pm 4.4 \cdot 10^{-6}$	$\pm 4.1 \cdot 10^{-6}$	$\pm 0.7 \cdot 10^{-6}$	0.88	0.79
$10000, 20000$	$4.6 \cdot 10^{-7}$	$\pm 4.6 \cdot 10^{-7}$	$\pm 3.1 \cdot 10^{-7}$	$\pm 0.6 \cdot 10^{-7}$	1.00	0.82

Table G.10: Differential unpolarized inclusive-jet, dijet and three-jet cross-sections $d\sigma/dQ^2$ in e^+p collisions. Other details as in the caption to Table G.5.

x bin	$d\sigma/dx$ (pb)	$\delta_{\rm stat}$	$\delta_{\rm syst}$	$\delta_{\rm ES}$	$C_{\rm QED}$	$C_{\rm had}$
unpolarized - inclusive jets						
$0.006, 0.025$	13.12	± 0.50	± 0.74	$^{+0.86}_{-0.82}$	0.95	1.01
$0.025, 0.063$	35.82	± 0.85	± 1.13	$^{+0.70}_{-0.69}$	0.98	1.00
$0.063, 0.16$	49.26	± 0.98	± 0.09	± 0.14	0.97	0.99
$0.16, 0.40$	31.81	± 0.77	± 1.30	$^{+0.53}_{-0.54}$	0.97	0.99
$0.40, 1.0$	3.11	± 0.23	± 0.30	± 0.23	0.95	0.98

Table G.11: Differential unpolarized inclusive-jet cross-sections $d\sigma/dx$ in $e^- p$ collisions. Other details as in the caption to Table G.5.

x bin	$d\sigma/dx$ (pb)	$\delta_{\rm stat}$	$\delta_{\rm syst}$	$\delta_{\rm ES}$	$C_{\rm QED}$	$C_{\rm had}$
unpolarized - inclusive jets						
$0.006, 0.025$	9.49	± 0.47	± 0.41	$^{+0.54}_{-0.53}$	0.93	1.01
$0.025, 0.063$	21.40	± 0.71	± 0.76	± 0.24	0.96	1.00
$0.063, 0.16$	21.64	± 0.69	± 0.76	$^{+0.24}_{-0.23}$	0.95	0.99
$0.16, 0.40$	8.55	± 0.41	± 0.48	± 0.21	0.93	0.98
$0.40, 1.0$	0.439	± 0.090	± 0.084	± 0.032	0.91	0.98

Table G.12: Differential unpolarized inclusive-jet cross-sections $d\sigma/dx$ in $e^+ p$ collisions. Other details as in the caption to Table G.5.

m^{jj} bin (GeV)	$d\sigma/dm^{\mathrm{jj}}$ (pb/GeV)	δ_{stat}	δ_{syst}	δ_{ES}	C_{QED}	C_{had}
unpolarized - dijets						
$10, 15$	0.090	± 0.011	± 0.010	± 0.001	1.02	0.87
$15, 20$	0.207	± 0.018	± 0.011	± 0.002	0.99	0.88
$20, 30$	0.284	± 0.016	± 0.032	$^{+0.005}_{-0.004}$	0.97	0.89
$30, 45$	0.250	± 0.014	± 0.028	$^{+0.006}_{-0.007}$	0.96	0.90
$45, 65$	0.0960	± 0.0083	± 0.0191	$^{+0.0051}_{-0.0038}$	0.95	0.94
$65, 90$	0.0385	± 0.0060	± 0.0058	$^{+0.0023}_{-0.0032}$	0.94	0.96
$90, 120$	0.0132	± 0.0046	± 0.0035	$^{+0.0023}_{-0.0016}$	0.97	0.96
m^{3j} bin (GeV)	$d\sigma/dm^{\mathrm{3j}}$ (pb/GeV)	δ_{stat}	δ_{syst}	δ_{ES}	C_{QED}	C_{had}
unpolarized - three jets						
$20, 30$	0.0069	± 0.0024	± 0.0017	± 0.0001	0.99	0.83
$30, 45$	0.0253	± 0.0045	± 0.0009	$^{+0.0006}_{-0.0008}$	0.99	0.76
$45, 65$	0.0307	± 0.0049	± 0.0012	$^{+0.0012}_{-0.0011}$	0.97	0.77
$65, 90$	0.0150	± 0.0034	± 0.0054	$^{+0.0014}_{-0.0012}$	0.94	0.79
$90, 120$	0.0036	± 0.0022	± 0.0001	$^{+0.0004}_{-0.0003}$	0.94	0.85

Table G.13: Differential unpolarized dijet and three-jet cross-sections $d\sigma/dm^{\mathrm{jj}}$ and $d\sigma/dm^{\mathrm{jj}}$ in $e^- p$ collisions. Other details as in the caption to Table G.5.

m^{ij} bin (GeV)	$d\sigma/dm^{\mathrm{ij}}$ (pb/GeV)	δ_{stat}	δ_{syst}	δ_{ES}	C_{QED}	C_{had}
unpolarized - dijets						
$10, 15$	0.069	± 0.011	± 0.007	± 0.001	0.96	0.90
$15, 20$	0.146	± 0.017	± 0.010	$^{+0.001}_{-0.002}$	0.96	0.90
$20, 30$	0.171	± 0.015	± 0.022	± 0.003	0.95	0.91
$30, 45$	0.108	± 0.010	± 0.013	± 0.003	0.95	0.93
$45, 65$	0.0522	± 0.0077	± 0.0103	$^{+0.0023}_{-0.0025}$	0.94	0.95
$65, 90$	0.0169	± 0.0052	± 0.0026	$^{+0.0015}_{-0.0011}$	0.94	0.97
$90, 120$	0.0020	± 0.0020	± 0.0002	$^{+0.0003}_{-0.0002}$	0.92	0.99
m^{3j} bin (GeV)	$d\sigma/dm^{\mathrm{3j}}$ (pb/GeV)	δ_{stat}	δ_{syst}	δ_{ES}	C_{QED}	C_{had}
unpolarized - three jets						
$20, 30$	0.0051	± 0.0024	± 0.0013	± 0.0001	0.91	0.84
$30, 45$	0.0124	± 0.0037	± 0.0006	$^{+0.0005}_{-0.0003}$	0.95	0.75
$45, 65$	0.0076	± 0.0029	± 0.0007	± 0.0004	0.94	0.78
$65, 90$	0.0049	± 0.0024	± 0.0018	$^{+0.0005}_{-0.0004}$	0.90	0.81

Table G.14: Differential unpolarized dijet and three-jet cross-sections $d\sigma/dm^{\mathrm{ij}}$ and $d\sigma/dm^{\mathrm{3j}}$ in e^+p collisions. Other details as in the caption to Table G.5.

Appendix H

Additional Figures

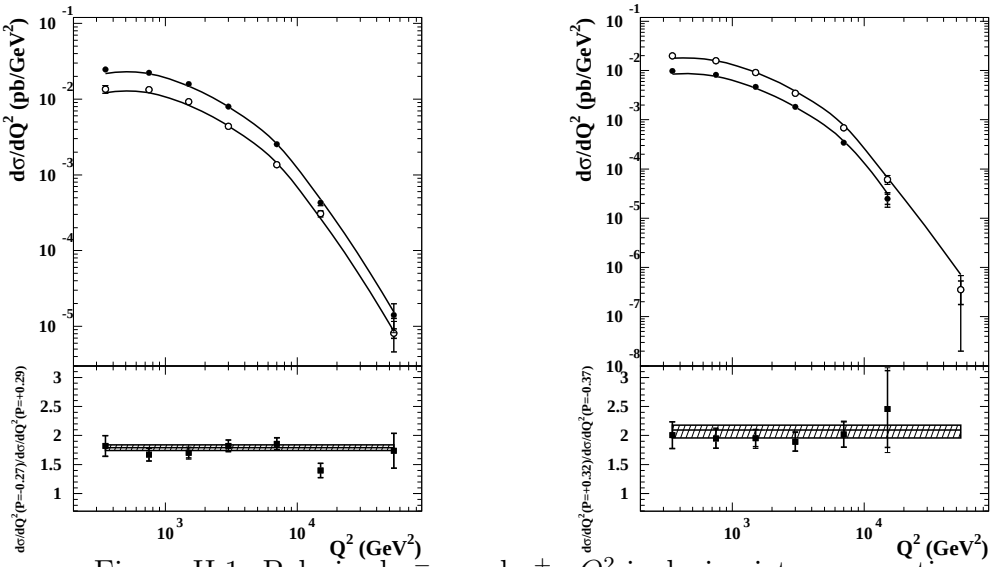

Figure H.1: Polarized $e^{-}p$ and $e^{+}p$ Q^2 inclusive-jet cross sections

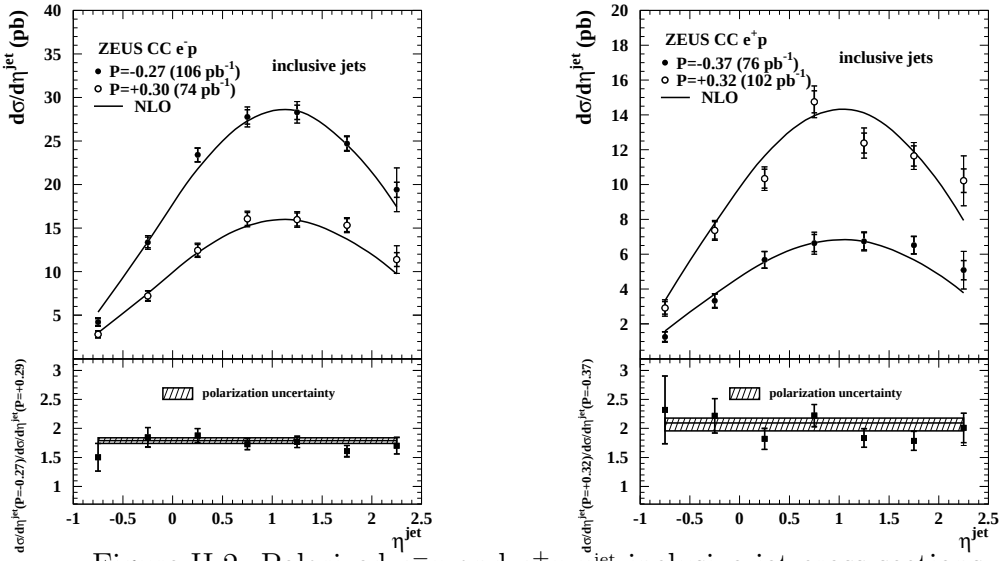

Figure H.2: Polarized e^-p and e^+p $\eta^{\rm jet}$ inclusive-jet cross sections

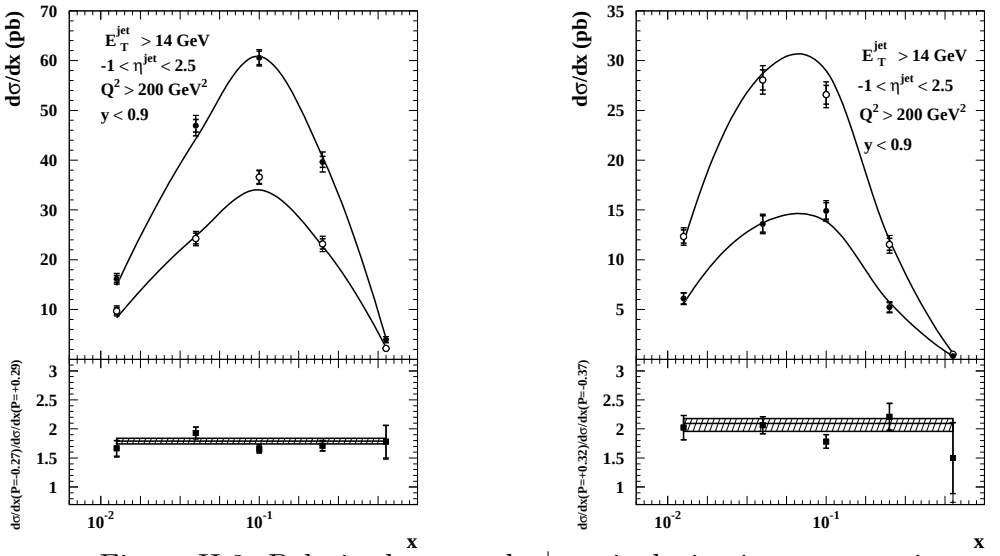

Figure H.3: Polarized e^-p and e^+p x inclusive-jet cross sections

Bibliography

[1] M.H.Seymour, *Jets in QCD*, Technical Report CERN-TH/95-176, CERN, Geneva, Switzerland, 1995.

[2] E.D. Bloom *et al*, Phys. Rev. Lett. **23**, 935 (1969).

[3] Aktas, A. et al., Phys. Lett. **B634**, 173 (2006).

[4] Chekanov, S. and others, Eur. Phys. J. **C32**, 1 (2003).

[5] Chekanov, S. and others, Eur. Phys. J. **C31**, 149 (2003).

[6] Adloff, C. and others, Eur. Phys. J. **C19**, 429 (2001).

[7] F. Halzen and A.D. Martin, *Quarks and Leptons: An Introductory Course in Modern Particle Physics*. John Wiley & Sons, Inc, 1984.

[8] Eidelman, S. and others, Phys. Lett. **B592**, 1 (2004).

[9] E. Mirkes and D. Zeppenfeld, Phys. Lett. **B**, 205 (1996).

[10] E. Mirkes, *Theory of Jets in Deep Inelastic Scattering* (unpublished), 1997, available on `http://hep-ph/9711224v1`. U. Karlseruhe TTP97-39.

[11] W. T. Giele, E. W. N. Glover and D. A. Kosower, Nuclear Phys. **B403**, 633 (1993).

[12] G. 't Hooft, Nucl. Phys. B **61**, 455 (1973).

[13] W. A. Bardeen, Phys. Rev. D **18**, 3998 (1978).

[14] G. Altarelli and G. Parisi, Nucl. Phys. **B 126**, 298 (1977).

[15] V.N. Gribov and L.N. Lipatov, Sov. J. Nucl. Phys. **15**, 438 (1972).

[16] L.N. Lipatov, Sov. J. Nucl. Phys. **20**, 94 (1975).

[17] Yu.L. Dokshitzer, JETP **46**, 641 (1977).

[18] CTEQ Coll., H.L. Lai et al., Eur. Phys. J. **C 12**, 375 (2000).

[19] J. Pumplin et al., JHEP **07**, 012 (2002).

[20] D. Stump, et al., JHEP **10**, 046 (2003).

[21] A.D. Martin, R.G. Roberts and W.J. Stirling, Phys. Rev. **D 50**, 6734 (1994).

[22] ZEUS Coll., S. Chekanov et al., Eur. Phys. J. **C 42**, 1 (2005).

[23] Klein, M., *Proceedings of the 1st Hadron Collider Physics Symposium*, M. Campanelli, A. Clark, X. Wu (ed.), pp. 33 – 39. Diablerets, Switzerland (4-9 Jul 2005).

[24] ZEUS Coll., S. Chekanov et al., Phys. Rev. **D 67**, 012007 (2003).

[25] C. Duprel et al., *Proceedings of the Workshop on Monte Carlo Generators for HERA Physics*, A.T. Doyle, G. Grindhammer, G. Ingelman, H. Jung (ed.), pp. 142 – 150. Hamburg, Germany (1979). Also in preprint arXiv:hep-ph/9910448v1. MADPH-99-1129, PITHA 99/30.

[26] S. Catani and M. H. Seymour, Nucl. Phys. **B 485**, 291 (1997).

[27] A.A. Sokolov and I.M.Ternov, Sov. Phys. Dokl. **8**, 1203 (1964).

[28] ZEUS Coll., *A microvertex Detector for ZEUS* (unpublished), 1997, available on `http://www-zeus.desy.de/ZEUS_ONLY/zeus_notes/ZEUS_NOTES/ZEUS-97-006.ps`. ZEUS-97-006, DESY-PRC 97/01.

[29] J. Krüger, *The Uranium Scintillator Calorimeter for the ZEUS Detector at the Electron-Proton Collider HERA* (unpublished). DESY F35-92-02, 1992.

[30] H1 Coll., I. Abt et al., Nucl. Inst. Meth. **A 386**, 310 (1997).

[31] H1 Coll., SPACAL group, R.-D. Appuhn et al., Nucl. Inst. Meth. **A 386**, 397 (1997).

[32] Helbich M. ; Ning Y. ; Paganis S. ; Ren Z. ; Schmidke W. B. ; Sciulli F. ; Schneekloth U. ; Bttner C. ; Caldwell A. ; Sutiak J., Nuc. Instrum. Meth. A **565**, 572 (2006).

[33] Beckmann, M. and others, Nucl. Instrum. Meth. **A479**, 334 (2002).

[34] V. Andreev et al., *A Proposal for an Upgrade of the HERA Polarimeters for HERA*, Technical Report DESY PRC 98-07, Polarization 2000 Group, DESY, Hamburg, Germany, March 1998.

[35] D.P. Barber et al., Nucl. Inst. Meth. **A 329**, 79 (1993).

[36] Gharibyan, V. and Schuler, K. P., NATO Sci. Ser. II. **111**, 149 (2003).

[37] G. F. Hartner, *VCTRAK Briefing: Program and Math* (unpublished). Zeus-98-058, internal ZEUS-note, 1998.

[38] J. Repond, *Jet Energy Corrections* (unpublished). ZEUS Note96-104.

[39] Abramowicz, Halina and Caldwell, Allen and Sinkus, Ralph, Nucl. Instrum. Meth. **A365**, 508 (1995).

[40] M. Wodarczyk, *Measurement of the F_2 Structure Function of the Proton at HERA from 1996 and 1997 ZEUS Data*. Ph.D. Thesis, University of Wisconsin, 1999.

[41] F. Jaquet and A. Blondel, *Proc. of the European Committee for Future Accelerators*, U. Amaldi (ed.), p. 391. Hamburg, Germany (1979). DESY-79-48.

[42] S.Catani et al., Nucl. Phys. **B406**, 187 (1993).

[43] P.J. Bussey, *EUCELL*. ZEUS Phantom Library.

[44] M. Bengtsson, G. Ingelman and T. Sjöstrand, *Proc. HERA Workshop*, R.D. Peccei (ed.), Vol. 1, pp. 149–165. DESY, Hamburg, Germany (1987).

[45] G. Gustafson and U. Pettersson, Nucl. Phys. **B 306**, 746 (1988).

[46] G. Ingelman, A. Edin and J. Rathsman, Comp. Phys. Comm. **101**, 108 (1997).

[47] T. Sjöstrand, PYTHIA 5.7 AND JETSET 7.4 PHYSICS AND MANUAL, 1993. Preprint CERN-TH 7112/93.

[48] L. Lönnblad, Comp. Phys. Comm. **71**, 15 (1992).

[49] B. Andersson et al., Phys. Rep. **97**, 31 (1983).

[50] A. Kwiatkowski, H. Spiesberger and H.-J. Möhring, Comp. Phys. Comm. **69**, 155 (1992). Also in *Proc. Workshop Physics at HERA*, 1991, DESY, Hamburg.

[51] K. Charchula, G.A. Schuler and H. Spiesberger, Comp. Phys. Comm. **81**, 381 (1994).

[52] R. Brun et al., GEANT3, Technical Report CERN-DD/EE/84-1, CERN, 1987.

[53] M. Beckmann and A. Borissov and S. Brauksiepe and F. Burkart and H. Fischer and J. Franz and F. H. Heinsius and K. Konigsmann and W. Lorenzon and F. M. Menden and A. Most and S. Rudnitsky and C. Schill and J. Seibert and A. Simon, NUCL.INSTRUM.METH.A **479**, 334 (2002).

[54] ZEUS Collaboration; S. Chekanov et al., Phys. Lett. **B 637**, 210 (2006).

[55] ZEUS Coll., S. Chekanov et al., Eur. Phys. J. **C 31**, 149 (2003).

[56] Wing, M. (on behalf of the ZEUS Coll.), *Proc. of the 10th International Conference on Calorimetry in High Energy Physics hep-ex/0206036.*, R. Zhu (ed.), p. 767. Pasadena, USA (2002). Also in preprint hep-ex/0206036;
H. Spiesberger, *An Event Generator for ep Interactions at HERA Including Radiative Processes (Version 4.6)*, 1996, available on `http://www.desy.de/~hspiesb/heracles.html`;
H. Spiesberger, HERACLES *and* DJANGOH*: Event Generation for ep Interactions at HERA Including Radiative Processes*, 1998, available on `http://www.desy.de/~hspiesb/djangoh.html`.

[57] S. Bethke, Prog. Part. Nucl. Phys. **58**, 351 (2007).

[58] Klein, M. and Yoshida, R., Prog. Part. Nucl. Phys. 61 **2008**, 343 (2008).

[59] F. Halzen and A.D. Martin, *Quarks and Leptons*, 2nd edition$^{\text{th}}$ edn. John Wiley and Sons, New York, 1984.

[60] H1 Coll., C. Adloff et al., Eur. Phys. J. **C 19**, 429 (2001).

[61] ZEUS Collaboration; S. Chekanov et al., Nucl. Phys. **B 765**, 1 (2007).

[62] ZEUS Coll., S. Chekanov et al., Eur. Phys. J. **C 32**, 1 (2003).

[63] H1 Coll., C. Adloff et al., Eur. Phys. J. **C 19**, 269 (2001).

[64] Nadolsky, Pavel M. (2008).